E.O. Paton Electric Welding Institute of the National Academy of Sciences of Ukraine

International Scientific-Technical and Production Journal

The Paton WELDING JOURNAL

Issue 12 2020

Published Monthly Since 2000

English Translation of the Monthly «Avtomatychne Zvaryuvannya»
(Avtomaticheskaya Svarka/Automatic Welding) Journal Published in Ukrainian and Russian Since 1948

Founders
E.O. Paton Electric Welding Institute
International Association «Welding»

Publisher
International Association «Welding»

Translators
A.O. Fomin, I.M. Kutianova
Editor
N.G. Khomenko
Electron galley
D.I. Sereda, T.Yu. Snegiryova

Address
E.O. Paton Electric Welding Institute,
International Association «Welding»
11 Kazymyr Malevych Str. (former Bozhenko),
03150, Kyiv, Ukraine
Tel.:/Fax: (38044) 200 82 77
E-mail: journal@paton.kiev.ua
www://patonpublishinghouse.com/eng/journals/tpwj

State Registration Certificate
KV 4790 of 09.01.2001
ISSN 0957-798X
DOI: http://dx.doi.org/10.37434/tpwj

Subscriptions
12 issues per year, back issues available.
$384, subscriptions for the printed (hard copy) version, air postage and packaging included.
$312, subscriptions for the electronic version (sending issues of Journal in pdf format or providing access to IP addresses).
Institutions with current subscriptions on printed version can purchase online access to the electronic versions of any back issues that they have not subscribed to.
Issues of the Journal (more than two years old) are available at a substantially reduced price.

CONTENTS

https://doi.org/10.37434/tpwj2020.12.01

IMPACT OF TECHNOLOGICAL PARAMETERS OF ARC DEPOSITION OF AN ANTICORROSION LAYER IN THE VESSEL OF WWER-1000 REACTOR ON RESIDUAL STRESS DISTRIBUTION

O.V. Makhnenko and **O.S. Kostenevych**
E.O. Paton Electric Welding Institute of the NAS of Ukraine
11 Kazymyr Malevych Str., 03150, Kyiv, Ukraine. E-mail: office@paton.kiev.ua

Substantiation of extension of safe operating life of the vessels of WWER-1000 reactors in service requires taking into account the residual stresses, arising during fabrication as a result of heating at welding or surfacing heating and their redistribution after heat treatment. Automatic submerged-arc surfacing with strip electrodes was used for the cylindrical part of the vessels, and manual coated electrode arc surfacing was applied for the nozzle zone surface (internal surface of nozzles Dn850 and their fillets), as well as other difficult-of-access places of the vessel. The process and parameters of the mode of anticorrosion arc surfacing can markedly influence the microstructural phase composition of the HAZ of base material, 15Kh2NMFA vessel steel, as well as residual stress distribution. Mathematical modeling was used for prediction of microstructural phase transformations in the HAZ, at deposition of the protective anticorrosion layer, based on experimental welding thermokinetic diagram of austenite decomposition of 15Kh2NMFA steel, and distribution of residual stresses in WWER-1000 reactor vessel was derived, allowing for microstructural transformations at different technological modes of arc surfacing. Comparison of the results on residual stress distribution after deposition and heat treatment at different technological modes showed the presence of the zone of compressive stresses, which arise in the HAZ of 15Kh2NMFA steel, as a result of martensite-bainite transformation. 24 Ref., 6 Tables, 15 Figures.

K e y w o r d s : reactor vessel, WWER-1000, anticorrosion arc surfacing, heat-treatment, residual stresses, microstructural phase transformations, mathematical modeling, thermokinetic diagram, 15Kh2NMFA steel

The majority of nuclear power reactors in Ukraine belong to WWER-1000 type, where the vessel is made from thick-walled forged shells from low-alloy high-strength steel of 15Kh2NMFA grade, which are joined by circumferential welds. For corrosion protection the internal surface of the vessel is coated with an anticorrosion layer from austenitic material.

At present the most important scientific-engineering task is extension of safe operating life of the reactor vessels (RV) in service. Its substantiation requires taking into account the residual stresses (RS) arising as a result of heating at welding or surfacing, and their redistribution after heat treatment. Technological parameters of anticorrosion arc surfacing can greatly influence the microstructural phase composition of the heat-affected zone (HAZ) of base material of 15Kh2NMFA vessel steel, as well as residual stress distribution.

In accordance with normative documentation requirements [1], automatic submerged-arc surfacing with a welding strip (the main recommended method), or manual coated electrode arc surfacing or argon-arc surfacing should be used for deposition of anticorrosion coatings on the reactor vessel. In keeping with manufacturing plant documentation [2], automatic submerged-arc surfacing with strip electrodes was used for the RV cylindrical part, and manual coated electrode arc surfacing was applied for the nozzle zone surface (internal surface of nozzles Dn850 and their fillets), as well as for other difficult-of-access places.

RV anticorrosion surfacing was performed in two layers: first layer from austenitic material with increased content of chromium and nickel, Sv-07Kh25N13, second layer also from an austenitic material Sv-04Kh20N10G2B (Sv-08Kh19N10G2B), ensuring the general thickness of the deposited layer of 9 mm [1, 2]. Manual arc surfacing was performed with coated electrodes ZIO-8 (first layer) and EA-898/21B (second layer).

Technological parameters for automatic submerged-arc surfacing (OF-10) with strip electrodes were as follows: [1, 3–6]: current I_w = 600–750 A, voltage U_a = 32–36 V, strip electrode width b = 40–60 mm, preheating and concurrent heating temperature T_h = 100–250 °C, deposition rate v_d = 7–10 m/h; for manual coated electrode arc surfacing [1, 7, 8]: current I_w = 130–150 A, voltage U_a = 26–30 V, 4–5 mm dia electrodes, preheating and concurrent

O.V. Makhnenko — https://orcid.org/0000-0002-8583-0163, O.S. Kostenevych — https://orcid.org/0000-0002-7427-2805

Table 1. Chemical composition of 15Kh2NMFA steel, wt.% [10]

C	Si	Mn	Cr	Ni	Mo	Cu	S	P	V	As	Co
0.13–0.18	0.13–0.37	0.3–0.6	1.8–2.3	1.0–1.5	0.5–0.7	<0.3	<0.02	<0.02	0.10–0.12	<0.04	<0.03

heating temperature T_h = 100–250 °C, deposition rate v_d = 3 m/h.

After processing of the internal surface RV was subjected to heat treatment by high-temperature tempering mode for residual stress relaxation. Maximum heat treatment (HT) temperature could reach 610 °C [2, 6], 620 °C [2, 5], 650–670 °C [1, 9] and soaking duration could be from 5 to 20 h.

Composition of RV base material of 15Kh2NMFA steel (Table 1) was to meet the requirements of TU 108-765–78 [10]. Thermophysical and physicomechanical properties of base material and deposit material are given in [11, 12], depending on temperature.

The work provides comparative analysis of the results of calculations to determine the microstructural phase composition and mechanical properties of the HAZ of RV base material, as well as distribution of residual stresses at different technological modes of anticorrosion surfacing and subsequent heat treatment. The influence of technological parameters of arc surfacing on residual stress distribution was studied, using finite-element model of the nozzle zone of WWER-1000 RV, which includes characteristic sections of surfacing the VR cylindrical part and internal surface of nozzles Dn850 (Figure 1).

Modeling was performed assigning the following technological modes (Table 2): for automatic submerged-arc surfacing of the nozzle zone cylindrical shell, variation of strip electrode width b and preheating temperature T_{pr}, as well as soaking duration at heat treatment was performed. For the internal surface of nozzles Dn850, including the fillets, manual coated electrode arc welding at the nominal mode was modeled.

Two models of surfacing heating source were applied: strip — for automatic submerged-arc surfacing of RV cylindrical shell and spot (or normal-circular), simulating manual coated electrode arc surfacing of the internal surface of nozzle Dn850, as well as the fillets.

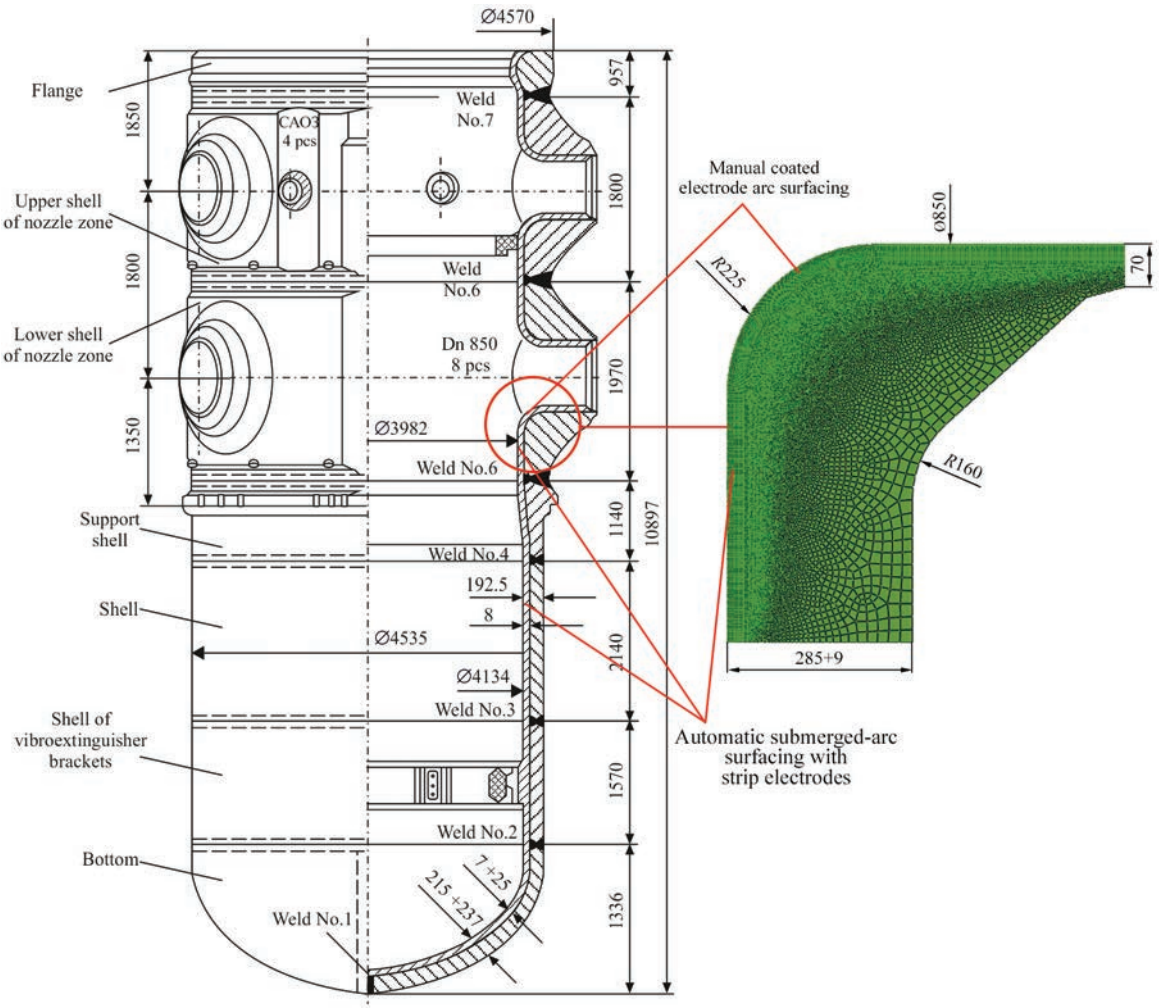

Figure 1. Schematic of location of the zones of manual and automatic surfacing of WWER-1000 RV with an anticorrosion layer and finite-element model of the nozzle zone [1, 2]

Table 2. Modes of arc surfacing and HT assumed in calculations

Current I_w, A	Voltage U_a, V	Efficiency coefficient η	Effective heat input, kJ/mm	Deposition rate v_d, mm/s	Bead width b, mm	Preheating temperature T_{pr}, °C	Soaking time at HT, h (T = 650 °C)
Manual coated electrode arc surfacing							
150	30	0.75	4.066	0.83	15	250	20
150	30	0.75	4.066	0.83	15	250	10
150	30	0.75	4.066	0.83	15	250	5
Automatic submerged-arc surfacing with strip electrodes							
650	32	0.9	9.360	2.0	40	250	20
700	32	0.9	14.608	1.4	60	150	20
700	32	0.9	14.608	1.4	60	250	20
700	32	0.9	14.608	1.4	60	250	10
700	32	0.9	14.608	1.4	60	250	5

Table 3. Results of calculation of HAZ size and cooling rates at different technological parameters of surfacing

Bead width b, mm	Preheating temperature T_{pr}, °C	FZ depth, mm	HAZ depth in base material, mm	Cooling rate w (800–500 °C), °C/s
15 (manual surfacing)	250	1	7	8–11
40	250	1	9	4–5
60	250	1	10	3–4
60	150	1	8	5–7

The problem of nonstationary heat conductivity in arc surfacing was solved in a two-dimensional definition with the assumption of a fast moving heat source and axial symmetry at sequential deposition of surfacing passes with step-by-step tracing in time from the start of heating of metal in each deposited pass to cooling to the temperature of concurrent heating. Distribution of thermal power of strip source W_1 and point source W_2 in the two-dimensional definition in a cylindrical system of coordinates can be represented by the respective dependencies (1) and (2) [13]:

$$W_1(r,z,t) = \frac{2Q\sqrt{K_r K_z}}{\pi v_h t_h \left[1+\sqrt{\frac{K_z}{\pi}}b\right]} \times \exp\left[-K_r(r-r_0)^2 - K_z(z-z_0)^2\right]; \quad (1)$$

$$W_2(r,z,t) = \frac{2Q\sqrt{K_r K_z}}{\pi v_h t_h} \times \exp\left[-K_r(r-r_o)^2 - K_z(z-z_o)^2\right], \quad (2)$$

where r, z are the coordinates (radial and axial) of the considered RV point; r_0, z_0 are the coordinates of the center of moving heat source; K_r, K_z are the concentration coefficients of the specific heat flow; t_h is the heating time; Q is the effective power of the heat source ($Q = \eta I_w U_a$); η is the coefficient of heat source efficiency; v_d is the deposition rate; b is the strip electrode width.

Derived calculation results of maximum temperature distributions and characteristic thermal cycles at deposition allowed evaluation of the dimensions of the fusion zone (FZ) and HAZ, as well as cooling rate

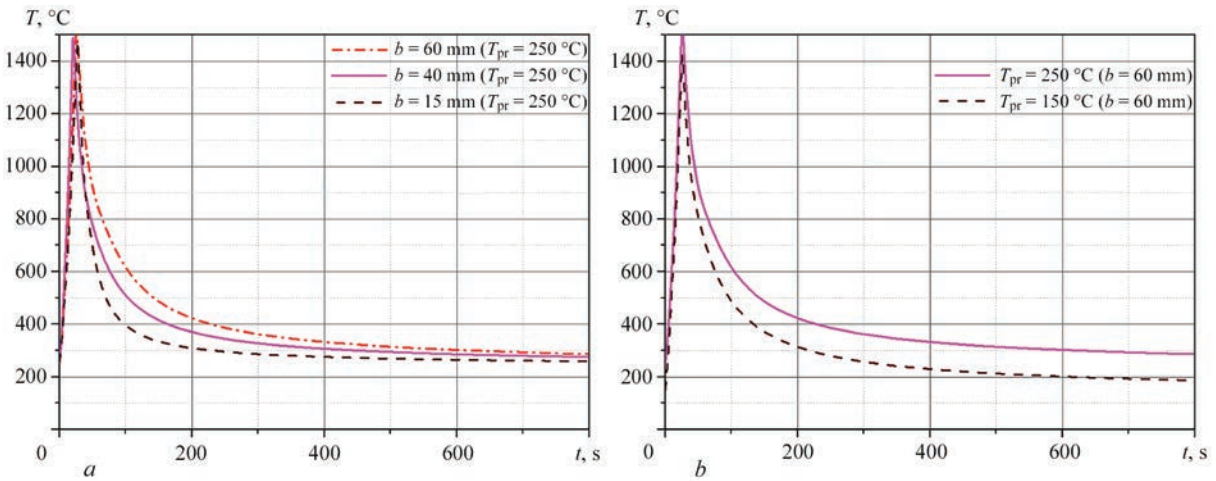

Figure 2. Characteristic thermal cycles at variation of: *a* — bead width; *b* — preheating temperature, T_{pr}

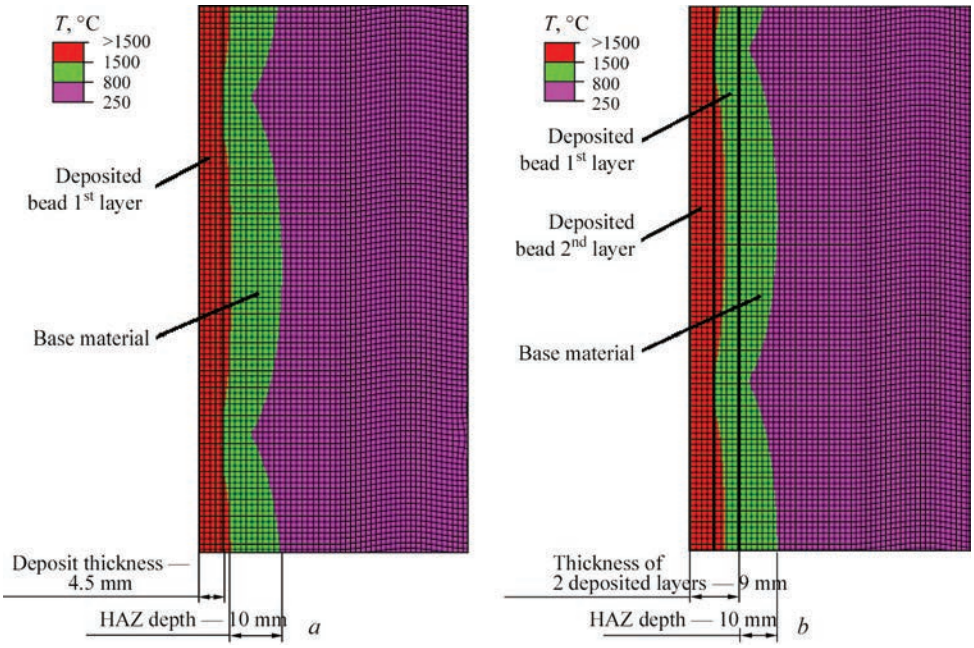

Figure 3. Characteristic dimensions of FZ (T > 1500 °C) and HAZ (1500 °C > T> 800 °C) for submerged-arc surfacing with strip electrodes of: *a* — first layer; *b* — second layer

of the metal in reactor vessel surfaced zones at different technological modes (Figure 2, Table 3). Results were obtained for different bead widths b: at automatic arc surfacing with strip electrodes — 40, 60 mm, at manual coated electrode arc welding — 15 mm, and at different preheating temperatures T_{pr} for automatic surfacing that are equal to 150 and 250 °C.

From the viewpoint of microstructural transformations, important is the size (depth) of the HAZ in base material. As after the second deposited layer the HAZ shifts by the value of the first layer width, the depth of the HAZ in base material is actually determined as a result of deposition of the first layer. One can see by the results (Table 3, Figure 2) that the minimum HAZ size in base material (up to 7 mm depth) and maximum rate of HAZ metal cooling in the temperature range of 800–500 °C (8–11 °C/s) were derived for manual coated electrode arc surfacing of nozzle Dn850. Rather high cooling rate (5–7 °C/s) was obtained for arc surfacing with strip electrode of width b = 60 mm at preheating temperature of 150 °C. The lowest cooling rate (3–4 °C/s) and the greatest depth of the HAZ in base material (up to 10 mm) were obtained for the mode of arc surfacing with strip electrode at b = 60 mm and preheating temperature of 250 °C (Figure 3).

FZ chemical composition can differ essentially from that of the filler material, as a result of mixing with the base metal. In keeping with [7], the mixing ratio g_0 (%), namely the fraction of base metal in the deposited metal depends on the deposition mode and is determined as follows:

$$g_0 = \frac{F_{BM}}{F_{BM} + F_d} 100\ \%, \qquad (3)$$

where F_0 is the cross-sectional area of molten base metal; F_d is the cross-sectional area of the deposited metal.

Microstructural phase composition in FZ taking into account the mixing of base and filler metal, can be approximately determined according to Schaeffler structural diagram [14] based on the values of equivalent nickel and chromium:

$$\begin{pmatrix} Ni_{eq} = \%\,Ni + 30 \cdot \%\,C + 0.5 \cdot \%\,Mn \\ Cr_{eq} = \%\,Cr + \%\,Mo + 1.5 \cdot \%\,Si + 0.5 \cdot \%\,Nb \end{pmatrix}. \qquad (4)$$

Results of calculation of mixing ratio and approximate microstructural phase composition in the FZ, according to Schaeffler diagram, are given in Table 4 at increase of the heat input from the nominal value by 10, 20, 30, 40 %.

Calculation of microstructural phase composition, according to Schaeffler diagram [14] for different FZ regions at essential deviations of the heat input values from the nominal one, showed that in terms of formation of an austenitic structure in FZ, 30 % increase of the heat input is a critical value for automatic submerged-arc surfacing with strip electrode and 40 % increase is a critical value for manual coated electrode arc surfacing. This is indicative of reliable formation of austenitic structure in the FZ (up to 5–10 % content of ferrite) at nominal values of the heat input. At mathematical modeling of temperature distributions, it was found that the critical value of the mixing ratio,

Table 4. Determination of mixing ratios at heat input variation

Increase of heat input against nominal value, %	Area of deposited bead, mm²	Area of molten base metal, mm²	Mixing ratio g_0, %	Ni_{eq}	Cr_{eq}	Austenite in FZ, %
0	180 (automatic submerged-arc surfacing with strip electrode b = 40 mm)	26	13	14.7	22.5	90–95
10		52	23	13.7	20.3	95–100
20		86	32	12.8	18.1	100
30		110	38	12.2	16.8	a+m+f
0	67 (manual coated electrode arc surfacing	13	16	14.3	21.7	90–95
10		21	23	13.7	20.2	95–100
20		27	28	13.2	19.0	95–100
30		36	35	12.5	17.6	100
40		43	39	12.1	16.6	a+m+f

Table 5. Numerical data from TKD of austenite decomposition in 15Kh2NMFA steel under characteristic thermal cycle of welding/surfacing conditions

Cooling rate w_j, °C/s	Transformation temperatures at cooling stage, °C				Bainite V_b/martensite V_m fraction, %	Hardness $HV1$, kgf/mm²
	B_s	B_f	M_s	M_f		
3	485	315	343	315	98/2	383
4	478	343	343	280	80/20	380
5	468	425	425	298	10/90	426

non-exceeding which ensures formation of the austenitic structure in the FZ, is equal to g_0 = 38–39 % at nominal values of g_0 = 13–16 % (Table 4). Therefore, further mathematical modeling of microstructural phase composition, mechanical properties and stress-strain state in RV surfaced zone did not take into account the filler material mixing with base metal in the FZ or the change of chemical composition of austenitic deposit material.

Modeling of microstructural phase transformations in low-alloy steel HAZ during welding or surfacing can be performed using the approach based on application of parametric (regression) equations derived at PWI [15, 16]. In this work, mathematical modeling of microstructural transformations in the HAZ of 15Kh2NMFA steel was performed with application of thermokinetic diagram (TKD) of austenite decomposition for characteristic welding/surfacing cycles exactly for 15Kh2NMFA steel. For this purpose, physical modeling of microstructural transformations in the HAZ of RV base material at arc surfacing in Gleeble3800 unit, and metallographic analysis of 15Kh2NMFA steel samples were performed [13]. Physical modeling results are presented in [13] in the form of two plotted TKD of austenite decomposition for characteristic cycles of welding/surfacing at different cooling rates w_j in the temperature range of 800–500 °C and at different maximum heating temperatures (1000 and 1350 °C). For convenience of mathematical modeling of microstructural transformations in the HAZ of 15Kh2NMFA steel, the welding TKD of austenite decomposition, averaged relative to maximum heating temperature, which is proposed in [17], was used. It is plotted for different cooling rates w_j in the characteristic temperature range of 800–500 °C (Figure 4, Table 5).

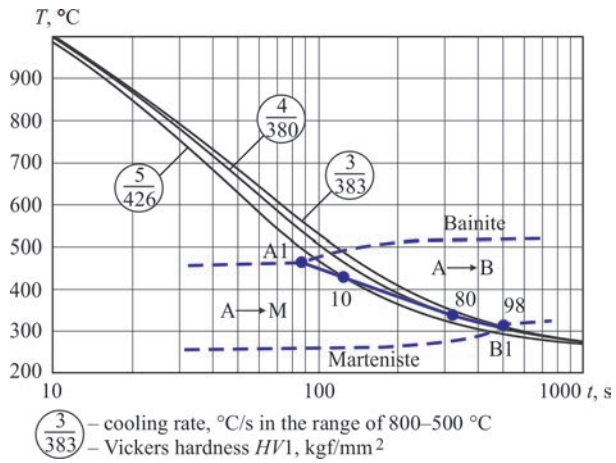

Figure 4. Thermokinetic diagram of austenite decomposition in 15Kh2NMFA steel for characteristic cooling cycles at welding [17]

The numerical data of TKD of 15Kh2NMFA steel [17] (Table 5) allow deriving the interpolation dependencies for all the TKD parameters (temperature of the start of bainite B_s and martensite transformation M_s, finish of bainite B_f and martensite transformation M_f, maximum fraction of martensite $V_{m.max}$ and $V_{b.max}$) for intermediate cooling rates w.

It was experimentally established that the initial microstructure of samples from 15Kh2NMFA steel is bainite with a small fraction of martensite of up to 3–5 % (Figure 5). Hardness of Vickers samples is $HV1$ = 315–325 kgf/mm² (3150–3250 MPa). Bainite grain size is 15–20 μm (8–9 grain size number to ASTM). Experimental data are in good agreement

with the available data [18, 19] as to the initial microstructural state of 15Kh2NMFA steel.

Figures 6 and 7 show the derived results of calculation of the weight fraction of each microstructural phase during surfacing and in the final microstructure of base material HAZ after cooling, according to numerical data of 15Kh2NMFA steel TKD.

Calculated data according to Figure 6, obtained on the base of experimental TKD of austenite decomposition in 15Kh2NMFA steel showed that heating at submerged-arc surfacing with strip electrodes (b = = 60 mm) resulted in formation of a small fraction of martensite of up to 15 % at preheating temperature T_{pr} = 250 °C (cooling rate of 3–4 °C/s) and formation of a predominant content of 90 % martensite in the final microstructure at preheating temperature T_{pr} = = 150 °C (cooling rate of 5–7 °C/s) (Figure 6).

Comparison of the results for the two values of strip electrode width (Figure 7) at anticorrosion surfacing showed that at the width b = 40 mm the fraction of martensite formed in the HAZ is 70–90 %, and at the width of b = 60 mm — it is up to 15 % martensite. At manual coated electrode arc surfacing (b = = 15 mm) martensite content in the final microstructure after cooling is equal to 90 %.

Results of mathematical modeling of microstructural phase composition of 15Kh2NMFA steel HAZ

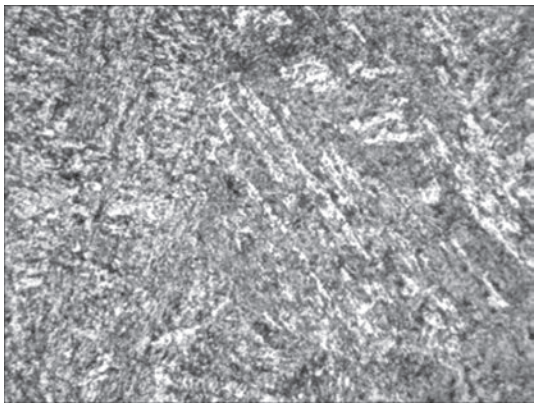

Figure 5. Initial bainite microstructure (×500) of 15Kh2NMFA steel samples

after two layers of anticorrosion surfacing for different technological modes are summarized in Table 6.

Derived calculation data on formation of bainite-martensite microstructure of 15Kh2NMFA steel, as a result of RV anticorrosion surfacing, agree quite well with published results [9, 20, 21].

Change of microstructural phase composition leads to a change of mechanical properties in HAZ of RV base material. The yield limit of each microstructural phase was determined, depending on chemical composition and temperature, based on the parametric regression equations [16].

The stress-strain state of material in RV surfaced zone was modeled using the thermo-viscoplasticity

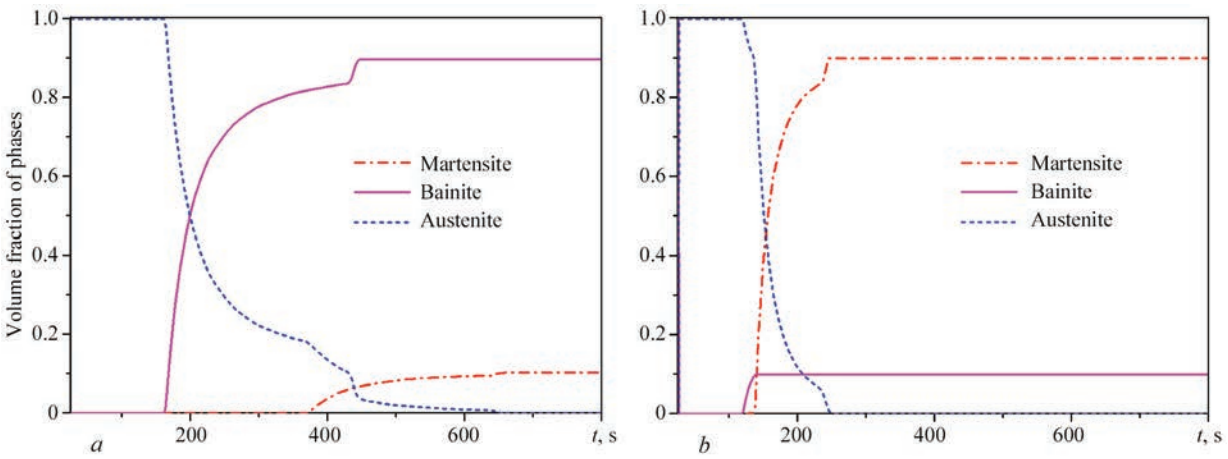

Figure 6. Results of prediction of the kinetics of austenite decomposition in HAZ metal at arc surfacing with strip electrode (b = = 60 mm) with preheating up to 250 (*a*), 150 (*b*) °C

Table 6. Results of calculation of microstructural phase composition in the HAZ of RV base material (15Kh2NMFA steel) for different technological modes of surfacing

Technological mode	Calculated data acc. to TKD, %	
	Martensite	Bainite
b = 15 mm (manual surfacing), T_{pr} = 250 °C, w = 8–11 °C/s	90	10
b = 40 mm, T_{pr} = 250 °C, w = 4–5 °C/s	70–90	10–30
b = 60 mm, T_{pr} = 250 °C, w = 3–4 °C/s	15	85
b = 60 m, T_{pr} = 150 °C, w = 5–7 °C/s	90	10

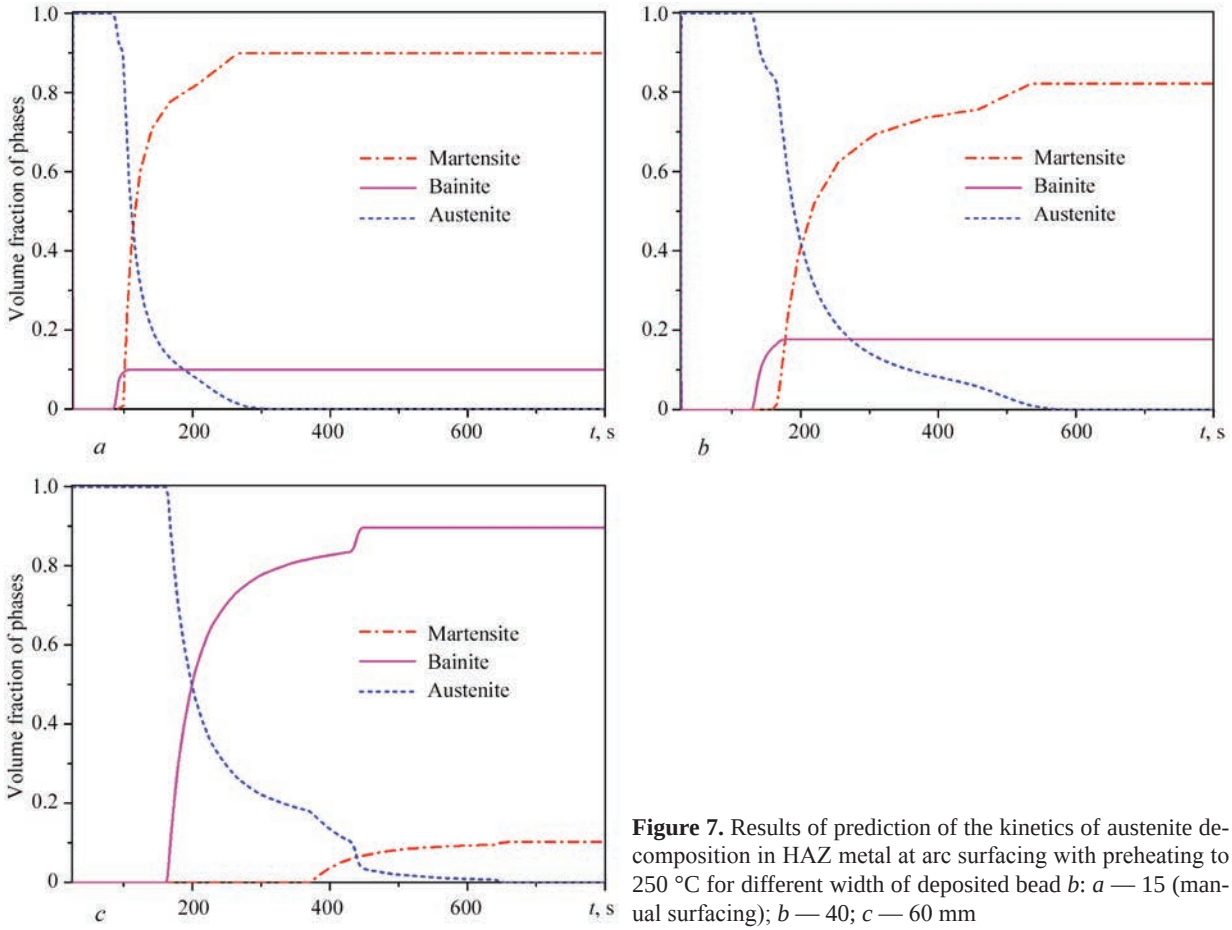

Figure 7. Results of prediction of the kinetics of austenite decomposition in HAZ metal at arc surfacing with preheating to 250 °C for different width of deposited bead *b*: *a* — 15 (manual surfacing); *b* — 40; *c* — 60 mm

model [22], for which the solution of the fundamental equations was derived by the finite element method.

Obtained were the results for residual stresses, allowing for microstructural phase transformations, based on application of experimental TKD at different technological modes of arc surfacing. Allowing for microstructural transformations and periodicity (in the transverse direction) of bead deposition on RV surface leads to nonuniform distribution of RS, appearance of compressed zones in base metal HAZ, and also influences the quantitative value of stresses. Figures 8–10 show the distribution of RS circumferential $\sigma_{\beta\beta}$ and axial σ_{zz} components in characteristic sections 1–1, 2–2.

Comparing calculation results at different widths of the deposited bead *b* = 15, 40, 60 mm (Figure 9, *a*, *b*) it was established that after two layers of deposition for all the cases of bead width, compressive circumferential RS of up to (–300– –600 MPa) were obtained in section 1–1 in base material HAZ; and the width of the compressive stress zone is equal to the depth of HAZ in the base material, while in section 2–2 we have tensile circumferential RS of up to 600 MPa in the HAZ.

After manual arc surfacing (*b* = 15 mm), the maximum value of tensile circumferential RS is up to 750 MPa, HAZ depth is up to 7 mm and the depth of

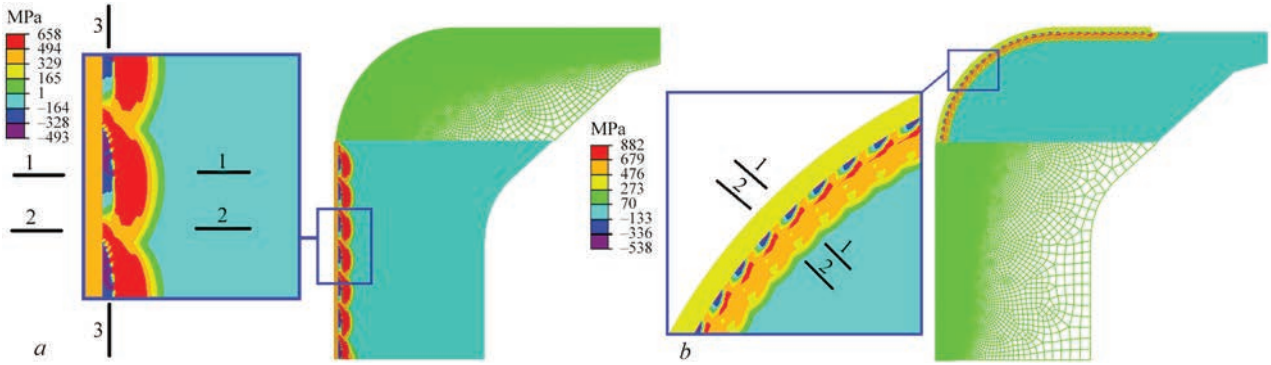

Figure 8. Distribution of circumferential RS $\sigma_{\beta\beta}$ in the cross-section of RV surfaced zone: *a* — for automatic arc surfacing with strip electrodes; *b* — for manual coated electrode arc surfacing

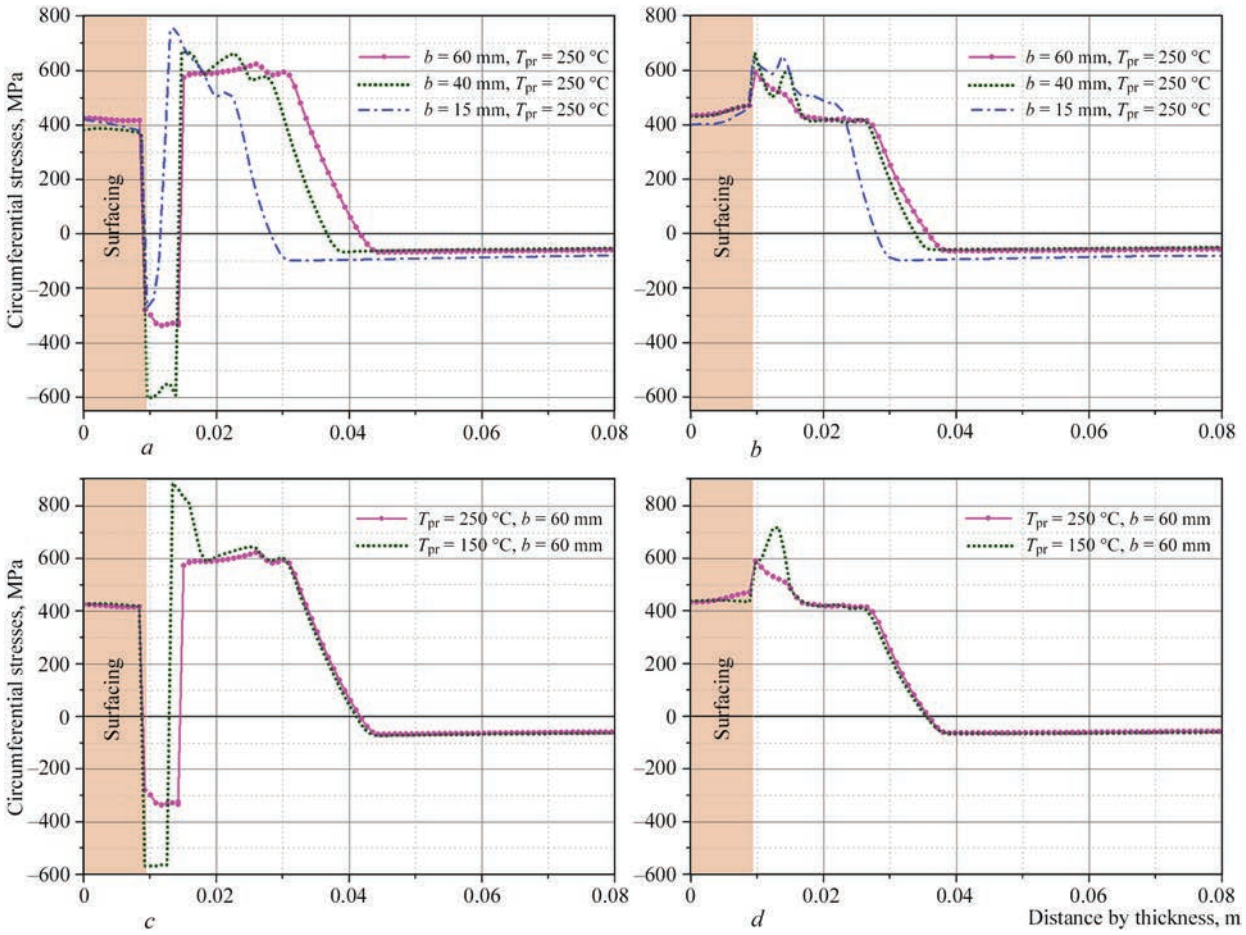

Figure 9. Distribution of circumferential RS $\sigma_{\beta\beta}$ by RV thickness after surfacing. Variation of bead width: *a* — section 1–1; *b* — 2–2. Variation of preheating temperature: *c* — section 1–1; *d* — 2–2

tensile stress zone is up to 28 mm from the deposition surface.

At surfacing with strip electrode at bead width b = 60 mm, the depth of base material HAZ is much greater and is equal up to 10 mm, at b = 40 mm it is equal up to 9 mm, the depth of tensile stress zone is equal up to 36 mm (section 2–2) — 42 mm (section 1–1) and 34 mm (section 2–2) — 36 mm (section 1–1), respectively, from the deposition surface. Maximum tensile circumferential RS for both the values of strip electrode width are close in value (600–650 MPa).

For different temperature of preheating and concurrent heating at surfacing with strip electrodes of width b = 60 mm it was found (Figure 9, *c*, *d*) that after surfacing at preheating temperature of 150 °C compressive circumferential RS of up to –570 MPa form in section 1-1 of base material, HAZ depth in base material is up to 8 mm, while at preheating temperature of 250 °C lower compressive RS — on up to –330 MPa level were obtained, but in a wider zone of base material HAZ, of up to 10 mm. Tensile circumferential RS in base material in the case of application of electrode of width b = 60 mm at preheating temperature of 150 °C locally reach the value of 840 MPa, at the temperature of 250 °C they do not exceed 600 MPa, while the depth of tensile stress zone reaches 42 mm from the deposition surface.

As regards axial component σ_{zz}, Figure 10 shows RS distribution after surfacing by the thickness RV cylindrical part in characteristic sections 1–1, 2–2, depending on the width of strip electrode and preheating temperature. Base material HAZ in RV cylindrical part has compressive RS (up to –400– –825) MPa in section 1–1, up to (–30– –200) MPa in section 2–2. Magnitude of tensile RS in the base material, allowing for microstructural transformations, is equal up to (500–620 MPa) in section 1–1 and up to (250–300 MPa) in section 2–2.

At modeling of the technological process of general (furnace) heat treatment (HT) the high-temperature tempering mode at the temperature of 650 °C for up to 20 h was specified. Stress relaxation was modeled, using the function of temperature creep of material, which in [23] was determined based on available experimental data for 15Kh2NMFA steel [9]. In particular, calculation of creep strains by the finite element method was performed using the equation correlating the rate of equivalent creep strain $d\varepsilon_{eq}^{c}$ with stress intensity σ_i in the form of Norton–Bailey law [24]:

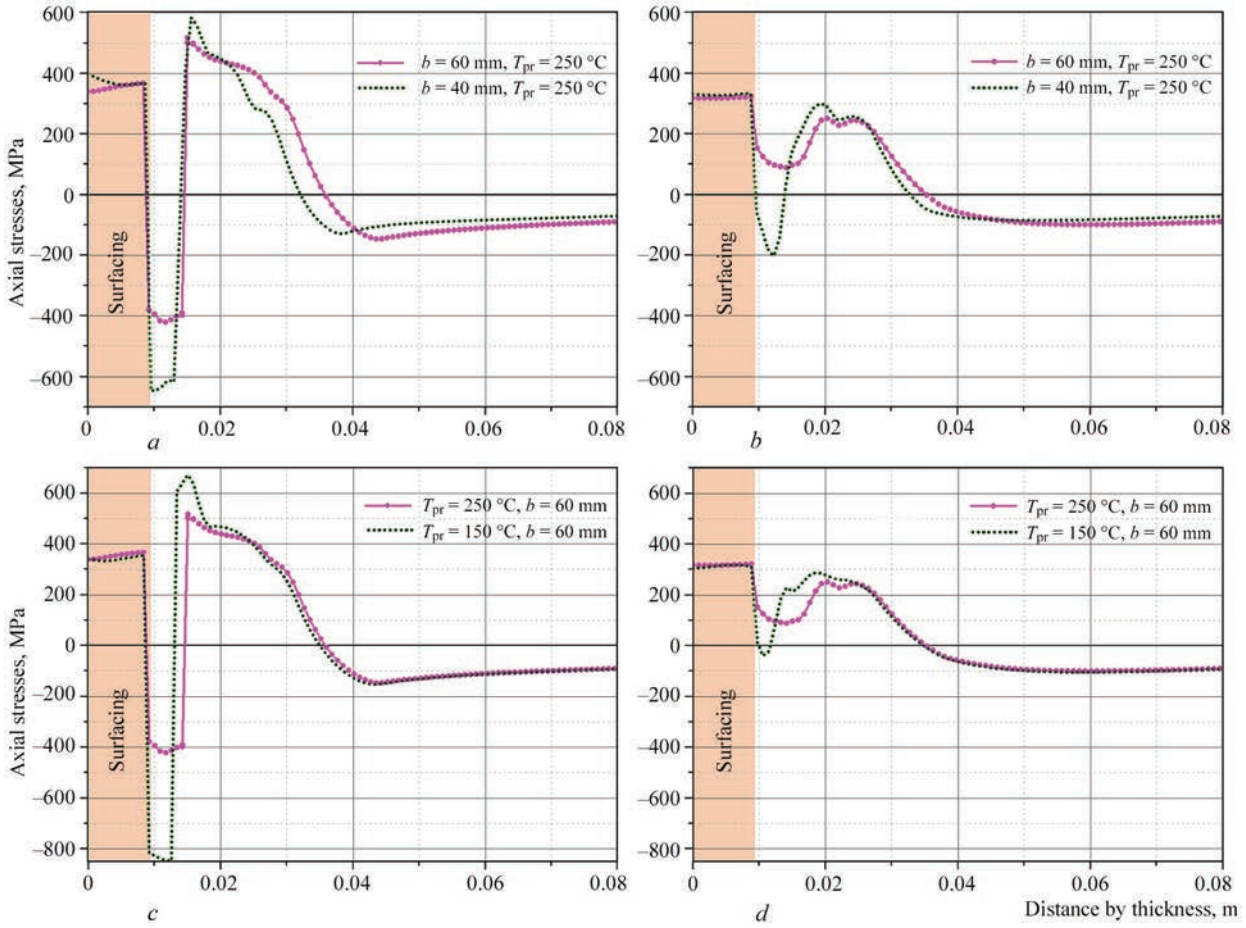

Figure 10. Distribution of axial RS σ_{zz} by RV thickness after surfacing. Variation of bead width: *a* — section 1–1; *b* — 2–2. Variation of preheating temperatures: *c* — section 1–1; *d* — 2–2

$$d\varepsilon_{eq}^{c} = A\sigma_i^n dt, \quad (5)$$

where A, n are the material constants, taking into account [9, 23] for 15Kh2NMFA steel $A = 0.17 \cdot 10^{-20}$(1/(MPa^6·s), $n = 6$.

HT by high-temperature tempering mode markedly lowers the level of residual stresses in RV base material, caused by anticorrosion surfacing. Figures 11–15 give the distributions of the circumferential and axial components of residual stresses by RV thickness after surfacing and HT performance for different technological modes. Tensile stresses on the level of austenitic material yield limit (up to 400 MPa) remain in the austenitic deposit material, because of the difference from the base material in the coefficients of temperature expansion.

Comparison of the results on circumferential RS, obtained by modeling the HT by the high-temperature tempering mode (T = 650 °C, 20 h soaking) at different width of the deposited beads and preheating temperature T_{pr} = 250 °C at surfacing showed (Figure 11, *a*, *b*) that manual arc surfacing with coated electrodes (b = 15 mm), compressive residual stresses of up to –325 MPa were obtained in base material HAZ. At automatic surfacing with strip electrode of width b = 40 mm a zone of compressive stresses of up to –330 MPa (section 2–2) and up to –500 MPa (section 1–1) was obtained in base material HAZ; at b = 60 mm the compressive stress zone (–200 MPa) (section 1–1) and the zone of tensile stresses on the level of 50 MPa (section 2–2) was formed in base material HAZ. Maximum value of tensile circumferential RS in the base material is not more than 170 MPa.

The level of circumferential residual stresses in the compression zone after HT by the mode of high-temperature tempering at a lower preheating temperature, T_{pr} = 150 °C, at surfacing is higher than that of stresses at T_{pr} = 250 °C, due to formation of a greater fraction of martensite. At automatic surfacing with strip electrodes of width b = 60 mm at preheating temperature T_{pr} = 150 °C the maximum compressive circumferential stresses can be up to (–370– –450 °C) MPa, width of the compressive zone can reach 3 mm (section 2–2) — 7 mm (section 1–1) of base material, and the depth of tensile stress zone almost does not change: up to 35 mm (section 2–2) and up to 42 mm (section 1–1) from the deposit surface (Figure 11, *c*, *d*).

Figure 12 presents the distribution of RS axial component σ_{zz} by the thickness of RV cylindrical part in characteristic sections 1–1, 2–2 after surfacing and

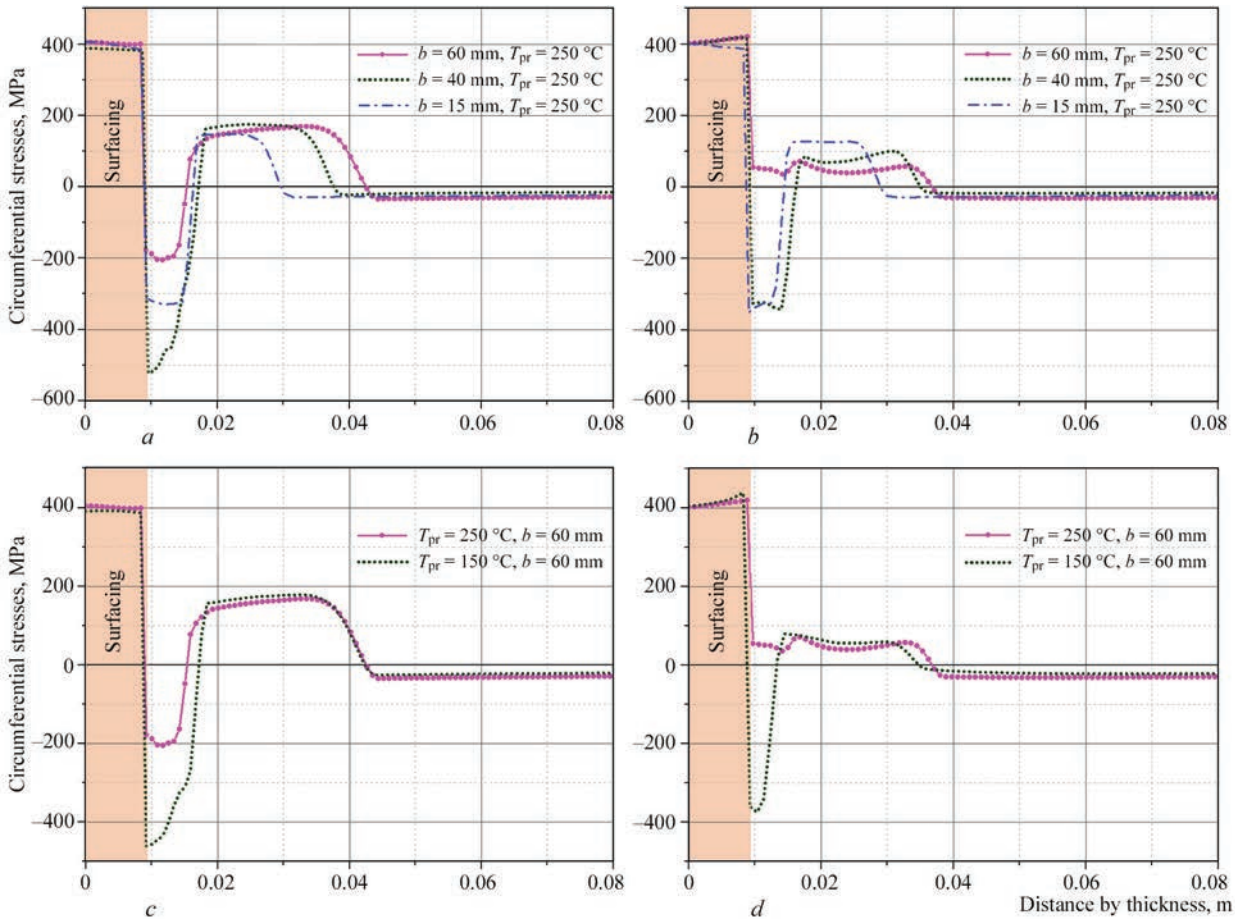

Figure 11. Distribution of circumferential RS $\sigma_{\beta\beta}$ by RV thickness after surfacing and HT (T = 650 °C, 20 h soaking). Variation of bead width: *a* — section 1–1, *b* — 2–2. Variation of preheating temperature: *c* — section 1–1; *d* — 2–2

HT by high-temperature tempering mode. The magnitude of compressive axial residual stresses, allowing for microstructural transformations in the HAZ, reaches (–220– –550) MPa in section 1–1, and (–50– –500) MPa in section 2–2. Maximum value of tensile axial residual stresses in base material does not exceed (100–120) MPa (section 1–1).

Nonuniformity of RS distribution (Figure 8, Figure 13) after surfacing (T_{pr} = 250 °C) and HT (T = 650 °C, soaking for 20 h) in the transverse direction of bead deposition (section 3-3), at 12 mm depth for the deposit surface) is represented by periodicity of values of circumferential RS from –200 to 50 MPa (strip electrode width b = 60 mm) and from –570 to 310 MPa (strip electrode width b = 40 mm). For the case of manual arc surfacing (b = 15 mm) we have an almost uniform compression zone of circumferential RS on the level of –350 MPa and slight periodicity of distribution of axial RS from –420 to –350 MPa. Axial residual stresses in the case of surfacing by strip electrodes change from –230 to –50 MPa (b = 60 mm) and from –500 to –375 MPa (b = 40 mm).

Thus results of distribution of the circumferential and axial components of residual stresses by RV thickness and in the transverse direction of bead deposition after surfacing and HT by the mode of high-temperature tempering for different technological modes showed that reduction of preheating temperature at surfacing from 250 to 150 °C leads to the HAZ narrowing and simultaneous significant increase of the magnitudes of compressive circumferential and axial RS in base material HAZ and of the width of compressive RS zone due to increase of the volume fraction of martensite component in the final microstructure. Increase of strip electrode width at surfacing leads to greater depth of the HAZ in base material, as well as of tensile RS zone. Here, narrowing of the compressive RS zone and lowering of the magnitude of compressive RS, both circumferential and axial, in the HAZ, was established due to reduction of volume fraction of the martensite component in the final microstructure.

According to Table 2, soaking duration was varied when modeling the technological operation of HT by high-temperature tempering mode at temperature T = = 650 °C, namely 5, 10 and 20 h. The results of calculation of the distribution of circumferential residual stresses by thickness, depending on soaking duration at HT are shown in Figure 14 for the case of surfacing with strip electrode b = 60 mm and in Figure 15 for

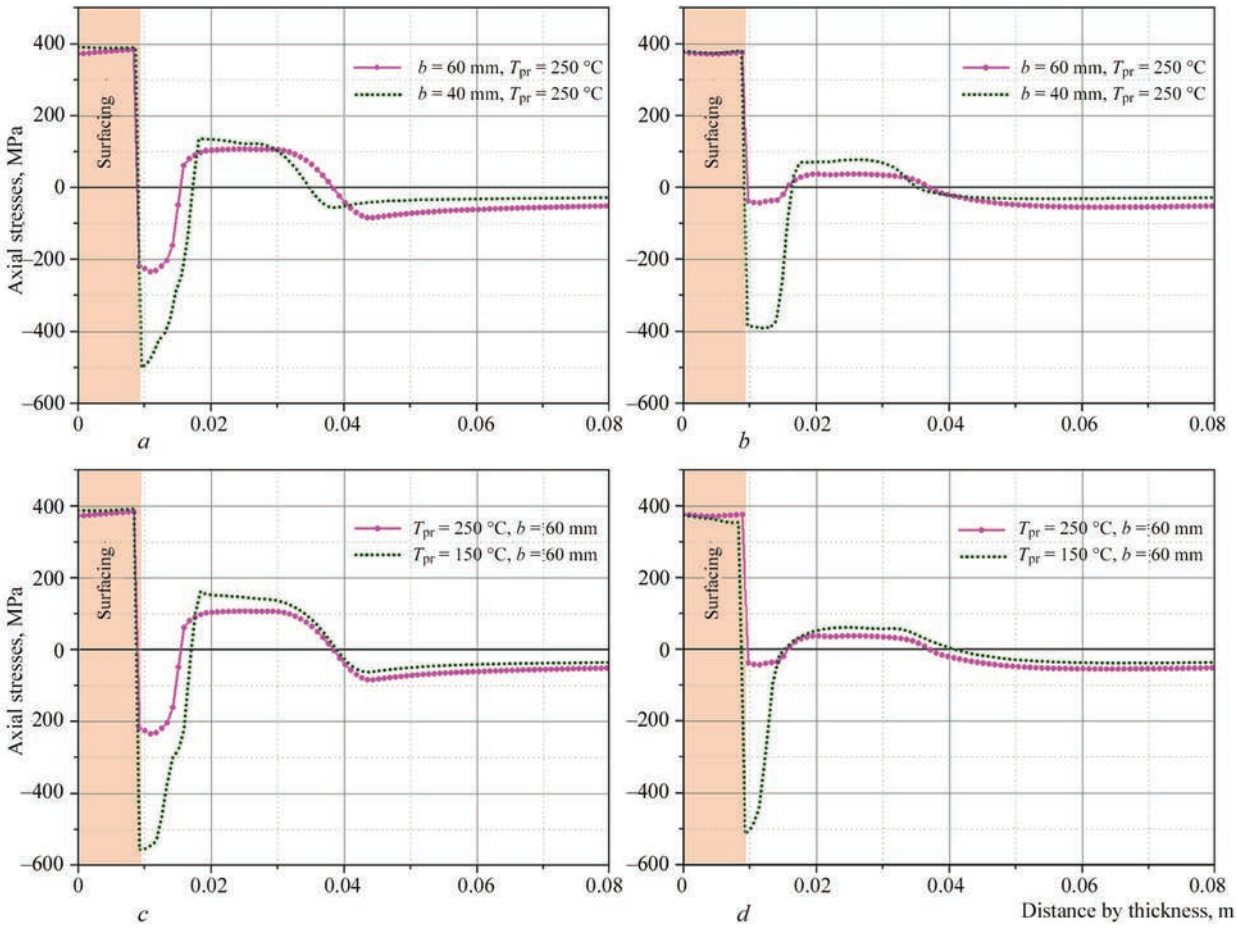

Figure 12. Distribution of axial RS σ_{zz} by RV thickness after surfacing and HT (T = 650 °C, 20 h soaking). Variation of bead width: *a* — section 1–1; *b* — 2–2. Variation of preheating temperature: *c* — section 1–1; *d* — 2–2

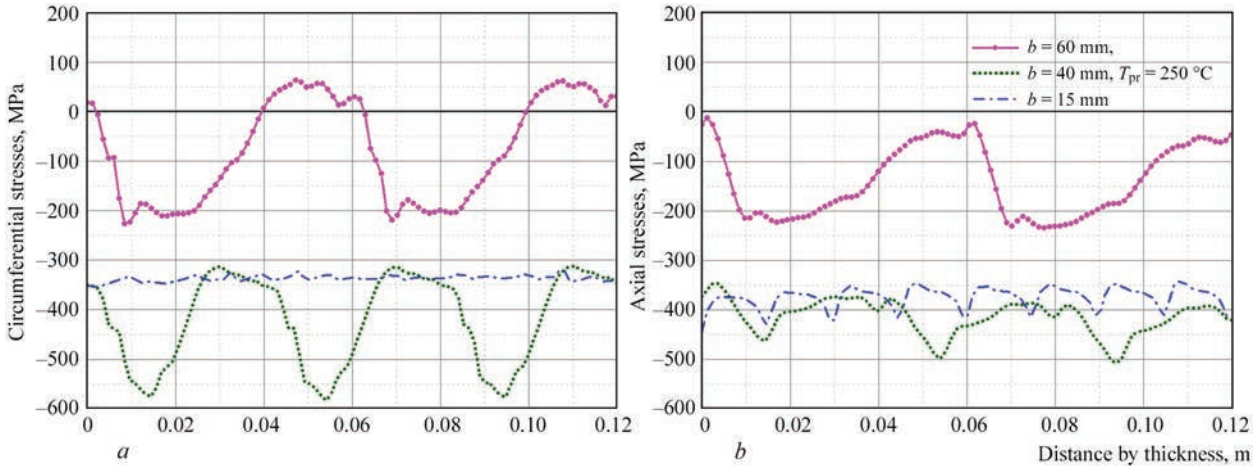

Figure 13. Distribution of circumferential $\sigma_{\beta\beta}$ (*a*) and axial σ_{zz} (*b*) RS after RV surfacing and HT (T = 650 °C, 20 h soaking) in base material HAZ in section 3–3 (in transverse direction of bead deposition, at 12 mm depth from deposit surface)

the case of manual surfacing with coated electrodes, b = 15 mm.

The results (Figure 14) show that the maximum level of tensile RS in base material after 5 h soaking at HT decreased to 220 MPa, after 10 h — to 200 MPa, and after 20 h — to 170 MPa (section 1–1). Maximum magnitudes of compressive stresses in the HAZ were also obtained at 5 h soaking duration, namely –235 MPa.

For coated electrode manual arc surfacing (Figure 15), lowering of the maximum level of tensile RS in base material to 200 MPa was obtained at HT after 5 h soaking, to 175 MPa after 10 h, and to 150 MPa after 20 h (section 1–1). In base material HAZ lowering of maximum magnitude of compressive stresses to –330– –350 MPa was achieved at 5 h soaking duration.

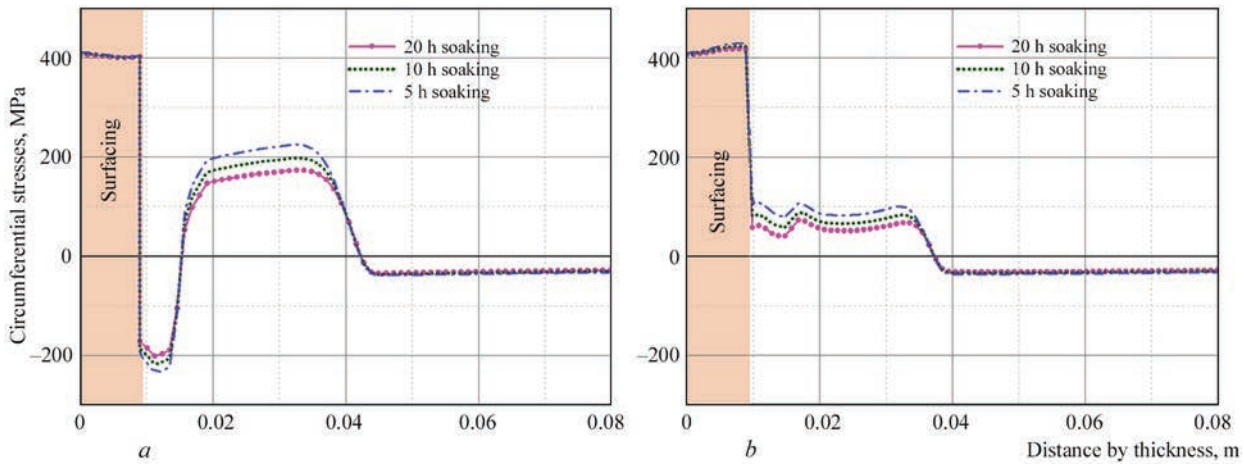

Figure 14. Distribution of circumferential RS $\sigma_{\beta\beta}$ by RV thickness for two characteristic sections at variation of heat treatment mode (soaking duration at $T = 650$ °C) for the case of submerged-arc surfacing with strip electrode $b = 60$ mm: *a* — section 1–1; *b* — section 2–2

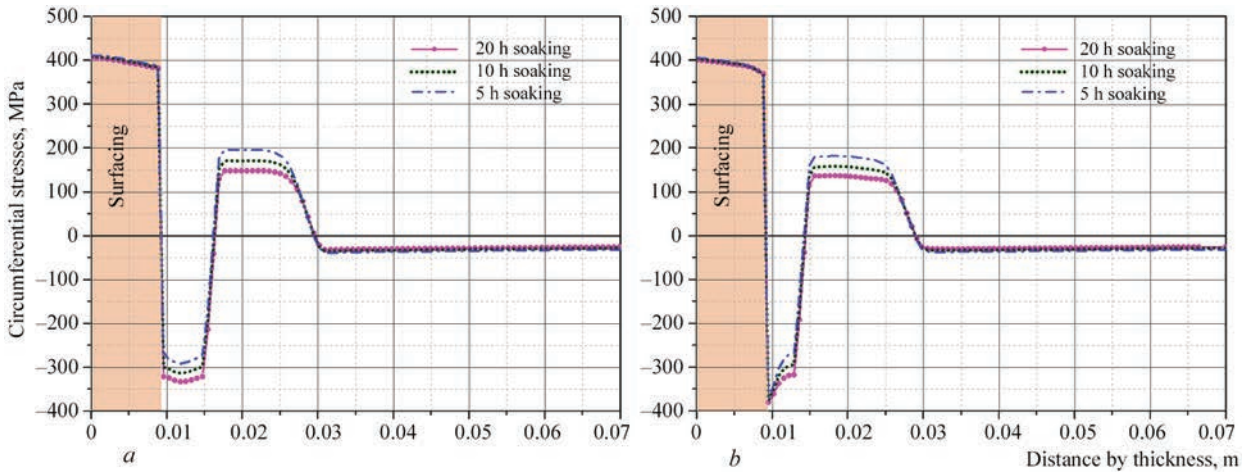

Figure 15. Distribution of circumferential RS $\sigma_{\beta\beta}$ by RV thickness in two characteristic sections at variation of heat treatment mode (soaking duration at $T = 650$ °C) for the case of manual arc surfacing with coated electrodes $b = 15$ mm: *a* — section 1–1; *b* — section 2–2

Conclusions

1. For WWER-1000 RV made from low-alloyed high-strength 15Kh2NMFA steel, on the internal surface of which an anticorrosion layer from austenitic material was deposited by two different technologies: automatic submerged-arc surfacing with strip electrodes of RV cylindrical part and manual coated electrode arc surfacing of the internal surface of the nozzles, calculated data were obtained as regards the kinetics of temperature distribution, cooling rates, FZ and HAZ dimensions and kinetics of microstructural phase transformations.

2. As a result of modeling the microstructural phase composition by the data of welding TKD for 15Kh2NMFA steel, martensite content from 15 to 90 % in base material HAZ was obtained for submerged-arc strip surfacing of RV cylindrical part, and predominant martensite content of up to 90 % for manual coated electrode arc surfacing of the internal surface of nozzle Dn850. Thus, technologies of arc surfacing with an anticorrosion layer of the internal surface, currently used in WWER-1000 RV manufacture, despite preheating up to 150–250 °C led to formation of a phase structure with high martensite content to the depth of up to 10 mm in base material HAZ.

3. A significant influence of variation of technological parameters of the surfacing and heat treatment process (strip electrode width, preheating temperature, soaking duration at heat treatment) on RS distribution in the surfaced zone of WWER-1000 RV was revealed. Analysis of the comparison of calculated RS distribution, allowing for microstructural phase transformations, showed the following main features, namely owing to the periodicity of deposition of the surfacing passes (beads) and formation of bainite-martensite microstructure, the base material HAZ develops a significant nonuniformity of RS distribution in the transverse direction of deposition and a zone of compressive stresses on the level of (–200–550) MPa of up to 7 mm width at the depth from 9 to 16 mm from the deposit surface. Then, at the depth

from 16 to 42 mm they change to tensile stresses of the maximum level of up to 170 MPa. In the austenitic deposited material tensile stresses on the level of the austenitic material yield limit (up to 400 MPa) remain even after HT, because of the difference in thermal expansion coefficients with the base material.

4. It was found that lowering of preheating temperature from 250 to 150 °C at surfacing leads to an essential increase of volume fraction of martensite component in the final microstructure and increase of the magnitude of compressive circumferential and axial RS in the HAZ, as well as to increase of the width of the compressive RS zone.

5. Increase of the strip electrode width to b = = 60 mm at surfacing leads to a significant increase of the width of the HAZ, as well as tensile RS zone in base material. Here, a lowering of the magnitude of compressive RS, both circumferential and axial in the HAZ, and reduction of the compressive RS zone was found at reduction of the volume fraction of martensite component in the final microstructure.

6. Increase of soaking duration at high-temperature annealing temperature of 650 °C promotes RS relaxation in the base material, particularly, lowering of the magnitude of maximum tensile circumferential stresses from (220–200) MPa at 5 h soaking to (170–150) MPA at 20 h soaking.

1. (2003) PNAE G-7-009–89: Equipment and pipelines of nuclear power plants. *Welding and surfacing, basic provisions.* Moscow [in Russian].
2. (1982) Welded vessel 1152.02.70.000. *Appendix to pressure vessel certificate 1152.02.70.000 D7, ZNPP, bl. 1* [in Russian].
3. Titova, T.I.,Shulgan, N.A. (2013) Improvement of quality of welded joints and deposited surfaces of NPP equipment OJSC production «Izhorskie zavody». In: *Proc. of Conf. on Ensuring the Safety of NPP with WWER*, St.-Petersburg, Gidropress [in Russian]. http://www.gidropress.podolsk.ru/files/proceedings/mntk2013/autorun/article95ru.htm
4. Iradj, Sattari-Far, Magnus, Andersson (2006) *Cladding effects on structural integrity of nuclear components.* SKI Report 2006:23, ISSN 1104-1374, ISRN SKI-R-06/23-SE.
5. Katsuyama, J., Udagawa, M., Nishikawa, H. et al. (2010) Evaluation of weld residual stress near the cladding and J-weld in reactor pressure vessel head for the assessment of PWSCC behavior. *Japan Society of Maintenology. E-J. of Advanced Maintenance*, **2**, 50–64.
6. Dupas, P., Moinereau, D. (1996) Evaluation of cladding residual stresses in clad blocks by measurements and numerical simulations. *J. de Physique IV Colloque*, **6**, 187–196.
7. Ryabtsev, I.A., Senchenkov, I.K. (2013) Theory and practice of surfacing operations. Ekotekhnologiya [in Russian].
8. Tsvitanovich, M., Postruzin, Zh., Munk, R. et al. (2011) System of ultrasonic testing of reactor vessel metal of Kudankulam NPP. In: *Proc. of Conf. on Ensuring the Safety of NPP with WWER, Podolsk, Gidropress* [in Russian]. http://www.gid-ropress.podolsk.ru/files/proceedings/mntk2011/documents/mntk2011-184.pdf
9. Margolin, B.Z., Varovin, A.Ya., Kostylyov, V.I. (2005) Determination of residual stresses in the WWER vessels after multi-run welding, surfacing and high-temperature tempering. *The Paton Welding J.*, **10**, 14–20.
10. (1978) TU 108-765–78: *Billets of steel of 15Kh2NMFA and 15Kh2NMFA-A grades for vessels and covers and other assemblies of reactor plants* [in Russian].
11. Kostylev, V.I., Margolin, B.Z. (2000) Determination of residual stress and strain fields caused by cladding and tempering of reactor pressure vessels. *Int. J. of Pressure Vessels and Piping*, **77**, 723–735.
12. (2000) *Procedure for determination of service life of nuclear reactor vessels during operation (MRK-SKhR-2000), RD EO 0353-02*, St.-Petersburg-Moscow [in Russian].
13. Makhnenko, O.V., Kostin, V.A., Zhukov, V.V., Kostenevich, E.S. (2019) Effect of cooling cycle of welding on structure-phase composition of 15Kh2NMFA steel. *The Paton Welding J.*, **9**, 8–17.
14. Hrivnak, I. (1984) *Weldability of steels*. Ed. by E.L. Makarov. Moscow, Mashinostroenie [in Russian].
15. Kasatkin, O.G., Seyffarth, P. (2002) Calculation models for evaluating mechanical properties of HAZ metal in welding low-alloyed steels. In: *Proc. of Int. Conf. on Mathematical Modeling and Information Technologies in Welding and Related Processes.* Kiev, 103–106.
16. Kasatkin, O.G. (1990) Mathematical modeling of relations composition-properties of welded joints and development of calculation and experimental system for optimization of main technological factors for welding of low-alloyed structural steels*: Syn. of Thesis for Dr. of Tech. Sci. Degree.* Kiev, PWI [in Russian].
17. Lobanov, L.M., Kostin, V.A., Makhnenko, O.V. et al. (2020) Forecasting of structural transformations in heat affected zone steel of 15KH2NMFA at anti-corrosion cladding. *Problems of Atomic Science and Technology*, 126(**2**), 89–96.
18. Gurovich, B.A., Kuleshova, E.A., Fedotova S.V. (2011) Influence of chemical composition and structural parameters of steels of WWER reactor vessels on susceptibility to embrittlement caused by formation of grain boundary segregations including the conditions characteristic for long-term operation of power plants. In: *Proc. of 7th Int. Sci.-Techn.Conf. on Ensuring the Safety of NPP with WWER,* Podolsk, Gidropress. http://www.gidropress.podolsk.ru/files/proceedings/mntk2011/autorun/article151-ru.htm
19. Frolov, A.S. (2013) Phase-structural state and service characteristics of new steel compositions for reactor vessels of higher power and service life*: Syn. of Thesis for Cand. of Tech. Sci. Degree*, Moscow, NRC Kurchatov Institute [in Russian].
20. Teplukhina, I.V., Golod, V.M., Tsvetkov, A.S. (2018) CCT diagram plotting based on the numerical analysis of dilatometric tests results. *Letters on Materials*, **8**(1), 37–41.
21. Soloviov, I.V., Kornienko, O.Yu., Zhilyakov, A.Yu., Belorusets, A.M. (2017) Examination of kinetics of overcooled austenite decomposition of 15Kh2NMFA steel during continuous cooling. In: *Proc. of 18th Int. Sci.-Techn. Ural School-Seminar of Metallurgists-Junior Scientists* (Ekaterinburg, 21-23 November 2017), UrFU, 250–252.
22. Makhnenko, V.I. (1976) *Calculation methods of investigation of welding stresses and strains.* Kiev, Naukova Dumka [in Russian].
23. Makhnenko, V.I. (2006) *Safe service life of welded joints and assemblies of modern structures*. Kiev, Naukova Dumka [in Russian].
24. Betton, J. (2008) *Creep Mechanics.* 3-rd ed. Springer, Germany, XVI.

Received 02.11.2020

https://doi.org/10.37434/tpwj2020.12.02

MECHANICAL PROPERTIES OF JOINTS OF 1460 ALUMINIUM ALLOY, PRODUCED BY ELECTRON BEAM WELDING USING FILLER MATERIAL FROM 1201 ALLOY

V.V. Skryabinskyi, V.M. Nesterenkov and **V.R. Strashko**
E.O. Paton Electric Welding Institute of the NAS of Ukraine
11 Kazymyr Malevych Str., 03150, Kyiv, Ukraine. E-mail: office@paton.kiev.ua

The paper presents the results of studying mechanical properties of joints of 1460 alloy and joints of 1460 + 1201 dissimilar alloys, produced by EBW at room and cryogenic temperatures. It is shown that the strength of joints of 1460 alloy, welded using filler material from 1201 alloy at a temperature of 77 K rises by 10 %, and at a temperature of 20 K — by 20 % as compared to the joints welded without using filler material. Mechanical properties of welded joints of 1460 + 1201 dissimilar alloys at the test temperatures of 20, 77 and 293 K are on the level not lower than those of the joints of 1460 alloy, welded with the application of 1201 filler material. Welding technology is described and chemical composition of weld metal is given. 12 Ref., 3 Tables, 9 Figures.

K e y w o r d s : electron beam welding, aluminium-lithium alloys, filler material, mechanical properties, welded joints, cryogenic temperatures

Aluminium alloys of Al–Cu–Li system have higher mechanical properties and a lower specific weight as compared to traditional alloys of Al–Cu system. Russian 1460 and 1469 alloys are designed to replace 1201 alloy in welded structures of aircraft and space engineering operating at normal and cryogenic temperatures [1, 2]. Similarly, 2090 and 2195 alloys, which are produced in the USA, replaced 2219 alloy. The chemical composition of the alloys is presented in Table 1.

American aluminium 2090 and 2195 alloys of Al–Cu–Li system have long been successfully used in aircraft and space engineering [1, 3]. In particular, while replacing 2219 alloy with 2195 alloy in welded structures of fuel tanks of the Space Shattle spaceship, the weight of the product was reduced by approximately 3000 kg. There are examples of successful application of 1460 alloy for the manufacture of mockups of welded structures for cryogenic purposes [1].

The estimates of weldability of 1460 alloy are contradictory. In [4], the data are given that it is satisfactorily welded by both argon arc as well as electron beam welding. The author of [5] considers its weldability unsatisfactory. The main problems that arise during fusion welding are tendency to hot crack formation and insufficiently high mechanical properties of welded joints. The new V-1469 alloy also has reduced characteristics of weldability. In [6] it is noted that during electron beam welding in welds the formation of cracks is possible and the strength of welded joints amounts to 50 % of the strength of the base metal.

To improve the weldability of 1460 and 2090 alloys during fusion welding, filler materials of Al–Cu alloying system are used. For welding of 1460 alloy, the filler wire Sv1201 [7, 8] is used, and for welding of 2090 alloy, the filler 2319 is used [9]. During welding using these filler materials in the weld metal the copper

Table 1. Chemical composition of alloys of Al–Cu and Al–Cu–Li systems for welded structures of cryogenic purpose

Alloy grade	Alloying elements, wt.%							
	Cu	Li	Zr	Ti	Mn	Sc	Mg	Ag
1201 (USSR)	5.8–6.8	–	0.1–0.25	0.02–0.1	0.2–0.4	–	< 0.02	–
2219 (USA)	5.8–6.8	–	0.1–0.25	0.02–0.1	0.2–0.4	–	–	–
1460 (USSR)	2.6–3.3	1.9–2.3	0.1	0.1	0.05–0.1	0.06–0.1	0.06–0.1	–
2090 (USA)	2.4–3.0	1.9–2.6	0.1	0.15	0.05	–	0.25	–
B-1469 (Russia)	3.2–4.5	1.0–1.7	0.02–0.26	0.05–0.07	0.05–0.08	0.02–0.28	0.01–0.5	0.45
2195 (USA)	3.7–4.3	0.8–1.2	0.12	0.1	0.25	–	0.25–0.8	0.25–0.6

V.V. Skryabinskyi — https://orcid.org/0000-0003-4470-3421, V.M. Nesterenkov — https://orcid.org/0000-0002-7973-1986,
V.R. Strashko — https://orcid.org/0000-0001-6852-3551

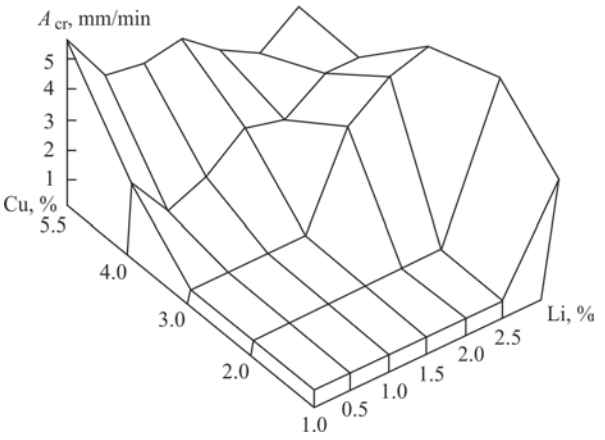

Figure 1. Dependence of weldability A_{cr} of alloys of Al–Cu–Li system on copper and lithium content [10] (with an increase of A_{cr} susceptibility to hot crack formation decreases)

content is increased and the lithium content is reduced. Such a change in chemical composition helps to improve mechanical properties and reduce the susceptibility to hot crack formation in the weld metal.

In [10], the susceptibility of alloys of Al–Cu–Li–0.12Zr system to hot crack formation during welding depending on the content of copper and lithium in them was investigated. It was found that with a decrease in the content of copper <3 % and lithium <1.5 %, the susceptibility to crack formation increases sharply. The results of these studies (Figure 1) should be taken into account during welding of Al–Cu–Li alloys using filler material.

The aim of this work is to show the possibility of improving mechanical properties of Al–Cu–Li system alloys at cryogenic temperatures by changing the chemical composition of the weld metal due to the use of filler material from 1201 alloy on the example of EBW of 1460 alloy.

Welding of all semi-finished products was carried out after a full heat treatment (hardening + artificial aging). Parameters of welding conditions were selected in such a way as to provide a full penetration of a butt in a one pass with the formation of reinforcement and a reverse weld bead. To control the shape of the penetration zone, a system of program distribution of electron beam power density within the spots and heating was used. Mechanical properties of welded joints were investigated at the temperatures of 293, 77 and 20 K. Ultimate tensile strength at room and cryogenic temperatures was determined by tensile testing of standard round specimens (GOST 11150–84, type 1) with a working part diameter of 4 mm. To determine the sensitivity to stress concentrators, round specimens with a notch were tested on tension. The impact toughness was determined on specimens with a Charpy notch throughout the weld metal. All the test specimens were cut out across the weld, placing the weld in the center of the specimen. The hardness of the weld metal and the heat-affected-zone was measured with a Rockwell instrument with a load on a steel ball of 600 N on a B-weighted scale with a ball diameter of 1 mm.

At the first stage, the strength of the base metal and welded joints of Al–4 % Cu–1 % Li alloys and 1460 alloy at temperatures of 20, 77 and 293 K was investigated. Specimens for tests were cut out from the joints welded previously by EBW method while studying weldability of these alloys [11]. The test results are shown in Figures 2 and 3.

From Figure 2 it is seen that the ultimate tensile strength of the base metal of Al–4 % Cu–1 % Li alloy and its welded joints at a decrease in the test temperature from 293 to 20 K rises by 180–190 MPa and reach-

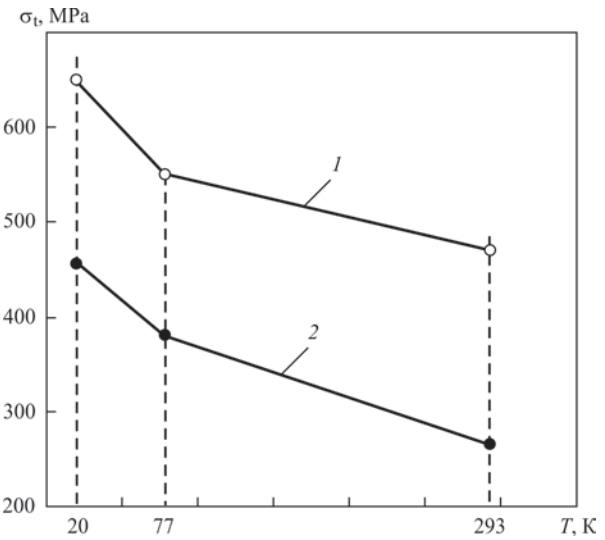

Figure 2. Ultimate tensile strength of specimens made of base metal (*1*) and welded joints (*2*) of plates of Al–4 % Cu–1 % Li alloy with a thickness of 40 mm depending on test temperature

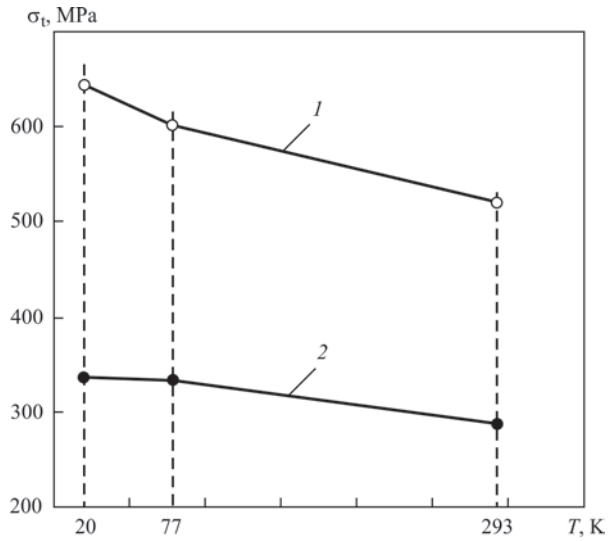

Figure 3. Ultimate tensile strength of specimens made of base metal (*1*) and welded joints (*2*) of rolling rings of 1460 alloy with a thickness of 72 mm depending on test temperature

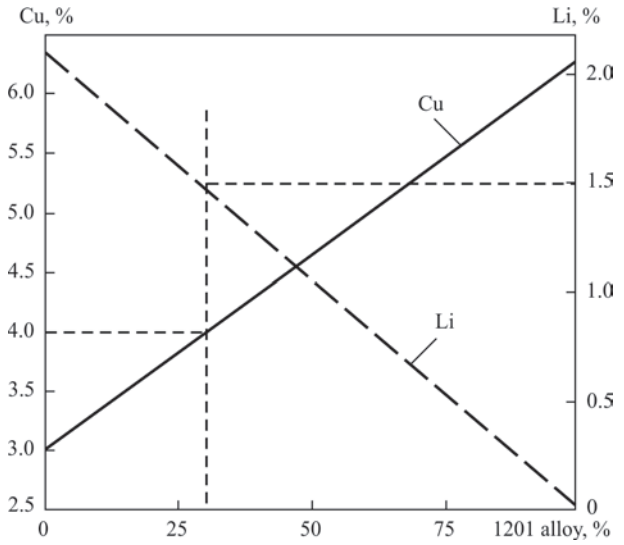

Figure 4. Dependence of calculated copper and lithium content in weld metal of 1460 alloy on the amount of 1201 alloy which participates in the welding pool formation during EBW of 1460 alloy with 1201 filler and during EBW of dissimilar 1460 + 1201 alloys

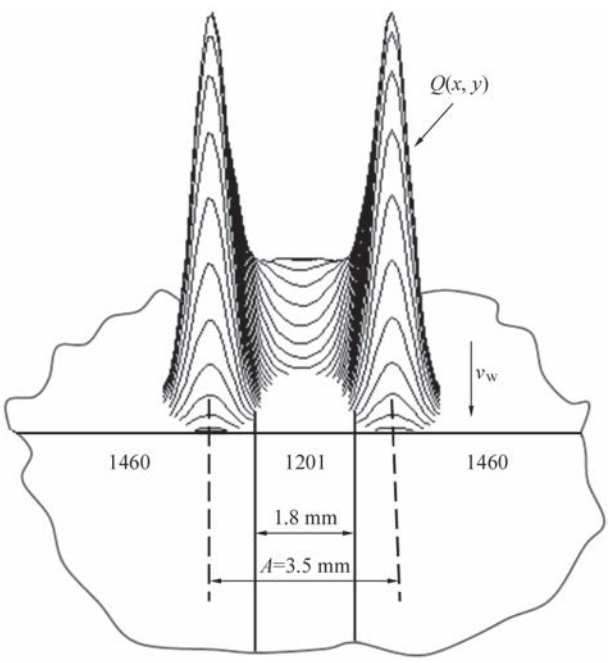

Figure 5. Scheme of EBW of butt joint of plates of 1460 alloy with filler of 1201 alloy ($Q(x, y)$ — distribution of beam density power; V_w — welding direction; A — amplitude of beam scanning)

es 650 and 455 MPa, respectively. The ultimate tensile strength of the base metal of 1460 alloy (see Figure 3) increases from 520 MPa at a temperature of 293 K to 645 MPa at 20 K. In the welded joints of 1460 alloy low-temperature hardening is extremely small. In this regard, during further investigations it was decided to increase the strength of welded joints of 1460 alloy at cryogenic temperatures to reduce the content of lithium and increase the content of copper in the weld metal. It should be noted that during EBW of Al–4 % Cu–1 % Li alloy, the weld metal was proned to microcrack formation [11], which is agreed with the data presented in [10]. Therefore, in order to increase the low-temperature hardening of the joints and at the same time not to provoke the formation of hot cracks in the weld metal, it was decided to increase the content of copper to 4 % and limit the content of lithium to 1.5 %.

The conventional method of changing the composition of weld metal during fusion welding is the use of filler materials. In our case the most suitable filler material from the existing aluminium alloys is 1201 alloy because as compared to 1460 alloy it has an increased content of copper (5.8–6.8 %) and do not have lithium in its composition.

Plates of 1460 alloy with a thickness of 40 mm were welded both with the use of filler material from 1201 alloy, as well as without it. Without a filler, horizontal butts joints were welded using a horizontal beam, and in case of using filler material, welding was performed by a horizontal beam in an uphill mode. The filler material was introduced into the welding pool using a molten insert made of 1201 alloy of 1.8 mm thickness. As was previously determined, the welding pool should contain about 4 % of copper and about 1.5 % of lithium. From Figure 4, it follows that to obtain such a chemical composition in the formation of the weld, about 30 % of the filler from 1201 alloy should be involved.

Taking into account a high elasticity of lithium vapors in vacuum, and as a consequence, its inevitable evaporation losses, it was decided to limit the share of 1201 alloy in the welding pool formation to 25 %. Therefore, with an insert width of 1.8 mm, the width of the weld with parallel side walls should be about 8 mm. EBW conditions are given in Table 2.

In order to exclude preliminary melting and leakage of the insert material from the butt, a beam scanning trajectory in the form of a semicircle while directing the branches of the semicircle in the direction of welding was used. The scanning amplitude was 3.5 mm. The power density of the electron beam was distribut-

Table 2. Conditions of EBW of plates of 1460 alloy and plates of dissimilar 1460+1201 alloys

Material	Thickness, mm	EBW conditions			
		Welding speed, mm/s	Accelerating voltage, kV	Scanning amplitude, mm	Beam current, mA
1460	40	11	60	1.5	320
1460 with 1201 filler	40	5.5	60	3.5	250
1460 + 1201	18	11	30	2.0	350

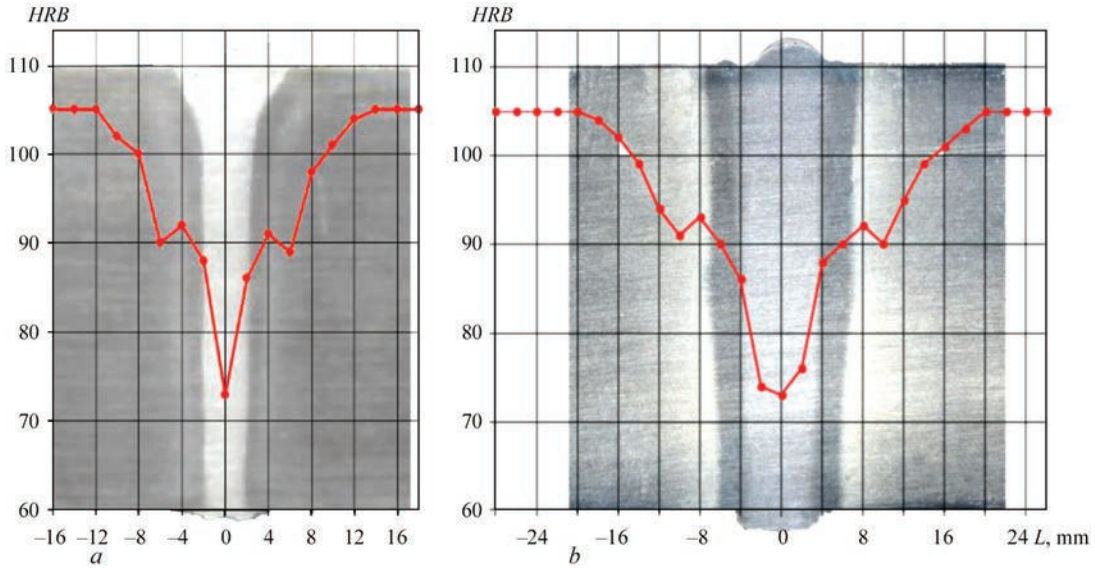

Figure 6. Cross-sections and distribution of hardness in the joints of plates of 1460 alloy of 40 mm thickness welded without filler (*a*) and with filler material of 1201 alloy (*b*)

ed along the scanning trajectory in such a way that the edges to be welded amounted to about 85 % of the total power and about 15 % for the tail part of the pool. The scanning parameters of the electron beam were calculated according to the procedure described in [12]. The welding scheme is shown in Figure 5.

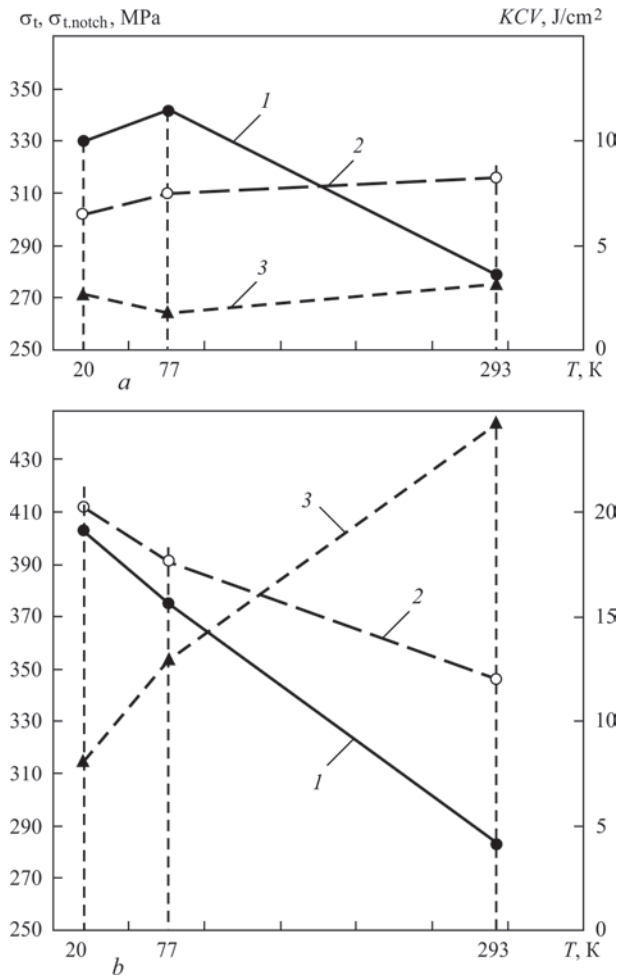

Figure 7. Dependence of mechanical properties of joints of 1460 alloy, welded without filler (*a*) and with filler from 1201 alloy (*b*) on test temperature: *1* — ultimate tensile strength of plane specimens (σ_t); *2* — ultimate tensile strength of specimens with a notch ($\sigma_{t.notch}$); 3 — impact toughness (*KCV*)

Cross-sections of joints and the results of hardness measurements are presented in Figure 6.

The welding process both using filler material as well as without it proceeded steadily without spattering and without leakage of liquid metal. The width of the weld produced without filler material was about 4 mm, and that with a filler was about 8 mm. The welds had almost parallel fusion lines with a slight expansion in the upper part. The hardness of the weld metal was *HRB* 73–76 and did not depend on chemical composition of the weld. The width of the heat-affected-zone (HAZ) for the weld without filler was about 12 mm. The weld produced with the filler of 1201 alloy had a HAZ width of about 20 mm, which is predetermined by the expansion of the molten zone and a lower welding speed. Cracks in the welds and in the HAZ were not detected. The chemical composition of base and filler metal, as well as welds is presented in Table 3.

Mechanical properties of the joints of 1460 alloy at room and cryogenic temperatures of tests are shown in Figure 7.

During welding without filler material, the ultimate tensile strength of the joints rises from 280 to 330 MPa when the test temperature is reduced from 293 to 20 K. The ultimate tensile strength of the specimens with a notch is reduced from 315 to 285 MPa. This indicates an increase in the sensitivity of the weld metal to stress concentrators. The impact toughness of the weld metal is low and is at the level of 2–3 J/cm^2 in the entire range of tests.

Reduction in the content of lithium and increase in the content of copper in the weld metal during weld-

Table 3. Chemical composition of weld metal and base metal during EBW of 1460 alloy using filler material and without it, as well as dissimilar 1460 + 1201 alloys

Location of determination	Chemical composition, wt.%			
	Base	Cu	Li	Sc
1460 alloy	Al	3.0	2.15	0.08
1201 alloy	Al	6.3	–	–
Weld of 1460 alloy, produced without filler	Al	3.0	2.10	0.08
Estimated chemical composition of weld metal during EBW using filler of 1201 alloy	Al	4.0	1.5	0.056
Weld of 1460 alloy, produced using filler of 1201 alloy	Al	3.80	1.45	0.06
Weld of dissimilar 1460 + 1201 alloys	Al	4.05	1.35	0.05

ing using filler made of 1201 alloy allows a significant improvement in mechanical properties of joints at cryogenic temperatures. The strength of joints welded using filler material at a temperature of 77 K, rises by 10 %, and at a temperature of 20 K, it sies by 20 % as compared to the joints welded without filler. Thus, the ultimate tensile strength of the joints at a decrease in the test temperature from 293 to 20 K, rises from 285 to 405 MPa. The specimens without a notch during testing at temperatures of 20 and 77 K fractured along the fusion line. The ultimate tensile strength of the specimens with a notch is everywhere higher than the ultimate tensile strength of plane specimens. When using filler of 1201 alloy, the impacct toughness of the weld metal increases by 3–10 times. It amounts to 25 J/cm^2 at a temperature of 293 K and 7.6 J/cm^2 at 20 K.

Also, experiments on EBW of dissimilar 1460 + 1201 alloys were performed. The welding conditions are given in Table 2. In order to control the degree of participation of alloys to be joined in the formation of the weld, the shift of the electron beam relative to the butt line is usually used. During EBW of butts from 1460 + 1201 alloys, the beam was not shifted relative to the butt, and the distribution of beam power density was controlled along the scanning trajectory in such a way that in the weld formation 75 % of 1460 alloy and 25 % of 1201 alloy took part. At such a ratio, it was expected to obtain about 4 % of copper content and about 1.5 % of lithium content in the weld metal.

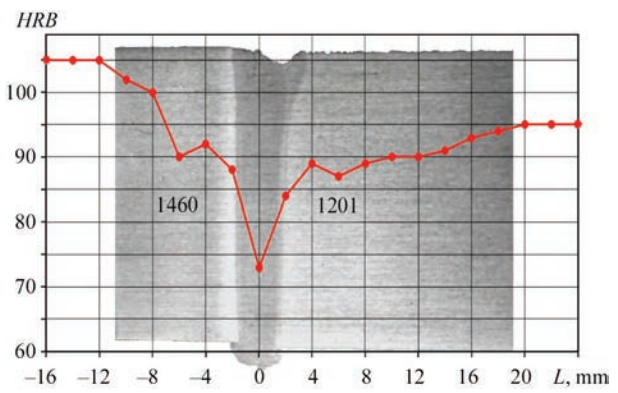

Figure 8. Cross section and hardness distribution in welded joint of plate of 1460 alloy with a thickness of 18 mm with the plate of 1201 alloy

The parameters of the beam scanning were calculated according to the procedure described in the work [12].

Cross-sections of joints, results of hardness measurements and mechanical properties of joints of 1460 + 1201 alloys are shown in Figures 8 and 9.

The hardness of the base metal of 1460 alloy is 105 *HRB* and 95 *HRB* for 1201 alloy at 73 *HRB* of a weld metal hardness. The width of HAZ on the side of 1460 alloy does not exceed 12 mm, and on the side of 1201 alloy it is 20 mm. In the weld metal, individual pores with a diameter of up to 0.5 mm were detected. Lacks of fusion and cracks were not detected. The chemical composition of the weld metal is given in Table 3.

The ultimate stength of 1460 + 1201 joints at a room temperature is at the level of 285 MPa and increases to 445 MPa when the temperature decreases to 20 K. The impact toughness decreases from 26 to 8 J/cm^2. At all test temperatures, the ultimate stength of specimens with a notch is higher than that of plane specimens, i.e. the sensitivity to stress concentrators in the weld metal is negligible.

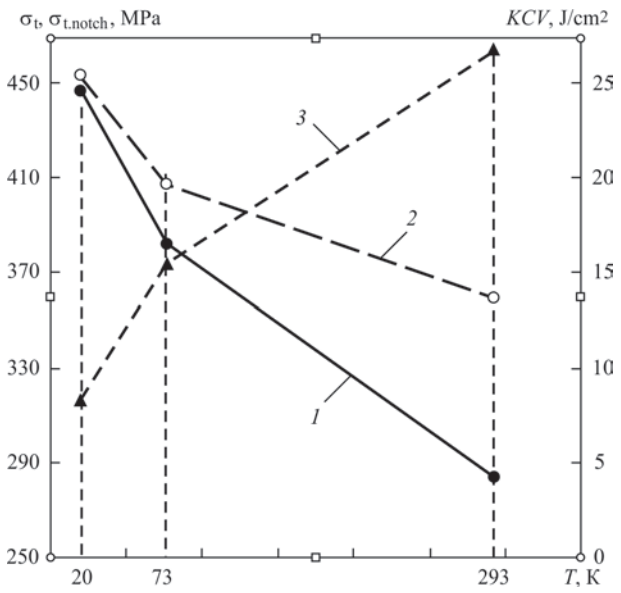

Figure 9. Dependence of mechanical properties of joint of plate of 1460 alloy with plate of 1201 alloy on test temperature: *1* — ultimate tensile strength of plane specimens (σ_t); *2* — ultimate tensile strength of specimens with a notch ($\sigma_{t.notch}$); *3* — impact toughness (*KCV*)

Conclusions

1. Mechanical properties of welded joints of 1460 alloy at room temperature and especially at cryogenic temperatures depend on the content of copper and lithium in the weld metal. As the copper content increases and the lithium content decreases, the ultimate tensile strength of the joints at test temperatures of 20 and 77 K rises by 20 and 10 %, respectively. Such a change in the chemical composition of the weld metal in practice can be carried out by using 1201 alloy as filler material. Impact toughness of the weld metal increases by 3–10 times, and sensitivity to stress concentrators decreases.

2. It is rational to introduce filler material into the welding pool during EBW of 1460 alloy with the use of a molten insert from 1201 alloy. Satisfactory welded joint formation during EBW with an insert is achieved by such a distribution of beam power density, at which about 80 % of the beam power is accounted for welded edges of 1460 alloy and the rest 20 % is accounted on the tail part of the pool.

3. Mechanical properties of welded joints of dissimilar 1460 + 1201 alloys at test temperatures of 20, 77 and 293 K are at a level not lower than the properties of the joints of 1460 alloy, welded using 1201 filler material.

1. Antipov, V.V., Vakhromov, R.O., Oglodkov, M.S. et al. (2016) Welded aluminium-lithium alloys of third generation. Role of fundamental studies in realization of strategic directions of development of materials and technologies of their processing for the period up to 2030. In: *Proc. of 3rd All-Russian Sci.-Techn. Conf. FGUP VIAM,* 2–17 [in Russian]. http://www.spsl.nsc.ru/FullText/konfe/%D0%92%D0%98%D0%90%D0%9C-2016%D1%84%D0%BC%D0%BC.pdf
2. Limarenko, A.L., Sigalo, V.G., Litvishko, T.L. (2002) Properties and structure of high-strength welded aluminium-lithium alloy 1460. *Kosmichna Nauka i Tekhnologiya, Dodatok*, 8(**1**), 123–126 [in Russian].
3. Maslov, G.G., Makarov, G.S. (1991) Aviation metallurgy in 39th International Show of Aerospace Engineering. *Tekhnologiya Lyogkikh Splavov*, **12**, 109–116 [in Russian].
4. Drits, A.M., Krymova, T.V. (1996) Russian high-strength welded aluminium-lithium alloy of 1460 grade. *Tsvetnye Metally*, **3**, 68–73 [in Russian].
5. Kablov, E.N. (2018) *The future of aviation belongs to aluminium-lithium alloys. Redkie Zemli, 2 June 2018* [in Russian]. http://rareearth.ru/ru/pub/20180702/04001.html
6. Makhin, I.D., Nikolaev, V.V., Petrovichev, P.S. (2014) Investigation of weldability of V-1469 and 01570S alloys using electron beam welding for design of advanced manned spaceship. *Kosmicheskaya Tekhnika i Tekhnologii*, 4(**7**), 68–75 [in Russian]. https://www.energia.ru/ktt/archive/2014/04–2014/04–09.pdf
7. Ovchinnikov, V.V., Drits, A.M., Kurbatova, I.A., Gureeva, M.A. (2017) Technology of welding of aluminium wrought alloy 1151. *Naukoyomkie Tekhnologii v Mashinostroenii*, **1**, 10–15 [in Russian]. https://riorpub.com/temp/bb-71c228829aa59ef9893f95ef3f0191.pdf
8. Labur, T.M., Grinyuk, A.A., Poklyatsky, A.G. (2006) Mechanical properties of plasma welded joints on aluminium-lithium alloys. *The Paton Welding J.*, **6**, 32–34.
9. Ramulu, M., Rubbert, M.P. (1990) Gas tungsten arc welding of Al–Cu–Li alloy. *Welding Research Suppl.*, March, 109–114.
10. Fridlyander, I.N., Drits, A.M., Krymova, T.V. (1991) Possibility of development of welded alloys based on Al–Cu–Li system. *Metallovedenie i Termich. Obrab. Metallov*, **9** [in Russian]. https://www.viam.ru/public/files/1991/1991–200808.pdf
11. Bondarev, A.A., Skryabinsky, V.V., Peshcherina, S.V., Butkova, E.I. (1991) Peculiarities of electron beam welding of high-strength alloy of aluminium-copper-lithium system. *Avtomatich. Svarka*, **7**, 37–40 [in Russian].
12. Skryabinskyi, V.V., Nesterenkov, V.M., Rusynyk, M.O. (2020) Electron beam welding with programming of beam power density distribution. *The Paton Welding J.*, **1**, 51–56.

Received 29.11.2020

https://doi.org/10.37434/tpwj2020.12.03

INFLUENCE OF PULSED-ARC WELDING CONDITIONS ON CHANGE OF PARAMETERS OF WELD AND HAZ OF WELDED JOINTS AND MECHANICAL PROPERTIES OF LOW-ALLOY STEELS

A.V. Zavdoveev[1], **V.D. Poznyakov**[1], **S.L. Zhdanov**[1], **M. Rogante**[2] and **T. Baudin**[3]
[1]E.O. Paton Electric Welding Institute of the NAS of Ukraine
11 Kazymyr Malevych Str., 03150, Kyiv, Ukraine. E-mail: office@paton.kiev.ua
[2]Rogante Engineering Office
62012 Civitanova Marche, Italy. E-mail: main@roganteengineering.it
[3]Université Paris-Saclay, CNRS, Institut de Chimie Moléculaire et des Matériaux d'Orsay
91405 Orsay, France. E-mail: thierry.baudin@u-psud.fr

Pulsed-arc welding is characterized by a periodical changing in arc power and, due to its features, it allows solving complex technological problems while creating unique structures, increasing efficiency of welding processes while maintaining a high level of physical and mechanical properties of welded joints. There are many manufacturers of welding equipment, that introduced the idea of using pulsed welding in their production, but data on the impact of pulsed-arc welding on parameters of welds have a different nature. For the successful application of pulsed-arc welding in modern production, it became necessary to study the influence of pulsed-arc welding conditions on the parameters of welds and HAZ as compared to welding using stationary-burning arc, performed using low-alloy welding materials. 20 Ref., 7 Figures.

Keywords: pulsed-arc welding, pulsating arc welding, heat-affected zone, low-alloy welding materials

Pulsed-arc welding is qualitatively different from conventional shielded-gas welding, as well as from manual arc welding at modulated current [1–5]. This process finds ever more application in the manufacture of welded structures from aluminium alloys, titanium and structural steels with the strength of up to 500 MPa [6, 7]. This is explained by the fact that pulsed-arc welding expands the possibilities of controlling the processes of melting and transfer of electrode metal in different spatial positions, improves the formation of welds, reduces the volume of stirring of electrode metal with the base metal and the size of the heat-affected zone [8–16]. This is connected namely with the fact that such well-known companies as Fronius (Austria), Böhler (Germany), ESAB (Sweden), EWM (Germany) and others pay a considerable attention in their activities to the development and manufacture of equipment for realization and expansion of the pulsed-arc welding process in shielding gases. The technical literature covers the influence of PAW parameters on the thermal processes occurring in HAZ metal of welded joints much less, as they affect the structure and mechanical properties of this metal, its resistance to the formation of cold cracks and brittle fracture, etc. In addition, there are differences in the control of pulsed-arc welding modes in different manufacturers. Namely, the uncertainty of these issues hinders the use of pulsed-arc welding in shielding gases in the manufacture of metal structures from the steels that are sensitive to thermal processes and prone to hardening. Therefore, at this stage, the study of the influence of pulsed-arc welding modes using EWM Phoenix Pulse 501 power source on the formation of the weld, thermal welding cycles and mechanical properties of welded joints of low-alloy steels were carried out.

Procedure of experiment. To solve the task set in the work at the first stage, surfacing was performed with a low-alloy welding wire G3Si1 with a diameter of 1.2 mm, which is an analogous to the well-known wire of grade Sv-08G2S. Surfacing was performed on 10 mm thick plates made of 09G2S steel. The sections were made of surfacing plates, on which the parameters of welds and HAZ were measured. The geometric parameters of the welds were determined by digitizing and using special software Axio Vision 4.6. To detect HAZ, the sections were subjected to macroetching with a solution of ferric chloride.

The record of TWC of HAZ overheating area was carried out with the use of chromel-alumel thermocouples of 0.5 mm diameter, while were installed in HAZ region, which were heated to the temperature of 1200 °C.

A.V. Zavdoveev — https://orcid.org/0000-0003-2811-0765, V.D. Poznyakov — https://orcid.org/0000-0001-8581-3526,
S.L. Zhdanov — https://orcid.org/0000-0003-3570-895X, M. Rogante — https://orcid.org/0000-0002-6846-0826,
T. Baudin — https://orcid.org/0000-0002-6765-360X

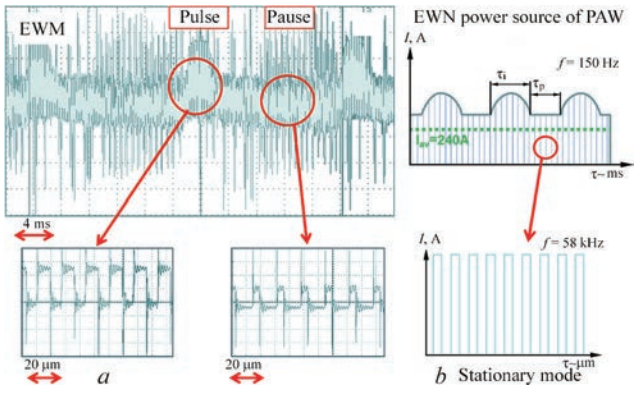

Figure 1. Oscillogram of welding current for pulsed mode: *a* — oscillogram in real time; *b* — schematic image

The key parameters of pulsed-arc welding include: pulse current (I_{pulse}), pause current (I_{pause}), pulse time (t_{pulse}), pause time (t_{pause}). To simplify the characteristics of the pulse process, the following fixed auxiliary parameters were accepted: mean (I_m) and effective welding current (I_{eff}), duty cycle (δ) and frequency (f). To evaluate the influence of pulsed-arc welding modes on the weld parameters, the following conditions were selected: welding current I_m = 120, 140, 160, 180, 200, 220 A, voltage U = 21, 22, 24, 26, 28, 30 V, welding speed 15 m/h, shielding gas is mixture Ag + 18 % CO_2. As a current source, an inverter-type rectifier of the EWM Phoenix Pulse 501 was used, which will provide a different frequency of pulse passage. Such parameters of pulsed-arc welding as duty cycle and pulse frequency for the EWM Phoenix Pulse 501 power source during operation in the pulse mode are programmed by the manufacturer, the user has the ability to control only the value of the mean welding current. Therefore, in the future we manipulate the value of the mean welding current during pulsed-arc welding. It should be noted that with an increase in the mean welding current the frequency f increases from 89 to 153 Hz and the duty cycle δ grows from 0.2 to 0.36.

To determine the welding and technological characteristics (Figure 1) of the current source, a digital oscilloscope UTD2000CEX-II was used, which allows fixing the volt-ampere characteristics within wide ranges. To record the oscillograms, a shunt 75ShSM with a resistance of 150 μOhm was used, which allows recording the welding current of up to 500 A.

Pulsed-arc welding ($f \geq 25$ Hz) and pulsating arc welding ($f \leq 25$ Hz) are distinguished by the frequency of pulses. The optimal pulsation modes were selected using a pulsating arc. In this case, the welding conditions were as follows: welding pulse current I_{pulse} = 140 A, pause current (base current) was 80 % of the pulse current I_{pause} = 112 A; voltage on the arc in the pulse U_{pulse} = 22 V, voltage on the arc in the pause U_{pause} = 18 V, welding speed v_w = 15 m/h, moreover, the pulse time t_{pulse} and pause time t_{pause}, as well as current in the pause were varied.

At the second stage, to evaluate the effect of pulsed-arc welding on the mechanical properties of welded joints of low-carbon steels S460M and 14Kh2GMR the specimens were welded to. Mechanized welding in shielding gases (Ag + 18 % CO_2) from joints of steel S460M and 14Kh2GMR of 16 mm thickness with a V-shaped edge preparation using the wire of a solid section G3Sil and Sv-10KhN2GSMFTYuA with a diameter of 1.2 mm, respectively. The root passes during welding of these steels were produced on a copper substrate. Welding using the conventional process (by arc that burns stationary) was performed on the following conditions: I_w = 180–200 A, U_a = 26 V, v_w = 15–18 m/h. The conditions of automated pulsed-arc welding were as follows: I_m = 220–240 A, U_a = = 26–28 V, v_w = 14–21 m/h.

In order to conduct mechanical tests and determine the impact toughness of HAZ metal, standard specimens were prepared. For the static (short-term) tensile tests, the specimens of type II were mechanically manufactured of steel in accordance with GOST 6996–96 (3 specimens for each cooling rate). The tests were performed according to GOST 6996–66 at a temperature of 20 °C. The impact toughness was determined during tests of Charpy specimens with a sharp notch (GOST 9454–78) at the test temperatures of –40 °C. The resistance to cold crack formation was determined using technological Tekken specimens.

Obtained results and their discussion. *Pulsed-arc welding.* When comparing the stationary and pulsed-arc welding modes, it is clearly seen that in pulsed-arc welding the weld bead is more homogeneous and uniform without traces of spattering. The measurements of metal losses on spattering showed that in pulsed-arc welding they decrease by an order of value, from 0.7 % during the stationary process to 0.07 % during pulsed-arc welding.

Analysis of the cross-section of the deposits (Figure 2) performed under different conditions showed that the penetration depth during pulsed-arc welding increases as compared to the stationary welding process on the same conditions. Thus the shape of weld penetration in pulsed-arc welding considerably differs from the process which was performed by a stationary-burning arc.

The quantitative analysis showed that with an increase in welding current, the width of the weld also increases. The nature of the change in this value is the same for welding using a stationary-burning arc, as well as for pulsed-arc welding. The similar regularity is observed for the height of the weld. As for the penetration depth, in general, with an increase in welding current, it increases, but in the case of pulsed-arc welding, the penetration depth is almost twice higher than in the case of stationary arc welding (Figure 3). Also in pulsed-arc welding, the cross-sectional area of the weld exceeds these indices for welding using a stationary-burning arc. The value of HAZ under the mushroom-shaped section is comparable for both

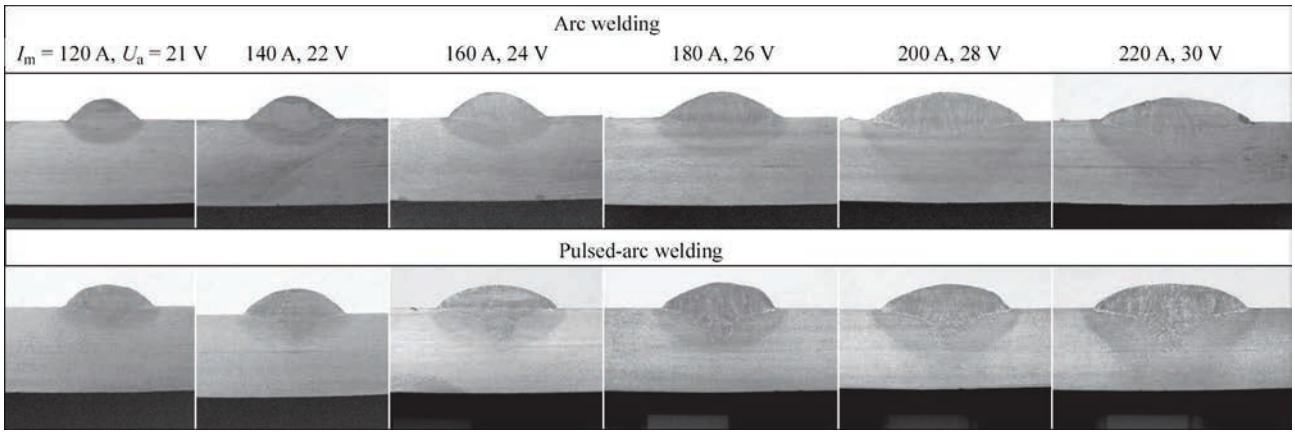

Figure 2. Appearance of macrosections

types of welding, and in the weld root of the HAZ during pulsed-arc welding it is lower (Figure 3).

Pulsating arc. According to the experiment data, it was found that with an increase in the pause current, the width of the weld increases, here to smaller values of the duty cycle larger values of the weld width correspond (Figure 4). The height of the weld increases uniformly with an increase in the pause current. The change in the penetration depth has similar regularities, i.e. it increases with an increase in the pause current. The change in HAZ parameters under the mushroom-shaped section has a monotonous nature. The lower duty cycle corresponds to large values of HAZ width. It is important to note that the average HAZ values under the mushroom-shaped section are lower than during welding using a stationary-burning arc and pulsed-arc welding. The similar regularities are observed for HAZ both in the weld root (Figure 4, *b*) as well as in the surface of the weld.

At the welding conditions at a pulse current I_{pulse} = = 140 A and the pause current I_{pause} = 112 A (fixed pulse time is 0.5 s) with an increase in the pause time, i.e. with a decrease in the frequency f and duty cycle δ, the weld height increases, the weld width decreases slightly and the width of HAZ decreases, and the penetration depth at t_{pause} = 0.5 increases, and then almost does not change. In the case of fixing the pause time (0.5 s) and increasing the pulse time, i.e. with an increase in frequency f and duty cycle δ, the penetration depth also initially increases, and then stabilizes, but to confirm this fact the further investigations are required. The width of the HAZ varies in a nonlinear form, but in the case of a fixed pulse time it is lower than in the case of stationary-burning arc welding. In the case of fixing the pause time and increasing the pulse time, the width of

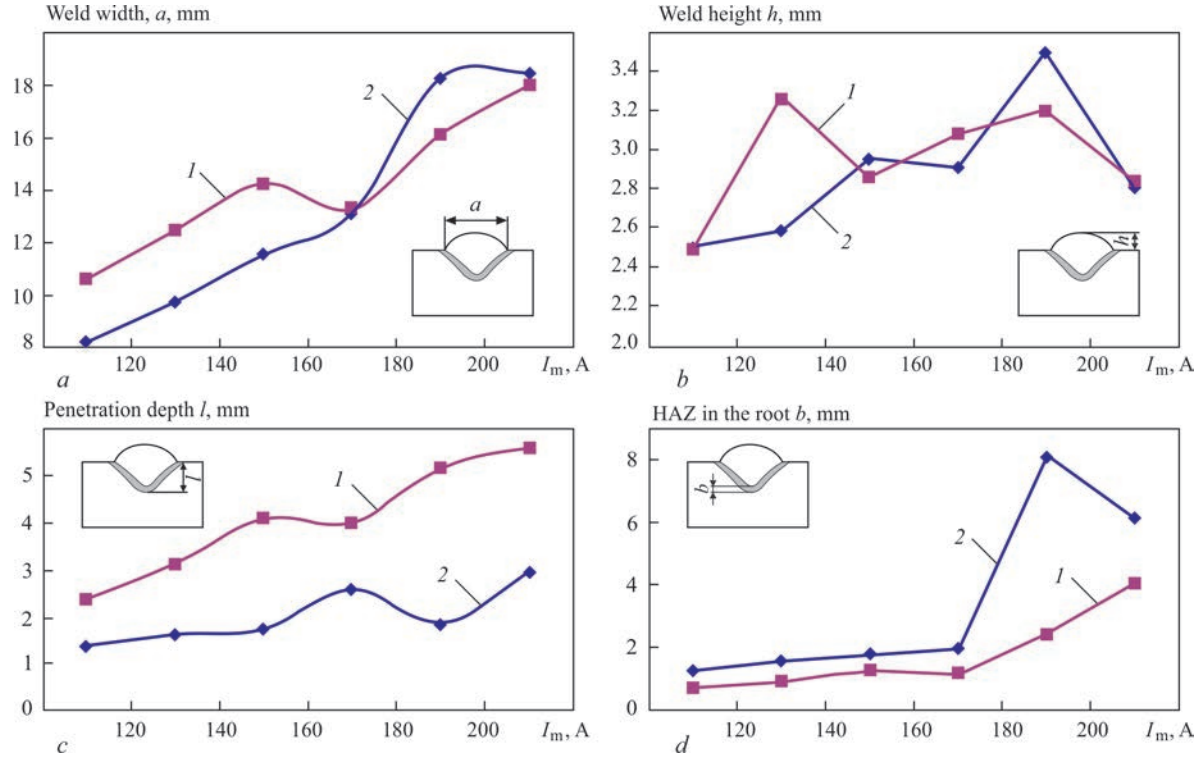

Figure 3. Quantitative characteristics of parameters of welds produced by pulsed-arc and arc welding: *1* — pulsed-arc; *2* — arc

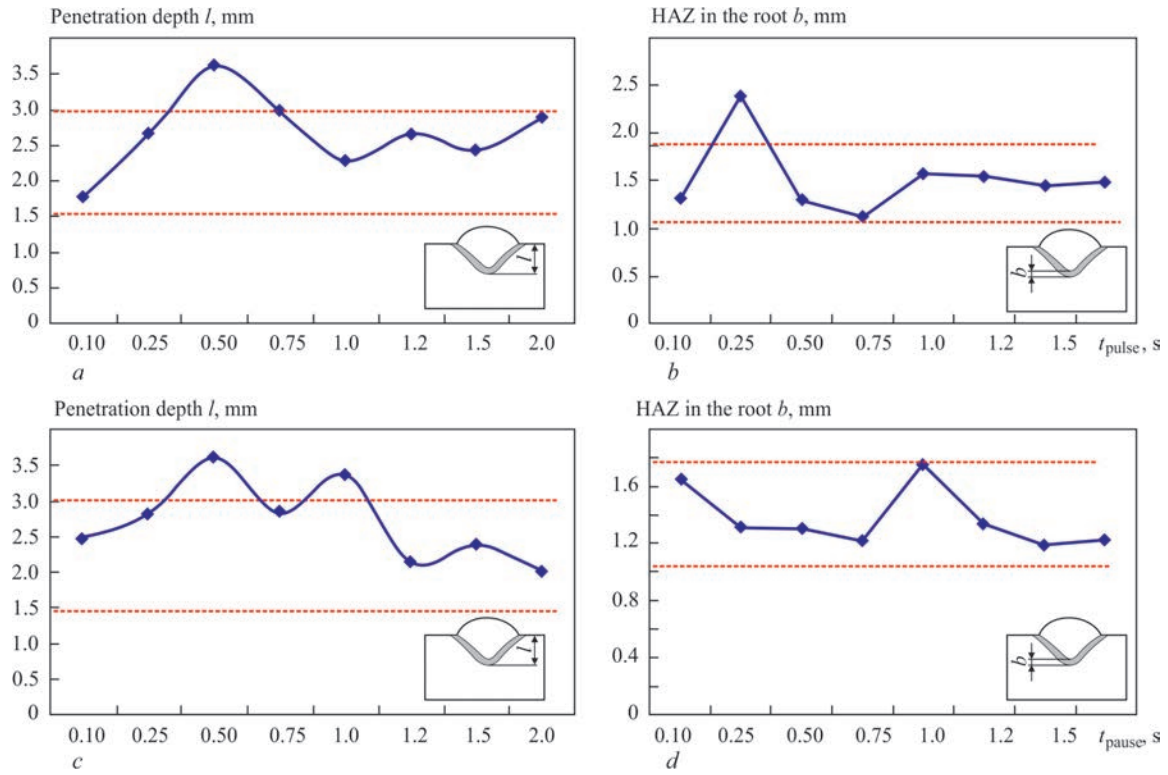

Figure 4. Quantitative characteristics of parameters of welds produced by pulsating arc welding: *a*, *b* — pulse time is fixed t_{pulse} = 0.5 s; *c*, *d* — pause time is fixed t_{pause} = 0.5 s

the HAZ is larger than for pulsed-arc welding and lower than for the welding using a stationary-burning arc.

The analysis of thermal cycles of welding allowed establishing the following features: in pulsed-arc welding the rate of growing temperature of metal of an area of HAZ overheating is higher than in the case of welding by a stationary arc; in the high-temperature range from 1350 to 1000 °C, the cooling of the metal during pulsed-arc welding is faster, and in the temperature range lower than 1000 °C, it is slower (Figure 5). A more detailed analysis of the influence of pulsed welding modes on the cooling rate of HAZ metal is shown in Figure 6. From the given data it is seen that the cooling rate of the metal in the temperature range of the lowest resistance of austenite of 600–500 °C for pulsed-arc welding is 1.5 times lower than in the case of stationary arc welding, and the time of cooling metal in the temperature range of 800–100 °C $\tau_{8/1}$ has the similar values. Peculiarities of running TWC during pulsed-arc welding, revealed from the diagram of the derivative (Figure 5), confirmed that the cooling rate of the metal in the areas of HAZ, which are heated to the temperatures higher than 1000 °C is higher than during welding with the arc, which burns stationary. In HAZ, where the metal is heated to the temperatures lower than 1000 °C, the cooling rate of the metal is lower than during welding using a stationary-burning arc. This contributes to the diffusion processes during structural transformations and, as a consequence, the formation of a mixed bainitic-martensitic structure.

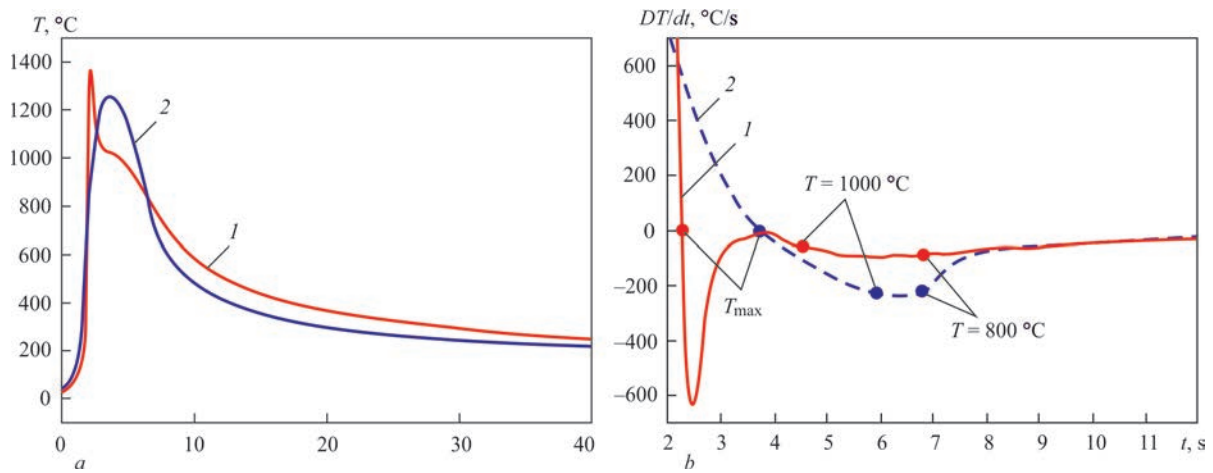

Figure 5. Thermal welding cycles (*a*) and rate of temperature change (*b*) for pulsed-arc welding (*1*) and arc welding (*2*)

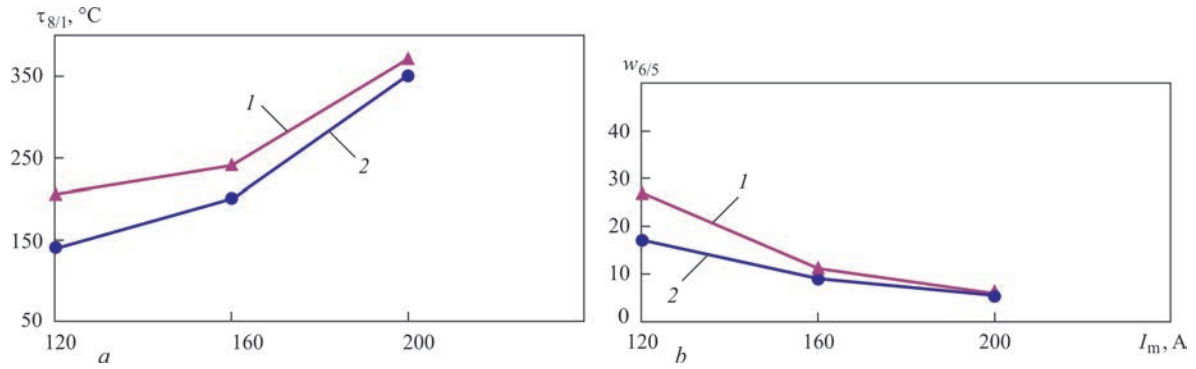

Figure 6. Change of time (*a*) and rate (*b*) of cooling of area of overheat of HAZ metal in pulsed-arc welding (*2*) and welding using stationary arc (*l*) at a rate of 15 m/h

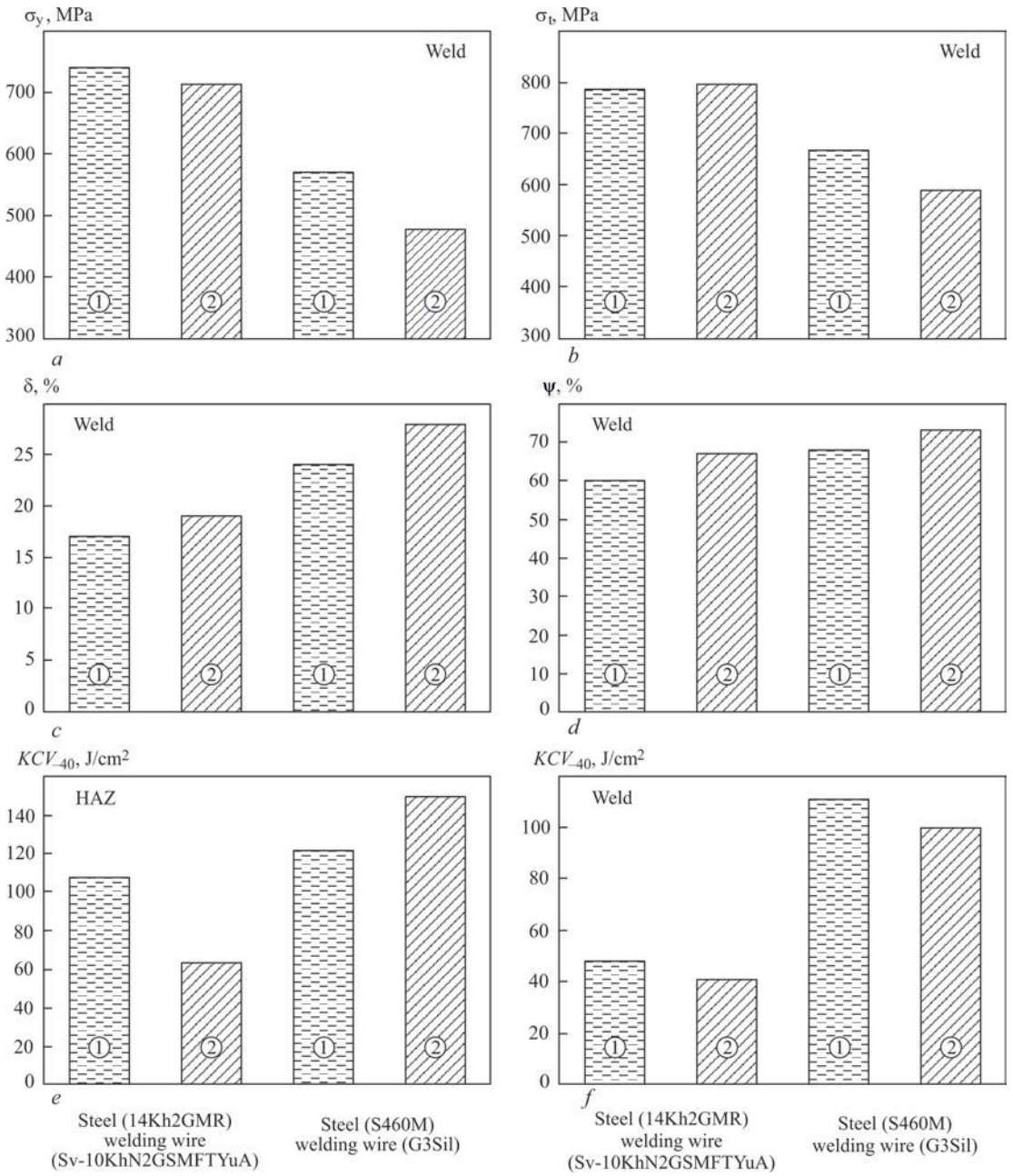

Figure 7. Mechanical properties of welded joints of low-carbon high-strength steels 14Kh2GMR and S460M during pulsed-arc welding (*1*) and arc welding (*2*)

The change in cooling conditions observed during the transition from stationary-burning arc welding to the pulsed-arc welding suggests that in this process of welding in the HAZ metal of high-strength steels with $\sigma_{0.2} > 600$ MPa will form a more favorable structure with a high stability to cold crack formation and to brittle fracture. The work in this direction will be the result of our further investigations.

The mechanical properties of welded joints are shown in Figure 7. Studies of the effect of pulsed-arc welding on the mechanical properties of welded joints of low-carbon high-strength steels of grades S460M and 14Kh2GMR showed that pulsed-arc welding allows obtaining higher values of static strength of the weld metal while maintaining a high level of ductility. Moreover, the values of impact toughness KCV_{-40} at the test temperature of –40 °C for both weld metal as well as HAZ metal exceed the values obtained by welding using a stationary-burning arc. Thus, under the conditions of pulsed-arc welding the best values of operational characteristics are reached, and the values of impact energy exceed the requirements of EN 10025-2 $KCV_{-20} \geq 27$ J.

The results of tests of welded joints, which were produced using Tekken technological specimens, testify to a sufficiently high resistance to the formation of cold cracks of S460M steel both in pulsed-arc welding and in arc welding without heating. For stronger steels, such as 14Kh2GMR, it is possible to increase the resistance of welded joints to a delayed fracture in both pulsed-arc welding and stationary arc welding, possibly due to a preheating to the temperatures of 90–100 °C.

Conclusions

Comprehensive investigations of the influence of pulsed-arc welding modes using the EWM Phoenix Pulse 501 power source on the formation of the weld, thermal welding cycles and mechanical properties of welded joints of low-alloy steels established that:

- pulsed-arc welding in the specified ranges of frequencies and duty cycle allows reducing the amount of metal spattering, the width of the heat-affected zone, increasing the penetration depth (almost 2 times) as compared to stationary-burning arc welding. The cooling rate of the HAZ metal in the temperature range of 600–500 °C is reduced by almost 1.5 times;
- use of pulsating arc welding allows expanding the possibilities of controlling the weld formation and increasing the width of the weld and reducing the width of the HAZ as compared to welding using a stationary-burning arc;
- it is shown that the metal of welds and HAZ of welded joints of steels S460M and 14Kh2GMR produced by pulsed-arc welding, have a sufficient resistance to cold crack formation and a higher static strength while maintaining a high level of ductility of the weld metal.

1. Poznyakov, A.A., Zavdoveev, A.V., Gajvoronsky, A.A., Denisenko A.M. (2018) Effect of pulsed-arc welding modes on the change of weld metal and haz parameters of welded joints produced with Sv-08kh20N9G7T wire. *The Paton Welding J.*, **9**, 7–12.
2. Palani, P.K., Murugan, N. (2006) Selection of parameters of pulsed current gas metal arc welding. *J. of Materials Processing Technology*, **172**, 1–10.
3. Tong, H., Ueyama, T. et al. (2001) Quality and productivity improvement in aluminium alloy thin sheet welding using alternating current pulsed metal inert gas welding system. *Sci. Technol. Weld. Join.*, 6(**4**), 203–208.
4. Needham, J.C., Carter, A.W. (1965) Material transfer characteristics with pulsed current. *Brit. Welding. J.*, **5**, 229–241.
5. Rajasekaran, S. (1999) Weld bead characteristics in pulsed GMA welding of Al–Mg alloys. *Welding. J.*, 78(**12**), 397–407.
6. Zavdoveev, A., Rogante, M., Poznyakov, V. et al. (2020) Development of the PC-GMAW welding technology for TMCP steel in accordance with welding thermal cycle, welding technique, structure and properties of welded joints. *Reports in Mechanical Engineering*, 1(**1**), 26–33.
7. Zavdoveev, A., Poznyakov, V., Kim, H.S. et al. (2020) PC-GMAW effect on the welding thermal cycle and weld metal geometry for high strength steels. *International J. of Engineering and Safety Sciences*, **1**, 5–16.
8. Murray, P.E. (2002) Selecting parameters for GMAW using dimensional analysis. *Welding J.*, 81(**7**), 125–131.
9. Amin, M., Ahmed N. (1987) Synergic control in MIG welding 2-power current controllers for steady dc open arc operation. *Metal Construction*, June, 331–340.
10. Amin, M. (1983) Pulse current parameters for arc stability and controlled metal transfer in arc welding. *Ibid.*, May, 272–377.
11. Lambert, J.A. (1989) Assessment of the pulsed GMA technique for tube attachment welding. *Welding J.*, 68(**2**), 35–43.
12. Essers, W.G. Van Gompal (1984) Arc control with pulsed GMA welding. *Ibid.*, 64(**6**), 26–32.
13. Amin, M. (1981) Synergetic pulse MIG welding. *Metal Construction*, **6**, 349–353.
14. Dorn, L., Devakumaran, K., Hofmann, F. (2009) Pulsed current gas metal arc welding under different shielding and pulse parameters. Pt 2: Behaviour of metal transfer. *ISIJ Int.*, 49(**2**), 261–269.
15. Paton, B.E., Potapievsky, A.G, Podola, N.V. (1964) Consumable electrode pulsed-arc welding with programmed adjustment of process. *Avtomatich. Svarka*, **1**, 2–6 [in Russian].
16. Ueyama T. (2013) Trends in developments in gas shielded-arc welding equipment in Japan. *The Paton Welding J.*, **10**, 53–60.
17. Lashchenko, G.I. (2006) *Methods of consumable electrode arc welding of steel*. Kiev, Ekotekhnologiya [in Russian].
18. Zhuo, Y., Yang, C., Fan, C. et al. (2020) Grain refinement of wire arc additive manufactured titanium alloy by the combined method of boron addition and low frequency pulse arc. *Materials Sci. and Eng*: A, 140557. doi:10.1016/j.msea.2020.140557.
19. Saraev, Y.N., Solodskiy, S.A., Ulyanova, O.V. (2016) Improving processes of mechanized pulsed arc welding of low-frequency range variation of mode parameters, IOP *Conf. Ser. Mater. Sci. Eng*. 127, 12019. https://doi.org/10.1088/1757-899x/127/1/012019.
20. Chen, C., Fan, C., Cai, X. et al. (2019) Arc characteristics and weld appearance in pulsed ultrasonic assisted GTAW process. *Results Phys.*, **15**, 102692. https://doi.org/https://doi.org/10.1016/j.rinp.2019.102692.

Received 29.10.2020

https://doi.org/10.37434/tpwj2020.12.04

DEVELOPMENT OF REMOTELY-CONTROLLED EQUIPMENT AND TECHNOLOGY FOR LASER WELDING REPAIR AND RESTORATION OF PERFORMANCE OF NPP STEAM GENERATORS

V.D. Shelyagin, A.V. Bernadskyi, O.V. Siora, V.A. Kurylo and **O.M. Suchek**
E.O. Paton Electric Welding Institute of the NAS of Ukraine
11 Kazymyr Malevych Str., 03150, Kyiv, Ukraine. E-mail: office@paton.kiev.ua

Control straight butt joints of 10Kh18N10T and 10Kh17N13M3T steel blanks were welded in the vertical position with incomplete penetration by the thickness. Visual and radiographic examination, and metallographic investigations were performed, and welded joint microhardness was determined. Parameters of technological welding modes of the studied circumferential welded joints were established. Conditions of compliance with quality category «high B» of DSTU EN ISO 13919–1:2015 standard were the criterion for selection of appropriate parameters of the modes of laser welding of circumferential butt joints. As a result of work performance, it is shown that the point of welding start influences the dimensions of the weld section, in which the welding process is stabilized, and specified penetration depth is achieved. The techniques developed by the authors were verified on simulator-samples during pilot testing of the model of remotely-controlled equipment developed for repair and restoration of performance of PGV-1000M type steam generators. 18 Ref., 2 Tables, 9 Figures.

Keywords: repair of NPP steam generator, heat-exchanger tubes, laser welding, technology, equipment

Heat exchangers are designed for exchange of thermal energy between two or several environments and they widely applied in power generation, food, chemical and other industries. Combined assemblies from dissimilar metals are quite often used in the structures of heat exchangers to enhance their performance that allows more fully realizing the advantages of each of them. This also raises a difficult issue of fabrication and repair of such structures, as, when it is necessary to apply welding technologies, the problem of welding dissimilar metals has to be solved. Its solution is more complicated, compared to similar material welding [1–3]. An example of the need to perform such welding is installing plugs for sealing heat exchanger tubes in collectors of steam generators of PGV-1000M type for their repair.

In Ukraine 15 nuclear power units are in service in the four operating nuclear power plants (NPP), of which 13 are of WWER-1000 type and two are of WWER-440 type, of the total installed capacity of 13835 MW [4]. Steam generator of horizontal PGV-1000M type (further on referred to as SG) is a component of NPP circulation loop with water-water energy reactor WWER-1000 and it is designed for producing saturated steam as part of NPP power unit [5]. At present 52 horizontal SG operate in Ukraine, the operating time of which is from 10 to 130 thou h [6]. SG body in its middle part is welded to two vertical collectors of the first circuit designed for connection with 11000 heat exchange tubes (HET) bent into U-shaped coils [5]. The tube bundle with spacing and fastening elements takes up about 78 % of the area of the cross-sectional part of steam generator body. HET in bundles are placed in staggered order with steps of 19 mm by height and 23 mm by width between the axes [7], and minimum distance between HET outer walls is equal to 6 mm (Figure 1). The body of steam generator collector is made from 10GN2MFA steel. The internal surface of the collectors is clad by an anticorrosion austenitic deposit (1st layer is ZIO-8; 2nd layer is EA 898/21B), the thickness of each layer is about 3 mm.

The coil ends on SG made before 1990 were inserted into collector holes with further expansion to the entire inserted depth by the explosion technique [7]. The ends of coils in SG manufactured starting from 1990 were expanded after insertion into the collector holes by the method of hydraulic expansion and mechanical final expansion of the outlet section. In both the cases, the coil end faces were argon-arc welded to anticorrosion deposit.

During SG operation different cases of their failure were detected [5–8]. One of the most important con-

V.D. Shelyagin — https://orcid.org/0000-0001-8153-6533, A.V. Bernadskyi — https://orcid.org/0000-0002-8050-5580,
O.V. Siora — https://orcid.org/0000-0003-1927-790X, V.A. Kurylo — https://orcid.org/0000-0003-0790-9404,
O.M. Suchek — https://orcid.org/0000-0002-8961-3887

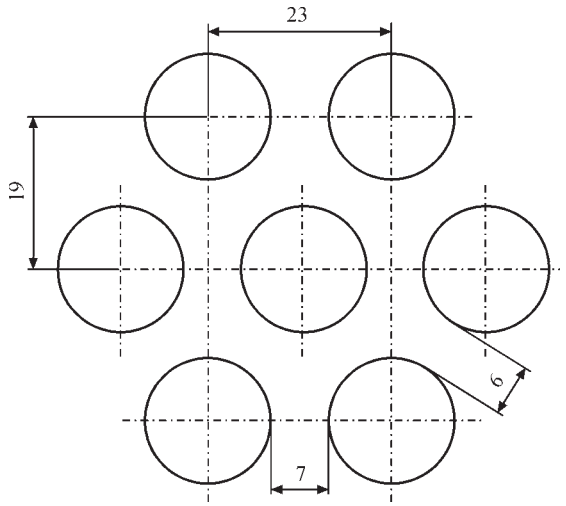

Figure 1. Scheme of heat exchanger tube layout is SG

ditions of safe operation of power units with WWER type reactors is absence of the coolant flowing from the first to the second circuit [8]. Heat exchanger tubes transfer the heat from the coolant of the first circuit to the second one, and act as protection barrier between them. HET damage can lead to penetration of radioactive first circuit coolant into the second circuit that compromises the safety of nuclear power units.

SG HET damage mechanisms are described in detail in the IAEA document [9]. It is shown that the main cause of HET damage is general corrosion, pitting, stress corrosion cracking and a combination of pitting and corrosion cracking. In most cases, degradation starts from point corrosion. After some time, at simultaneous increase of stresses which stretch the tubes in the radial direction, corrosion cracking starts additionally affecting this part of the tube. It is exactly initiation and intensive growth of cracking defects under normal operation conditions that may lead

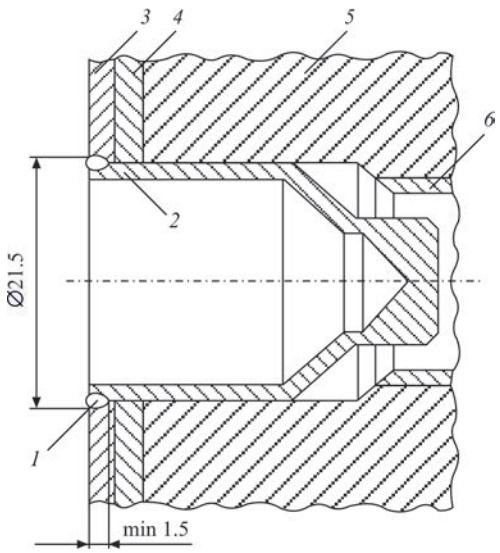

Figure 2. Scheme of plug welding in: *1* — weld; *2* — plug; *3* — first deposited layer; *4* — second deposited layer; *5* — SG wall; *6* — HET

Figure 3. Plug installed using argon-arc welding [18]

to flows from the first into the second circuit. When such a situation arises, the reactor unit is shutdown for unscheduled repair. Defective HET are sealed by placing a plug (Figure 2), which is welded around by argon-arc process. Increase of the number of plugged HET can lead both to considerable financial losses, and to lowering of operating efficiency of the units, because of reduction of heat exchange surface. In keeping with the repair scheme (see Figure 2), the circumferential butt welded joint of the plug with the SG collector body should be made in the vertical position with incomplete penetration (maximum penetration depth of 1.5 mm) and localized fusion zone.

Argon-arc welding [10–12] which is now used at repair, is characterized by higher heat input into the parts being welded and insufficient concentration of the heat source, compared to laser welding [13–17]. Weld form factor K_f (ratio of weld width to penetration depth) is equal to 2–4 in argon-arc welding. If the condition of ensuring minimum penetration depth of not less than 1.5 mm is satisfied, it leads to increase of the diameter of the circumferential welded joint with the plug (Figure 3) [18]. It results in overheating of the parts and negative impact on the adjacent joints, associated with increase of residual stresses. The area of influence approximately coincides with the zone of temper colours (see Figure 3). All this limits the possibilities of application of argon-arc welding for repair of SG of PGV-1000M type.

The urgency of the work consists in the potential for replacement of argon-arc welding technology. The new technology should provide the required penetration depth at reduction of welded joint diameter. It can be achieved at application of local heat sources, such as the laser or electron beam. The authors' idea consists in application of laser welding technology for SG repair. It is exactly the laser beam as a highly-concentrated energy source that can provide an extremely small thermal impact on the structure and longer operating life of welded joints.

Table 1. Chemical composition of welded steels, wt.%

Steel	C	Si	Mn	Ni	S	P	Cr	Ti	Fe
10Kh18N10T	< 0.1	< 0.8	1–2	10–11	< 0.2	< 0.035	17–19	< 0.6	Balance
10Kh17N13M3T	< 0.1	< 0.8	< 2	12–14	< 0.2	< 0.035	16–18	< 0.7	Same

The objective of the work was development of remotely-controlled automatic equipment and verification of laser welding technology for repair and restoration of performance of steam generators of PGV-1000M type.

Materials and experimental procedures. Used as experimental materials (Table 1) were stainless austenitic steels 10Kh18N10T (from which plugs are made) and 10Kh17N13MT (close in its composition to the first deposited layer in SG).

In order to determine the technological features of laser welding of joints of dissimilar stainless austenitic steels in the vertical position, the work was performed by the procedure described below.

1. Control straight butt joints with weld form factor K_f < 1 with incomplete penetration by the thickness were welded in the vertical position on machined 300×100 mm blanks from 3 mm sheets of 10Kh18N10T (ultimate strength σ_t = 520–550 MPa) and 10Kh17N13M3T (ultimate strength σ_t = 510–540 MPa) steels.

2. For each of the produced butt welded joints of dissimilar steels visual and radiographic inspection were performed, and their microhardness was determined.

3. Analysis of investigation results was the base for establishing the parameters of the technological modes of welding the circumferential joints of dissimilar steels.

4. Samples of plate-tube type (Figure 4) were prepared from blanks of 10Kh17N13M3T sheet steel (3 mm thick) of 100×100 mm size with 20 mm hole, which were joined by a circumferential weld to 100 mm long tube billets from 10Kh18N10T steel (with outer tube diameter of 20 mm and 1.5 mm wall thickness) at a horizontal position of the tube. Variation of the technological mode parameters resulted in circumferential butt welded joints with incomplete penetration between the tube and sheet with weld form factor K_f < 1.

5. Each of the produced circumferential welded joints of plate-tube type was tested according to in item 2.

6. Analysis of investigation results allowed determination of the most rational technological parameters of welding the circumferential joints of dissimilar steels for welding in plugs into steam generator heat exchanger tubes.

7. The developed model of a laboratory stand for laser welding in of plugs was used to conduct pilot testing of the created remotely-controlled equipment on simulator-samples.

Work on determination of the technological features of producing circumferential welded joints of stainless steels in the vertical position was performed in the laboratory stand, using Nd: YAG-laser DY044 of ROFIN-SINAR Company, Germany, with radiation wave length of 1.06 μm.

Experimental results. Parameters of technological modes for laser welding of a control straight butt joint of sheet samples, made in the vertical position, were varied in the following ranges: welding speed of 17–100 mm/s; defocusing value of –1–+7 mm; laser radiation power of 1.65–4.4 kW. A lens with 300 mm focal distance and argon as shielding gas with the flow rate of 333 cm^3/s were used in the investigations.

In order to obtain control straight butt joints of sheet samples, quality assessment criteria were used, which meet the requirements of DSTU EN ISO 13919-1:2015 standard «Welding. Electron and laser beam welded joints. Guidance on quality levels for imperfections. Part 1. Steel».

It is found that the characteristic defects which form at laser welding of control straight butt joints of sheet samples from stainless steels in the vertical position can be undercuts, lacks-of-fusion, shrinkage and crater cavities, excess convexity, isolated pores or voids or their sequences.

Results of analysis of the data of metallographic investigations, visual and radiographic inspection of control butt joints of sheet samples were used to select the ranges of parameters of the technological modes of laser welding, which allowed producing butt weld-

Figure 4. Plate-tube type joint after laser welding

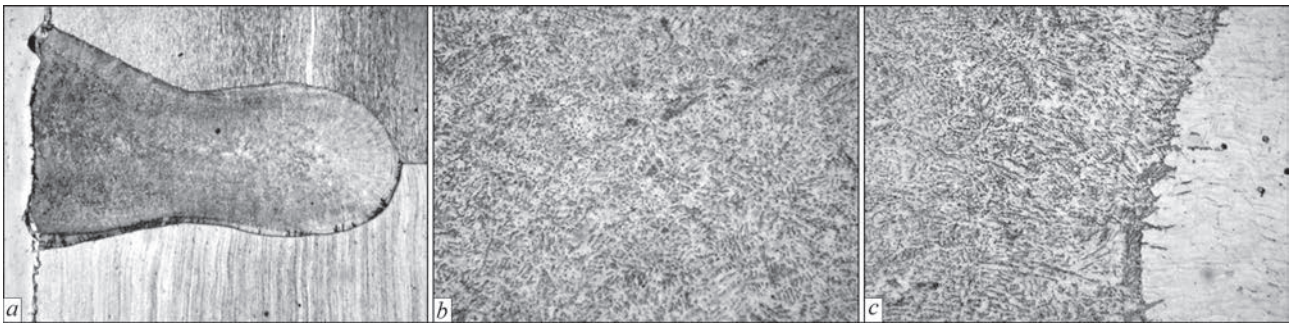

Figure 5. Structure of the produced welded joint of 10Kh18N10T and 10Kh17N13M3T steels: *a* — macrostructure (×50); *b* — metal structure in the weld central part (×400); *c* — metal structure on the fusion line (×400)

ed joints of quality category not lower than «C», acc. to DSTU EN ISO 13919-1:2015.

These modes were used to make in the vertical position the circumferential butt welded joints with weld form factor $K_f < 1$ and incomplete penetration.

During mechanical testing for static uniaxial tension the values of ultimate strength σ_t = 460–475 MPa were obtained at static tension of circumferential butt welded joints of plate-tube type on 10Kh18N10T (tube) and 10Kh17N13M3T (plate) steels. Comparison of the data shows that the breaking force for circumferential butt welded joints of plate-tube type of 10Kh18N10T (tube) and 10Kh17N13M3T (plate) steels is not less than 80 % of the breaking force of the tube base material (10Kh18N10T steel).

Figure 5 shows the photo of a structure characteristic for circumferential butt welded joints of plate-tube type of 10Kh18N10T and 10Kh17N13M3T steels (each 3 mm thick) welded with incomplete penetration in the vertical position with weld form factor $K_f < 1$.

The structure of weld metal of the joint shown in Figure 5, *a* is dispersed cast one, and it is divided into two zones. In the weld central part the structure is cellular-dendritic by the total height. In the weld middle part closer to the fusion line a zone of thin columnar crystallites is observed, which grow in the direction of heat removal. The zones are divided by a line of finer crystallites. The microstructure in the weld central part (Figure 5, *b*) consists of an austenitic matrix with a small amount of δ-ferrite (1.5–1.7 %). The cell size is mostly 12–13 μm. The weld metal hardness in the central part is equal to *HV*1–2950–3090 MPa. In some areas hardness rises up to *HV*1–3200–3380 MPa. In the weld lower part hardness reaches the values of *HV*1–3320–3650 MPa. On the fusion line (Figure 5, *c*) the microstructure also consists of austenite and δ-ferrite, but the structure is finer than that in the weld center. The crystallite width is 2–9 μm. Metal hardness on the fusion line is equal to *HV*1–2990–3030 MPa, with isolated areas, where hardness rises up to *HV*1–3160 MPa. Nitrides (in considerable quantity) are observed in the weld metal. The heat-affected zone (HAZ) is not pronounced, its structure consists of austenite and δ-ferrite. The grain size number in the metal of welded joint HAZ is No.6. HAZ hardness is equal to *HV*1–2650–2840 MPa. Nitrides are found in the HAZ metal.

Discussion. The results of visual and radiographic inspection, metallographic investigations, and static tensile testing were analyzed, in order to determine the influence of laser welding parameters on the characteristics of the produced joints. Graphic dependencies of the characteristics of the produced joints on the most critical factors (technological mode parameters) were obtained.

It was found that at increase of welding speed from 47 mm/s up to 63–72 mm/s, the total projection of pores (total area of pores detected at radiographic inspection) decreases from 0.45 % (of total area of the welded joint) to 0.14 % (Figure 6).

The smallest value of the total quantity of pore projections (0.14 %) was recorded at defocusing of –1 mm that is almost 1.5 times less, compared to welding with similar parameters of speed and laser radiation power, but with defocusing value of +2 mm (Figure 6).

In addition, a greater stability is observed in formation of a small reinforcement (0.7–0.4 mm) of the upper weld bead of the welded joint, at increase of laser welding speed from 47 mm/s to 88 mm/s, respectively (Figure 7).

All kinds of defects of the produced joints were detected. The methods to repair these defects and prevent their occurrence, which were developed and verified by practice, are given in Table 2.

The performed comprehensive analysis of the results of investigations and testing allowed determination of plug welding modes. The criterion for selection of rational parameters of the modes for laser welding of circumferential butt welded joints, were the conditions of compliance with the requirements of «B high» quality category of DSTU EN ISO 13919-1:2015 standard.

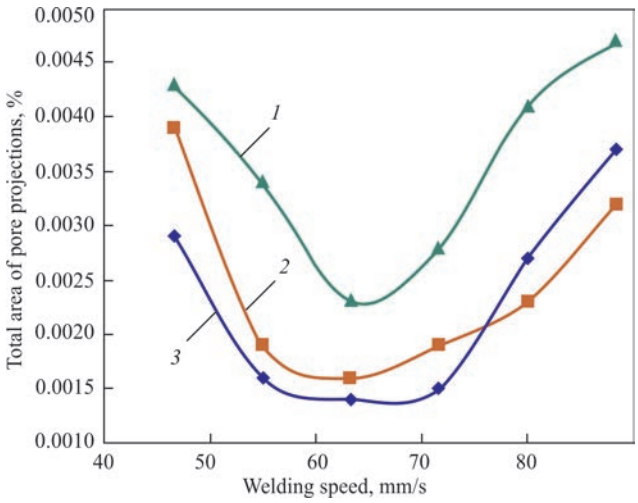

Figure 6. Total area of pore projections depending on speed and defocusing value of laser welding. Defocusing, mm: *1* — +2; *2* — 0; *3* — –1; power P = 4.4 kW

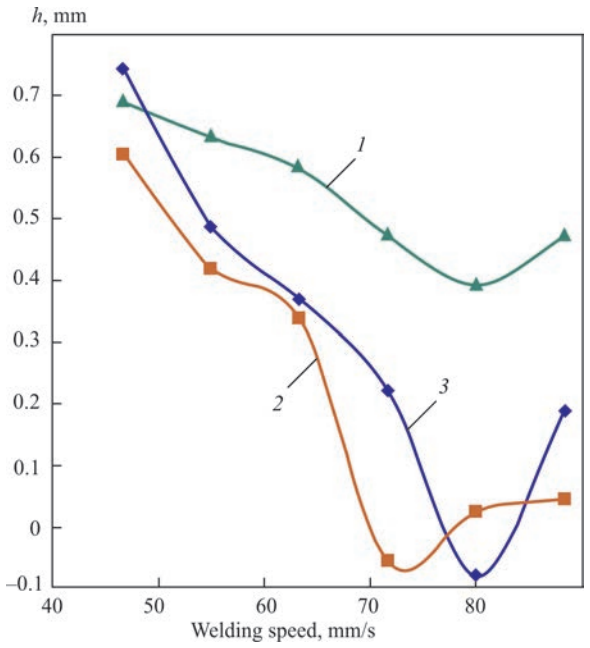

Figure 7. Reinforcement of weld upper bead of welded joint depending on laser welding speed. Power, kW: *1* — 4.4; *2* — 4.0; *3* — 3.6; defocusing — 2 mm

Laser welding of circumferential butt welded joints has the following technological features:

- presence of a section of increase of laser radiation power at the start of welding and section of its decrease at the end, in order to prevent formation of shrinkage and crater cavities;
- parameters of technological modes (laser radiation power; welding time and speed; lens focal position, etc.) for the section of increase of laser radiation power at the welding start and section of its decrease at the end, should be determined empirically for each variant;
- weld sections at the start and end of welding which do not correspond to the conditions of reaching the necessary depth of 1.5 mm, require rewelding, in order to ensure the specified penetration depth;
- unlike arc welding, there is no need for correction of the parameters (laser radiation power: welding time and speed), depending on going through a certain o'clock position, as the process is stabilized after passage of the section with simultaneous increase of laser radiation power and welding speed, and the specified penetration depth can be achieved in all the o'clock welding sections, (downward from 12 to 6 h in clockwise direction, and upward from 6 to 12 h in the clockwise direction, etc.);
- clockwise or counterclockwise direction of movement in welding does not have any significant influence on the structure and characteristics of the welded joint, when the specified depth is reached;
- the point of welding start influences the dimensions of the weld section, in which the welding process is stabilized and the specified penetration depth is achieved;
- for welded joints with weld form factor $K_f < 1$, it is recommended to select 9 o'clock position as the point of welding start and clockwise direction of movement, to achieve quality level «B high».

Welding parameters required to make circumferential butt joints of 10Kh18N10T and 10Kh17N13M3T steels in the vertical position with weld form factor $K_f < 1$ and incomplete penetration, were determined empirically. They meet the requirements of quality category «B high» of DSTU EN 13919-1:2015 standard.

Conducted comprehensive analysis of investigation and testing results allowed determination of modes for plug welding in. The criterion for selection of rational parameters of the modes of laser welding of circumferential welded joints were the conditions of compliance with the requirements of quality category «B high» of DSTU EN ISO 13919-1:2015

Table 2. Measures for defect repair or prevention

Defects	Repair/prevention
Pores, pore sequences, lacks-of-fusion; weld sinking, lacks-of-penetration	Weld root rewelding with addition of filler material (if required)/–
Shrinkage and crater cavities	–/ program control of smooth increase and decrease of laser beam power at the weld start and finish
Undercuts, excess convexity	–/ additional remelting by a defocused beam
Increase of weld cross-sectional area	–/ widening of the zone of laser beam impact by lens divider

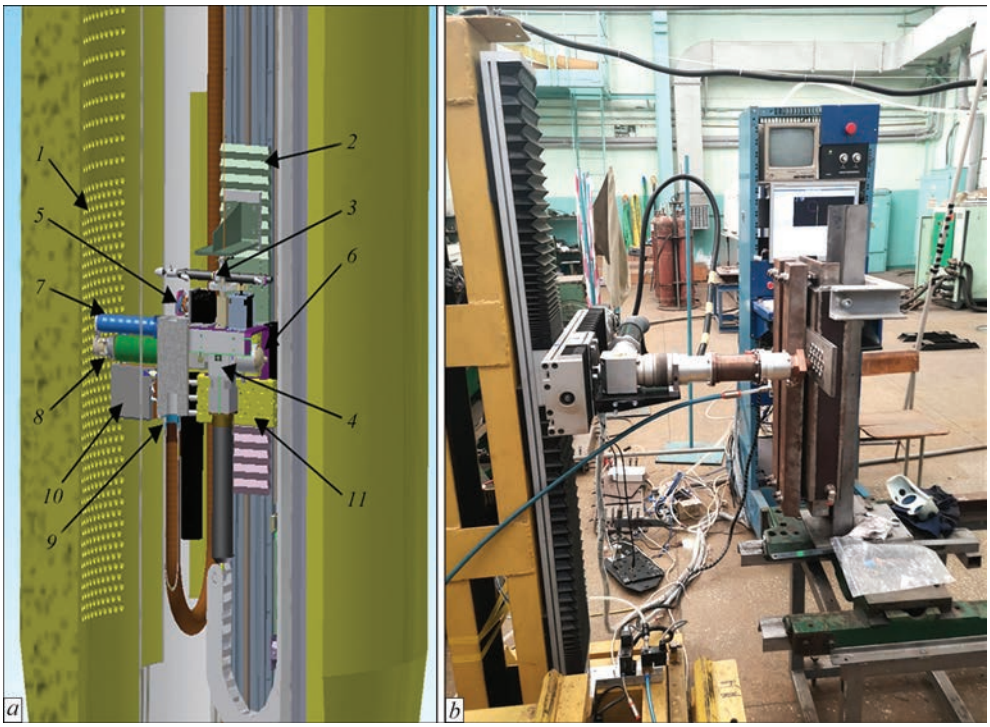

Figure 8. 3D-model (*a*) and working model (*b*) of equipment for remotely-controlled welding in of steam generator collector plugs: *1* — collector wall; *2* — manipulator carriage; *3* — automatic device for installing the plug; *4* — case of laser welding head optics; *5* — scanner; *6* — video camera; *7* — corrugated hose for removing vapours; *8* — gas protection device; *9* — filtering system; *10* — welding position sensor; *11* — drive of welding position sensor

Figure 9. Appearance of welded joints on simulator-samples with plugs welded by laser process

standard. In order to produce welded joints with weld form factor $K_f < 1$, it was proposed to perform laser welding of plugs with the following technological parameters: laser radiation power of 4.4 kW; welding speed of 63.33 mm/s; defocusing value of 1 mm; shielding gas (argon) flow rate of 0.33 l/s (333 cm^3/s); beginning of movement from 9 o'clock position, and clockwise movement direction. During welding in the above mode, the movement mechanism makes two full rotations clockwise, and laser radiation power is varied by a program with a specialized cycle. This way, the stages of increase of penetration depth, its stabilization and decrease are ensured, as well as absence of defects in the form of craters.

A 3D model (Figure 8, *a*) and draft design of the equipment for remotely-controlled welding in of plugs were developed. It was the base for making the working model of a laboratory stand for remotely-controlled laser welding in of plugs (Figure 8, *b*). The created model was used to perform pilot testing of the developed remotely-controlled equipment for repair and restoration of the performance of steam generators of PGV-1000M type on simulator-samples (Figure 9).

Results of visual control and comparative analysis of the geometrical characteristics of welded joints produced by laser (Figure 9) and argon-arc welding revealed the main differences between them. Argon-arc welding is characterized by overlapping of the adjacent welded joints. Unlike argon-arc welding, laser welding provides highly local heat impact that enables extending the service life of welded joints.

Conclusions

1. Remotely-controlled automatic equipment was developed and laser welding technologies were verified for repair and restoration of performance of steam generators or PGV-1000 type.

2. Results of the conducted investigations show that laser welding is a promising technology for replacement of argon-arc welding at repair of steam generator heat exchangers in nuclear and thermal power plants. It provides highly local heat impact and extends the service life of welded joints.

3. Analysis of the main causes for defect initiation at laser welding of circumferential welded joints of dissimilar stainless steels allowed proposing and verifying in practice the measures for repair of these defects and prevention of their formation.

1. Kvasnytskyi, V.V., Kvasnytskyi, V.F., Hexing, C. et al. (2018). Diffusion welding and brazing of dissimilar materials with controlled stress-strain state. *The Paton Welding J.*, **12**, 70–76. DOI: https://doi.org/10.15407/tpwj2018.12.07
2. Wu, Q., Xu, Q., Jiang, Y., Gong, J. (2020). Effect of carbon migration on mechanical properties of dissimilar weld joint. *Engineering Failure Analysis*, 117, 104935. DOI: https://doi.org/10.1016/j.engfailanal.2020.104935
3. Kvasnitsky, V.V., Kvasnitsky, V.F., Markashova, L.I., Matvienko, M.V. (2014) Effect of stress-strain state on structure and properties of joints in diffusion welding of dissimilar metals. *The Paton Welding J.*, **8**, 8–14. DOI:https://doi.org/10.15407/tpwj2014.08.01
4. (2018) State Enterprise *«National Nuclear Energy Generating Company «Energoatom». Strategic plan of development of State Enterprise «National Nuclear Energy Generating Company «Energoatom» for 2018–2022* [in Ukrainian]. http://www.energoatom.com.ua/files/file/strateg_chniy_plan_2018_2022_04042018.pdf
5. *Steam* generator PGV-1000M. *Description and main characteristics.* http://desnogorskspektr.ru/aes/teoriya-aes/parogenerator-pgv-1000m.-opisanie-i-osnovnye-harakteristiki.html [in Russian].
6. Shugailo, O.P. (2019) *Stress-strain state steam generator tubular elements in emergencies:* Syn. of Thesis for Cand. of Tekhn. Sci. Degree. Kyiv, IM [in Ukrainian].
7. Margulova, T.Kh. (1984) *Nuclear power stations.* Moscow, Vysshaya Shkola [in Russian].
8. Zarazovsky, M.N., Borodij, M.V., Kozlov, V.Ya. (2016) Risk-oriented approach to prediction of integrity and optimization of control of heat-exchange equipment with large defect statistics. *Yaderna ta Radiatsiina Bezpeka*, **4**, 32–38 [in Russian].
9. IAEA-TECDOC-1577. (2007). *Strategy for assessment of WWER steam generator tube integrity*. Vienna, IAEA.
10. Xiang, J., Chen, F.F., Park, H. et al. (2020). Numerical study of the metal vapour transport in tungsten inert-gas welding in argon for stainless steel. *Applied Mathematical Modelling*, **79**, 713–728. DOI: https://doi.org/10.1016/j.apm.2019.11.001
11. Kumar, S.R., Ravishankar, B., Vijay, M. (2020). Prediction and analysis of magnetically impelled arc butt welded dissimilar metal. *Materials Today: Proceedings*, **27**, 2037–2041. DOI: https://doi.org/10.1016/j.matpr.2019.09.054
12. Selvan, C.P.T., Dinaharan, I., Palanivel, R., Kalaiselvan, K. (2020). Predicting the tensile strength and deducing the role of processing conditions of hot wire gas tungsten arc welded pure nickel tubes using an empirical relationship. *Int. J. Pressure Vessels and Piping*, **188**, 104220. DOI: https://doi.org/10.1016/j.ijpvp.2020.104220
13. Sahul, M., Tomčíková, E., Sahul, M. et al. (2020). Effect of disk laser beam offset on the microstructure and mechanical properties of copper — AISI 304 stainless steel dissimilar metals joints. *Metals*, **10**, 1294. DOI: https://doi.org/10.3390/met10101294
14. *Ramakrishna R.*, V.S.M., Amrutha, P.H.S.L.R., Rahman Rashid, R.A., Palanisamy, S. (2020). Narrow gap laser welding (NGLW) of structural steels — a technological review and future research recommendations. *Int. J. Adv. Manuf. Technol.* **111**, 2277–2300. DOI: https://doi.org/10.1007/s00170–020–06230–9
15. Shelyagin, V.D., Bernatskyi, A.V., Berdnikova, O.M. et al. Effect of technological features of laser welding of titanium-aluminium structures on the microstructure formation of welded joints. *Metallofiz. Noveishie Tekhnol*, **42**, 363–379 [in Russian]. DOI: https://doi.org/10.15407/mfint.42.03.0363
16. Li, L., Mi, G., Zhang, X. et al. (2019). The influence of induction pre-heating on microstructure and mechanical properties of S690QL steel joints by laser welding. *Optics & Laser Technology*, 119, 105606. DOI: https://doi.org/10.1016/j.optlastec.2019.105606
17. Soltani, H.M., Tayebi, M. (2018). Comparative study of AISI 304L to AISI 316L stainless steels joints by TIG and Nd:YAG laser welding. *J. of Alloys and Compounds*, **767**, 112–121. DOI: https://doi.org/10.1016/j.jallcom.2018.06.302
18. *Technologies for non-destructive testing and repair of NPP components*. NUSIM 2008 VUJE. https://inis.iaea.org/collection/NCLCollectionStore/_Public/43/124/43124116.pdf

Received 11.11.2020

https://doi.org/10.37434/tpwj2020.12.05

PLASMA TRANSFERRED ARC SURFACING OF COMPOSITE ALLOYS WITH SEPARATE FEED OF TUNGSTEN CARBIDES AND MATRIX ALLOY

A.I. Som and **B.A. Halahuz**
Plasma-Master Co., Ltd.
52 Popudrenko Str., 02094, Kyiv, Ukraine. E-mail: info@plasma-master.com

Various combinations of separate feeding of cast spherical tungsten carbides and matrix alloy into the surfacing zone have been investigated. It has been established that when a self-fluxing nickel-based alloy is used as a matrix, the most stable surfacing process is achieved if tungsten carbides are fed through the axial bore in the focusing nozzle, and the matrix alloy comes through two channels located diametrically opposite to each other at its end. Ref. 6, 1 Table, 11 Figures.

K e y w o r d s : plasma transferred arc surfacing, tungsten carbides, spherical tungsten carbides, self-fluxing alloy, matrix, carbide distribution, wear resistance, microhardness

Plasma transferred arc surfacing (PTA surfacing) of composite alloys based on cast tungsten carbides (furtheron referred to as spherical tungsten carbides (carbides)) is ever wider used in industry to improve the wear resistance of parts operating under the conditions of intensive abrasive wear [1, 2]. A mixture of powders consisting of 40 % carbides and 60 % matrix alloy (by volume) is mainly used as filler material for surfacing. By mass, the proportions are approximately the same, but just reversed. As a rule, the matrix alloys are low-melting self-fluxing nickel-based alloys with different degree of alloying by Cr, Si, B and C. Matrix hardness here varies in the range from *HRC* 20 up to *HRC* 60. The above quantity of carbides is considered to be optimal, ensuring good formation and high wear resistance of the deposited metal, although mixtures with an even high content of carbides are sometimes used in practice. They can be of a fragmentary or spherical shape. Surfacing is performed predominantly using PTA torch with external feed of powders through one or several channels [3]. The fraction of powders in the mixture usually is 63–160 μm.

To achieve maximum wear resistance of the deposited layer, it is highly important for the carbide particles to be uniformly distributed in the deposited bead, both over the cross-section, and by its length. This, in its turn, is largely dependent on uniform distribution of carbides in the powder mixture used for surfacing. Unfortunately, it is difficult to ensure it in practice, as separation of carbides and matrix alloy takes place, because of the large difference in their density (approximately 2:1). This is particularly evident at application of mixtures with carbides. In some areas we can observe an excess of carbides, and in other areas, on the contrary, a lack of it. In the areas of carbide accumulation, violation of the deposited bead formation takes place, because of a lack of the low-melting matrix, and cracking is probable. This disadvantage can be avoided, by applying separate feed of carbide powders and matrix alloy from separate feeders-dispensers. In this case, their required ratio can be accurately maintained during the entire surfacing process.

In this paper the possible schemes of separate feed of powders are considered, and their advantages and disadvantages are analyzed. Investigations were performed using experimental and batch-produced PTA torch of Plasma-Master Co., Ltd.. Used as filler materials were carbides produced by Resurs-1 Ltd, Ukraine and powder of nickel-based alloy of 315-R2 grade of Wall Colmonoy Company, US with *HRC* 32 hardness. The fraction of carbides and Ni-alloy powders was 100–200 and 63–100 μm, and their ratio at feeding was 40 and 60 vol.%, respectively.

Carbides [4] is a highly convenient material for plasma surfacing with separate feed. It has excellent flowability, can be readily dosed, and compared to crushed carbides, it wears the channels in the PTA torch much less.

Surfacing of test samples was performed on plates from steel 20. Bead width was 20–22 mm, its height was 4.0–4.5 mm, and deposition rate was 4 kg/h. Samples were cut out of the surfaced plates for metallographic investigations and for wear resistance testing by SR («stationary ring») procedure [5]. In the latter case, the upper part of the deposited metal layer was ground to the level, where the carbide grains were relatively uniformly distributed over the section. Investigations were performed at PWI.

Figure 1 shows the schematic of PTA surfacing with separate feed, where the matrix alloy powder is fed into the arc through the axial bore of the PTA torch focusing nozzle in the form of a distributed flow,

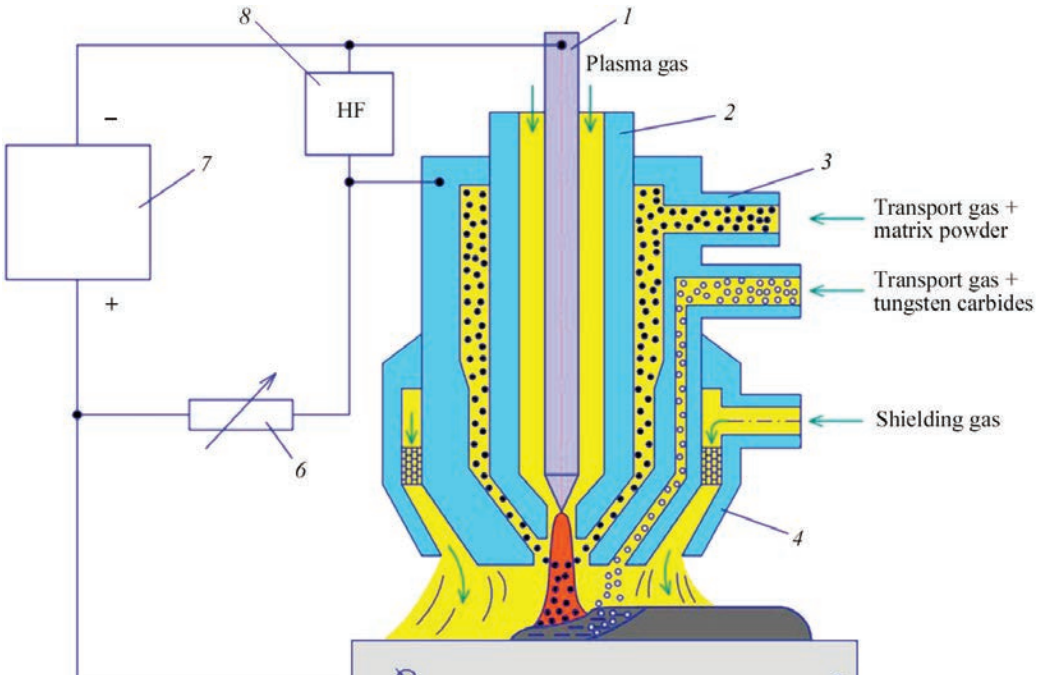

Figure 1. Scheme of PTA surfacing with carbides feeding into weld pool tail part: *1* — electrode; *2* — plasma nozzle; *3* — focusing nozzle; *4* — shielding nozzle; *5* — part; *6* — ballast resistor; *7* — power source; *8* — arc ignition block

and carbides flow through a separate channel directly into the weld pool tail part. The idea of this scheme consists in that the carbide particles did not penetrate under the arc, and were in contact with the weld pool molten metal for as short time as possible. This allows avoiding their melting or dissolution, preserving them in their initial form, and, consequently, providing the maximum wear resistance of the deposited metal.

Realization of this scheme mainly confirmed the assumptions made. Carbide particles are well preserved, the interfaces are very clear-cut (Figure 2). Their microhardness is maximal and is equal to HV_{01} – 2200–2400 Pa. Matrix microhardness is stable by the entire height of the layer and it is close to that of metal, deposited without carbides (HV_{01} – 327–380).This is indicative of the fact that dissolution of carbide particles is practically absent, and the matrix is not enriched with carbon or tungsten, which significantly influence the microhardness. The wear resistance of metal, deposited by this scheme, is also maximal (Table).

This scheme, however, has a number of significant disadvantages. These are unsatisfactory formation of

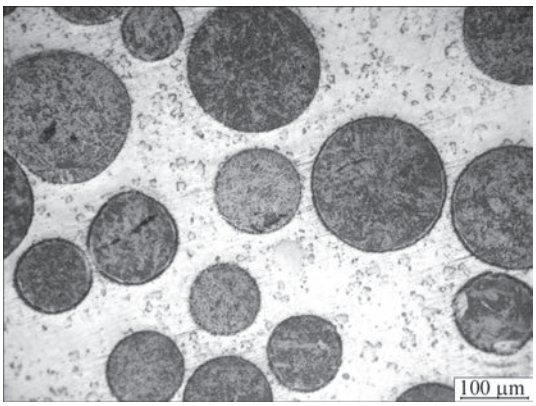

Figure 2. Shape and arrangement of carbide particles in the matrix at its feed into weld pool tail part (×200)

the deposited bead, large carbide losses and high level of internal stresses. Point is that the cold carbide particles «freeze» the weld pool. Its volume decreases and a considerable part of carbides (12–15 %) does not penetrate into it and is lost. Carbides is located mainly in the bead middle part that results in its convex shape. Internal stresses arise on the interface of carbides with the matrix, because of the large difference

Filler powder losses and wear resistance of metal deposited by different schemes of carbides feeding into the weld pool

Number	Scheme of spherical tungsten carbides feeding into the weld pool	Volume ratio of carbides and matrix alloy, %	Total powder losses, %	Wear resistance, SR (mass loss), g
1	Into tail part (Figure 1)	40/60	12–15	0.035
2	Through two channels parallel to bead axis (Figure 3, *a*)	40/60	8–10	0.045
3	Through two channels normal to bead axis (Figure 3, *b*)	40/60	10–12	0.050
4	Through axial bore in the form of mixture (Figure 5)	40 /60	2–3	0.035
5	Through axial bore (Figure 6)	40/60	3–5	0.040
6	Through axial bore (Figure 6)	50/50	4–6	0.045

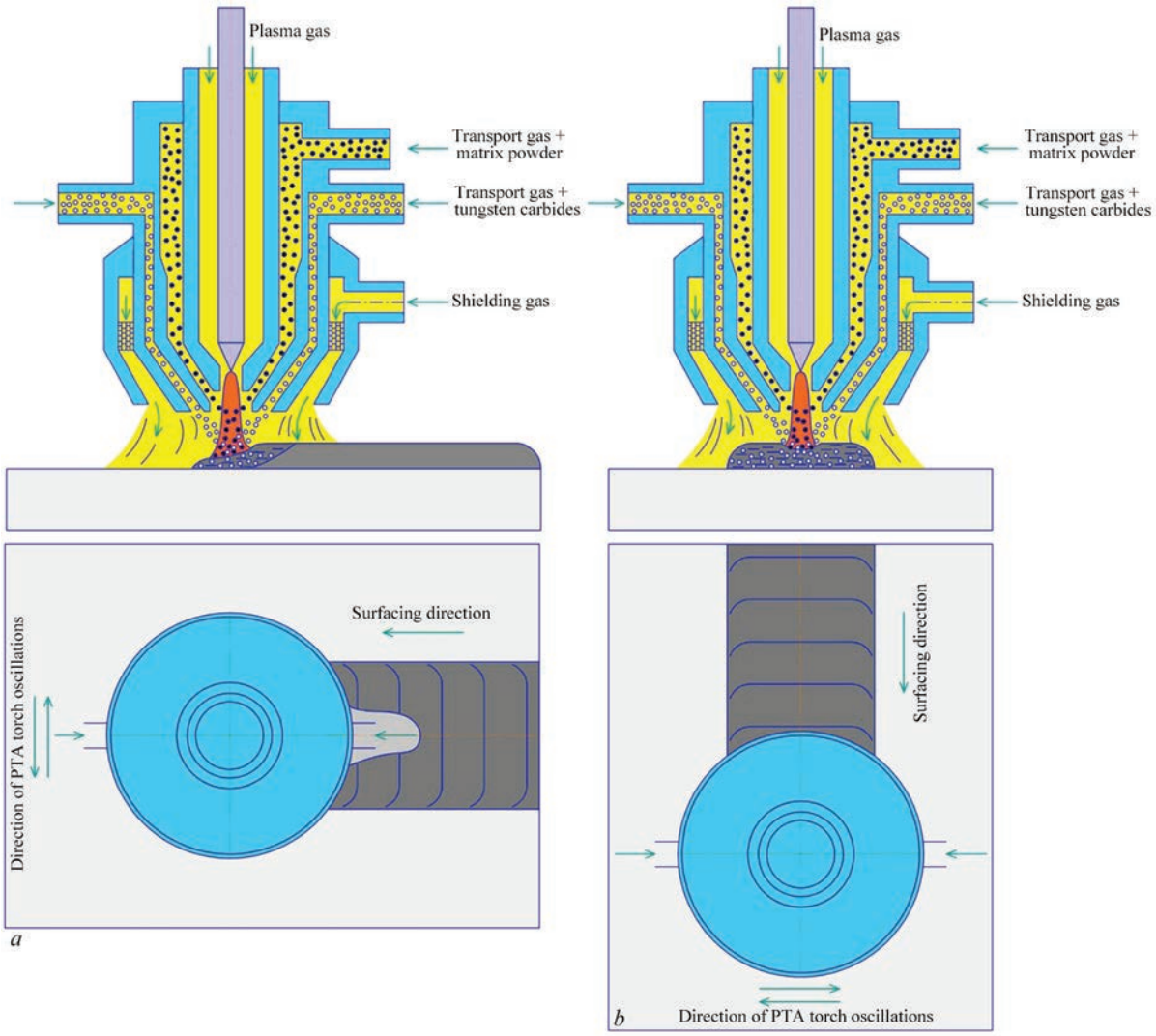

Figure 3. Schemes of PTA surfacing with carbides feeding into the weld pool head part through two channels: *a* — channels are located in the plane parallel to deposited bead axis; *b* — normal to axis

in the coefficients of thermal expansion. At surfacing of massive parts this can lead to appearance of microcracks and cause spalling of deposited metal, particularly at application of hard matrices.

The schemes of carbides feeding into the pool head part from two channels located diametrically opposite to each other in the end part of the focusing nozzle give the best result. This is true in the case of feed channel location both in the plane parallel to the deposited bead axis (Figure 3, *a*), and normal to it (Figure 3, *b*).

To achieve the maximum effectiveness, the angle of carbide feeding and the distance from PTA torch end to the workpiece were selected so that the powder particles fell into the weld pool hottest zone near the arc anode spot. In this case, they are heated very well and do not noticeably cool down the weld pool. With a correctly selected surfacing mode, first of all, optimal arc current, well formed beads can be obtained at small losses of carbides (see Table). Contrary to expectations, the carbide particles do not have time to melt under the arc. They quickly sink to the weld pool bottom and are closely packed in its lower part (Figure 4, *a*). Just a white fringe of the decarbonized layer can be observed on the particle surface (Figure 4, *b*). Microhardness of carbide particles is the same as in the previous case. An unfilled layer of the matrix forms in the bead upper part, above the carbide layer.

Of these two schemes, preference should still be given to a scheme with longitudinal arrangement of the feed channels, as it ensures smaller losses of carbides. This is usually noticeable at wide-layer groove surfacing with PTA torch oscillations. Here, in its extreme positions, carbides are fed into the weld pool more precisely and less is lost.

The smallest loss of carbides (see Table) and better formation of the deposited bead are ensured by a scheme, where carbides are mixed with the matrix alloy inside the PTA torch and penetrate into the weld pool together with them in the form of a distributed flow (Figure 5). A principal difference of this scheme from the previous ones consists in that carbides come to the weld pool in a heated state after passing through the arc. Due

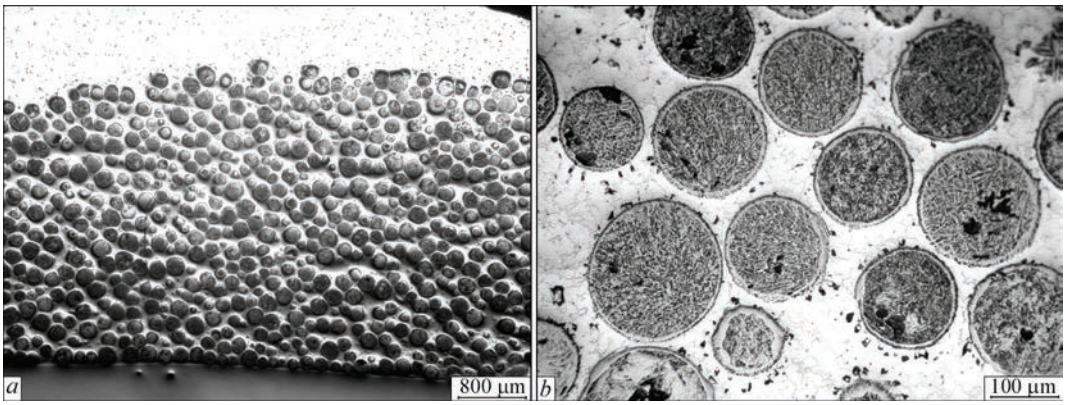

Figure 4. Distribution and shape of carbide particle at feeding through two channels located diametrically opposite to each other in the end part of focusing nozzle: *a* — ×25; *b* — ×200

to that they do not cool the weld pool, but, on the contrary, increase its heat content that promotes their rapid distribution in the liquid metal. Despite the preheating of particles in the arc, as shown by experiments, the carbide particles do not have enough time to melt under the arc, as they immediately sink to the bottom. A layer of low-melting matrix forms on top, which protects them.

Self-fluxing nickel-based alloys of Ni–Cr–Si–B system are very convenient for application as a matrix alloy at surfacing with composite alloys. They have a low-melting temperature (1000–1100 °C), readily wet the carbide particles and have rather good inherent wear resistance. However, at plasma surfacing with these alloys, using PTA torch with internal powder feed [3] there are a number of technological difficulties, related to their low-melting temperature. Fine powder particles (up to 100 μm) which penetrate into the central high-temperature region of the arc have enough time to heat up to evaporation temperature during their flight [6]. Metal vapours deposit on the cold walls of the focusing nozzle, forming a kind of insulation interlayer in the form of accretion. This interlayer is growing steadily during surfacing, and a moment comes, when it starts melting, forming drops at the focusing nozzle outlet. These drops block powder outflow and, eventually, disrupt the surfacing process. Moreover, volatile fractions from the weld pool deposit on the focusing nozzle edge, forming a loose deposit with time, which, if not removed, also disrupts the surfacing process. This adverse phenomenon can be partially avoided, if a coarser powder (more than 100 μm) is used, but it cannot be eliminated completely, as a dust-like fraction (up to 5 %), which remains after screening, is always present in the powder.

At external feeding through separate channels, the effectiveness of powder heating is much lower [6] and no filler powder drops form inside the focusing nozzle, although sticking of volatile fractions to its edge

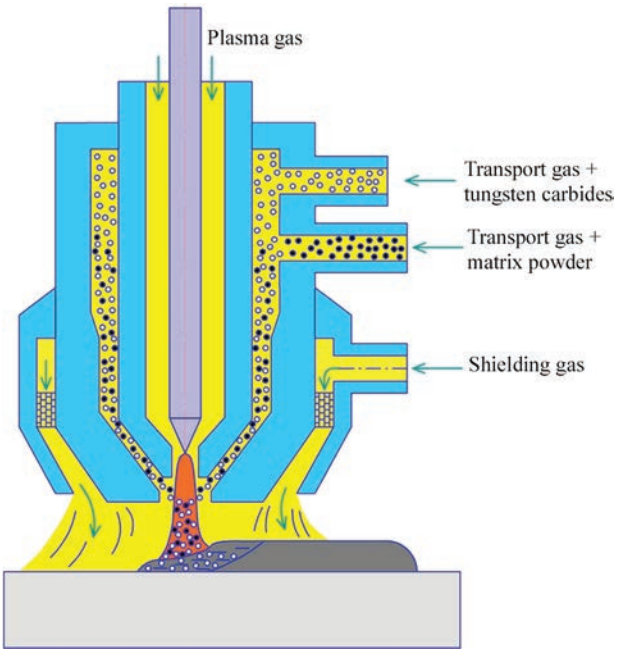

Figure 5. Scheme of PTA surfacing with feeding carbides mixed with matrix powder inside the PTA torch distribution chamber

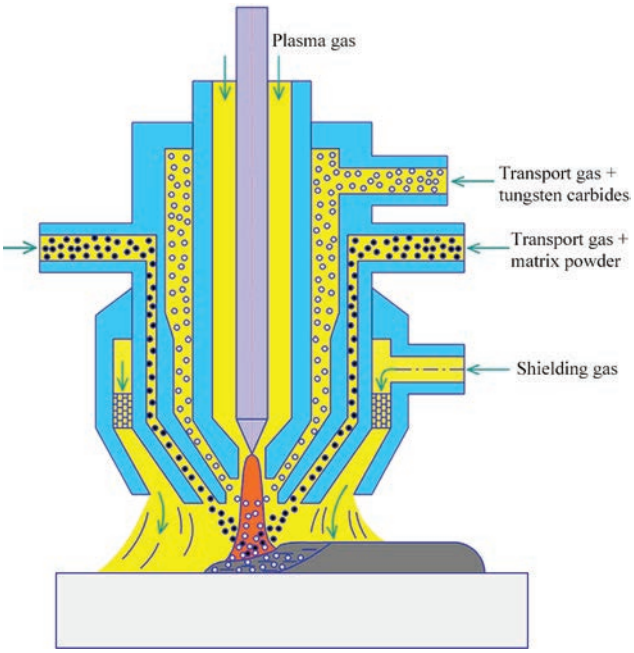

Figure 6. Scheme of PTA surfacing with feeding carbides into the weld pool through axial bore of focusing nozzle

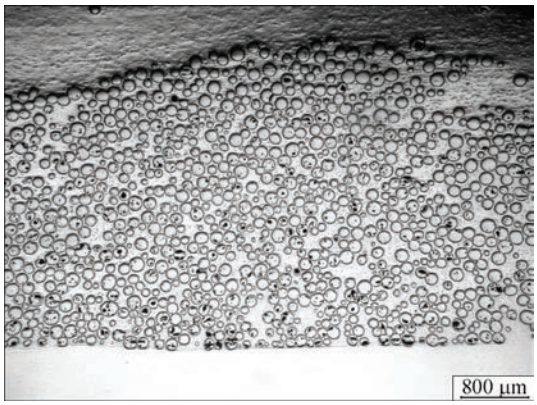

Figure 7. Carbide distribution in deposited metal at its feeding through axial bore of focusing nozzle (40 vol.%)

still takes place, but to a smaller degree. In this connection, the scheme of deposition of composite alloys presented in Figure 6, is the most preferable in terms of process stability. With this scheme, only carbides are fed into the weld pool through an axial bore of the focusing nozzle, and the matrix alloy comes through two diametrically opposite channels, i.e. conversely to earlier discussed schemes (Figure 3).

Carbides, as a higher melting material, do not have enough time to heat in the arc up to melting temperature during their flight, and, therefore, do not have any adverse influence on the surfacing process. Contrarily, preheating, similar to the previous case, promotes denser and faster distribution of carbide particles in the weld pool and lowering of internal stresses in the deposited metal. Carbide distribution by this feed scheme is shown in Figure 7.

As one can see, carbide particles are rather closely and uniformly arranged in the lower part of the deposited bead. Together with matrix alloy interlayers they take up approximately 2/3 of its cross-section. The bead upper part remains unfilled with carbides. It is natural that the wear resistance of this part is not high. However, excess amount of matrix alloy promotes good formation of the deposited bead (Figure 8, *a*), improves cracking resistance and is a kind of protection for carbide particles from dissolution under thermal impact of the arc.

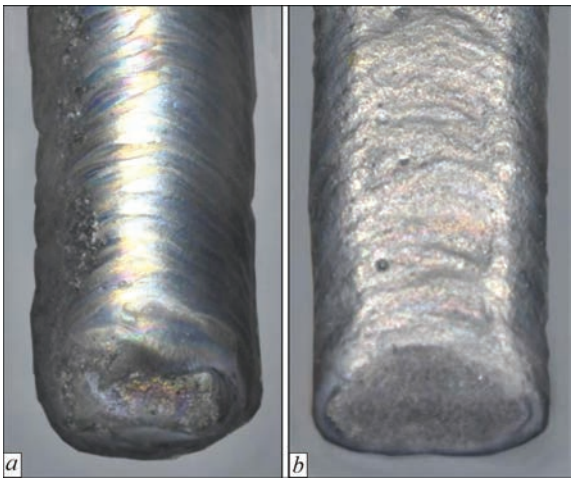

Figure 8. Appearance of beads deposited with carbide feeding through axial bore of focusing nozzle: *a* — 40; *b* — 50 vol.% of carbides

Additional experiments showed that with this scheme the carbide content in the filler material can be increased up to 50 vol.% without disturbance of the surfacing process, in order to improve the bead filling with carbides. The bead shape becomes more flat and favourable from the view point of wear resistance (Figure 8, *b*).

At the same time, metallurgical investigations showed (Figure 9) that with increase of carbide percentage some carbide particles start breaking up.

This is attributable to the fact that in this case the deposited bead is filled with carbides almost to the top, the protective layer of the low-melting matrix becomes insufficient and its particles now are on the surface under the concentrated plasma arc. Melting and dissolution of the carbide particles is further promoted by that the arc current also has to be increased with increase of the amount of carbides in the mixture, enhancing the thermal impact on the particles. It results in matrix enrichment in carbon and tungsten that leads to a certain increase of matrix hardness. In our case, this increase is small (up to HV_{01} – 400–420 Pa) and it does not cause any noticeable embrittlement of it.

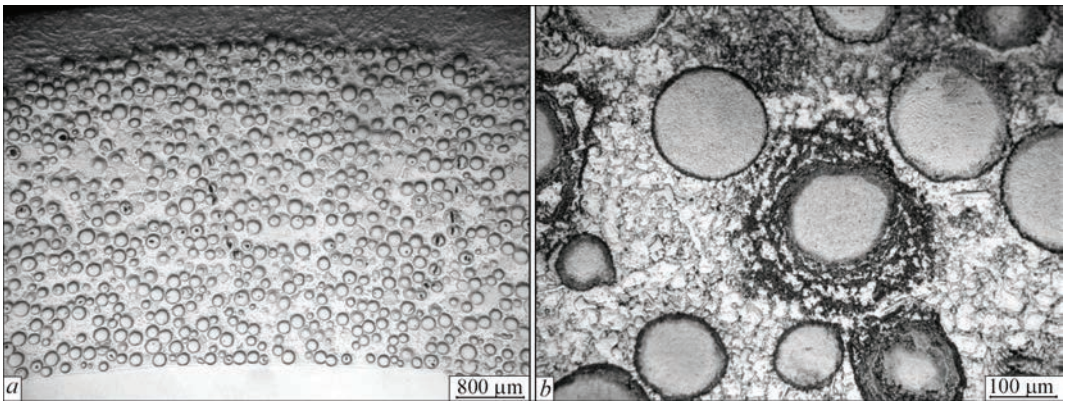

Figure 9. Distribution and shape of carbide particles in the deposited metal at their feeding through axial bore in focusing nozzle (50 vol.%): *a* — ×25; *b* — ×200

Figure 10. Equipment for PTA surfacing with composite alloys with separate powder feed: *a* — PM-302 unit; *b* — PP-6-04 PTA torch

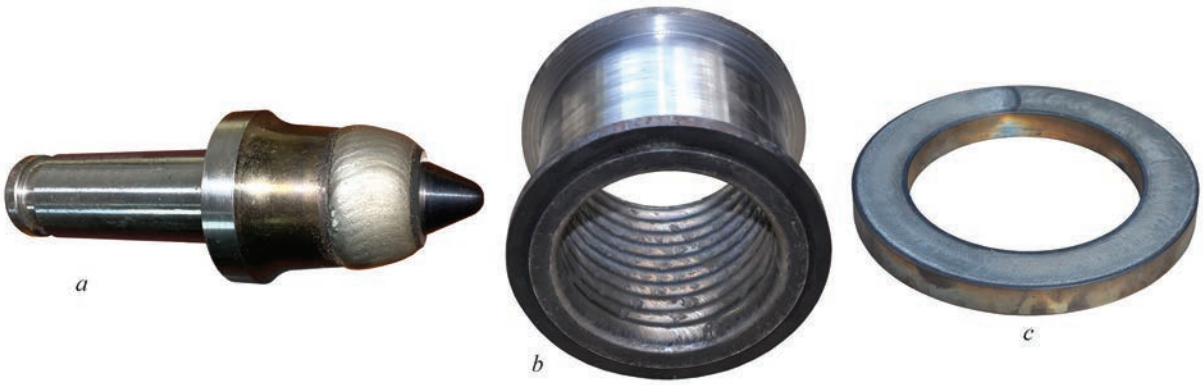

Figure 11. Examples of parts surfaced with composite alloy: *a* — cutter of coal cutter-loader; *b* —crushing equipment case; *c* — pump stabilizing ring

No cracks were observed in the deposited layer. Wear resistance also remained on the same level. This leads to a practical conclusion.

If machining of the deposited layer is required after surfacing to achieve an exact geometrical size, then it is better to deposit the bead so that it is not completely filled with carbides. This facilitates machining, and reduces the consumption of expensive carbides, without lowering the wear resistance of the working layer as a whole. Now if no machining is required by operation conditions, carbide content in the mixture should be increased up to 50 vol.%, and high wear resistance should be ensured by the entire thickness of the deposited layer.

Figure 10 shows equipment for PTA surfacing with composite alloys with separate powder feed, and Figure 11 gives examples of the surfaced parts.

Conclusions

1. At PTA surfacing with composite alloys with separate powder feed the most effective is the scheme, where carbides are fed through the axial bore of the focusing nozzle, and the matrix alloy comes through two diametrically opposite channels, located in its end.

2. To ensure more uniform wear resistance of the deposited layer by height, the volume fraction of carbides can be increased up to 50 % at feeding without violation of the surfacing process.

1. Harper, D., Gill, M., Hart, K W. D, Anderson, M. (2002) Plasma transferred arc overlays reduce operating costs in oil sand processing. In: *Proc. of Int. Spray Conf. YTSC 2002 (Essen, Germany, May 2002)*, 278–283.
2. Som, A.I. (2004) Plasma-powder surfacing of composite alloys based on cast tungsten carbides. *The Paton Welding J.*, **10**, 49–53.
3. Som, A.I. (1999) New plasmatrons for plasma-powder surfacing. *Avtomatich. Svarka*, **7**, 44–48 [in Russian].
4. Zhudra, A.P. (2014) Tungsten carbide based cladding materials. *The Paton Welding J.*, **6–7**, 66–71.
5. Yuzvenko, Yu.A., Gavrish, V.A., Marienko, V.Yu. (1979) *Laboratory units for evaluation of wear resistance of deposited metal. Theoretical and technological principles of surfacing. Properties and tests of deposited metal*. Kiev, PWI, 23–27 [in Russian].
6. Gladky, P.V., Pereplyotchikov, E.F., Ryabtsev, I.A. (2007) *Plasma surfacing*. Kiev, Ekotekhnologiya [in Russian].

Received 02.12.2020

https://doi.org/10.37434/tpwj2020.12.06

CORROSION AND MECHANICAL RESISTANCE OF WELDED JOINTS OF ALUMINIUM B1341T ALLOY, PRODUCED BY ARGON ARC WELDING USING FREE AND CONSTRICTED ARC

L.I. Nyrkova, T.M. Labur, S.O. Osadchuk and **M.R. Yavorska**
E.O. Paton Electric Welding Institute of the NAS of Ukraine
11 Kazymyr Malevych Str., 03150, Kyiv, Ukraine. E-mail: office@paton.kiev.ua

In the work the results of studies of corrosion and mechanical resistance of welded joints of B1341T alloy with a thickness of 1.2 mm, depending on the technology of manual argon arc welding using free and constricted arc are presented. The strength coefficient of welded joints is 0.79 and 0.8, respectively. Potentiometric measurements established an electrochemical heterogeneity between the base metal and the welded joints produced using free and constricted arc, which is equal to 100 mV and 86 mV, respectively. More positive potential is inherent to the region of a weld with a smaller area, which is safe to operation. Accelerated corrosion tests determined that the shape of the arc column during manual welding does not affect the resistance of welded joints to exfoliating corrosion and a corrosion-mechanical resistance under the conditions of a constant deformation. The level of resistance of the metal to exfoliating corrosion of the joints produced by both types of arc welding technology, was estimated by the point 2–3. The fracture time of the specimens welded by free arc welding, decreased on average to 20 days as compared to the base metal (73 days). The similar results were obtained for the joints welded by a constricted arc. At the same time, it was revealed that the use of constricted arc for welding, causes a decrease in the resistance of the joints to intercrystalline corrosion. The maximum fracture depth of the boundaries' grains is 0.350 mm for the joints produced by a free arc and 0.460 mm for the joints made by a constricted arc. 15 Ref., 3 Tables, 11 Figures.

Keywords: aluminium alloy, free and constricted arc welding, welded joint, mechanical properties, structure, intercrystalline corrosion, exfoliating corrosion, corrosion under constant deformation, potentiometry, accelerated corrosion tests

Aluminium alloys of the Al–Mg–Si–Cu alloying system used in aircraft engineering are characterized by a high manufacturability in combination with the characteristics of strength, weldability and corrosion resistance [1–8]. Such group of alloys includes the alloy of grade B1341T, which is used for the manufacture of structures of cylinders, tanks, where liquid substances are stored [3]. Namely due to this fact it is necessary to provide that the products have the optimal level of both mechanical and corrosion properties. Under the production conditions, individual structural elements of hydraulic tanks after stamping are often joined by manual argon arc welding using a nonconsumable electrode with free or constricted arc [1, 4, 7]. A free arc is characterized by a relatively low penetrating ability. The use of pulsed arc modes improves the shape and size of the welds, the conditions of their solidification, and also helps to reduce the loss of strength of the base metal during welding. Due to a cylindrical shape of the arc column, which is formed as a result of its constriction by a layer of inert gas, during welding with a constricted arc, an increase in heat concentration occurs. In addition, it is known [2–4] that the stability of the weld metal usually does not coincide with the stability of the base metal as a result of the formation of a heterogeneous joint structure during welding. Therefore, the aim of this work is to study the influence of manual welding technology using free and constricted arc on the complex of corrosion and corrosion-mechanical properties of welded joints (WJ) of B1341T alloy to determine the efficiency of these processes.

Procedure of experiments. In the work, aluminium B1341T alloy is used, the chemical composition of which according to spectral analysis performed in the DFS-36 spectrometer, is the following, wt.%: (0.45–0.9) Mg, (0.5–1.2) Si, (0.15–0.35) Mn, (0.1–0.5) Cu, (0.05–0.1) Ca, 0.25 Cr, 0.2 Zn, 0.15 Ti, 0.5 Fe, the content of other elements is not more than 0.1, Al is the base.

The sheet billets of B1341T alloy with a thickness of 1.2 mm before welding were etched in a 10% solution of NaOH and clarified in a 25 % solution of HNO_3, thoroughly washed in running hot and cold water and dried in air. The ends of the workpieces

L.I. Nyrkova — https://orcid.org/0000-0003-3917-9063, T.M. Labur — https://orcid.org/0000-0002-4064-2644,
S.O. Osadchuk — https://orcid.org/0000-0001-9559-0151, M.R. Yavorska — https://orcid.org/0000-0003-2016-6289

were mechanically cleaned with a scraper to a depth of 0.1 mm. Welding of butt joints was carried out along the rolled sheet metal of a semi-finished product. The billets were welded abutt, without a backing, using single-pass manual welding with a filler wire of grade Sv 1217 with a diameter of 1.2 mm in argon (according to GOST 10157 [9]). Figure 1 shows a diagram of the sequence and modes of welding.

Free arc welding was performed at a current of different polarity of a sinusoidal waveform using the MW2000 Fronius inverter, and welding using a constricted arc was performed at an asymmetric current of different polarity of a rectangular waveform and overload of the current duration using the PLASMA POWER SUPPLY, which was designed at the PWI for manual and automatic welding of thin-sheet ferrous and nonferrous metals of 0.3–1.5 mm at direct and alternating current. Welding modes and welding materials are presented in Table 1.

The appearance of the welded joints produced during free and constricted arc welding is shown in Figure 2.

Determination and evaluation of mechanical properties were performed on flat specimens with a technological reinforcement on the facial and back surfaces of the weld. The tests were performed according to [11, 12] in the machine MTS 318-25. The load was applied at a traverse speed movement of 2 mm/min before a fracture. During the tests, the load and deformation indices were continuously recorded, according to which results the values of the corresponding indices were calculated: yield strength, ultimate strength (tensile strength) and elongation. The level of deformation ability of the base metal and welded joints was established by the index of bending angle (α) under the conditions of three-point bending with the application of a load from the root side of the weld in accordance with GOST 6996 [12].

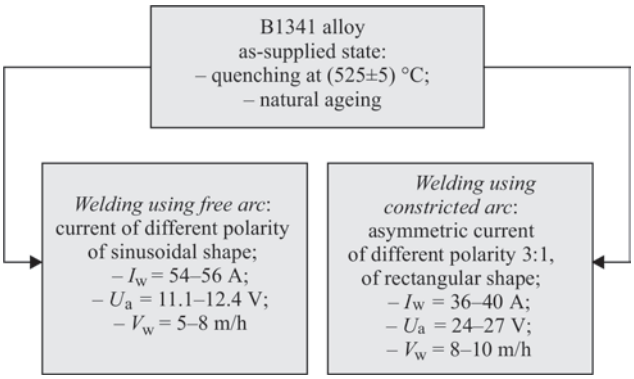

Figure 1. Scheme of sequence of performing operations of producing specimens for investigations and their modes

The microstructure of welded joints was studied on metallographic sections, which were cut out perpendicular to the axis of the welds and prepared according to a standard procedure. To detect the microstructure, electrolytic etching in a solution of the composition: 930 ml of CH_3COOH + 70 ml of $HClO_4$ was used.

Electrochemical investigations were performed by the methods of potentiometry and polarization curves using the potentiostat PI-50-1.1 and the programmer Pr-8. The distribution of potential on the surface of the welded joint was investigated by measuring the potential under the drop in the solution of 3 % NaCl

Table 1. Modes of manual one-sided argon arc welding of B1341T alloy of 1.2 mm thickness using nonconsumable electrode with free and constricted arc

Welding method	Diameter of tungsten electrode, mm	Diameter of filler wire, mm	Argon consumption, l/min	Consumption of shielding gas, l/min	Consumption of plasma-forming gas, l/min	Ratio of direct and reverse polarity
Free arc [10]	1.6	2.0–2.5	7–8.0	–	–	–
Constricted arc	1.6	2.0	4.0–8.0	3.0–6.0	0.8–1.5	3/1

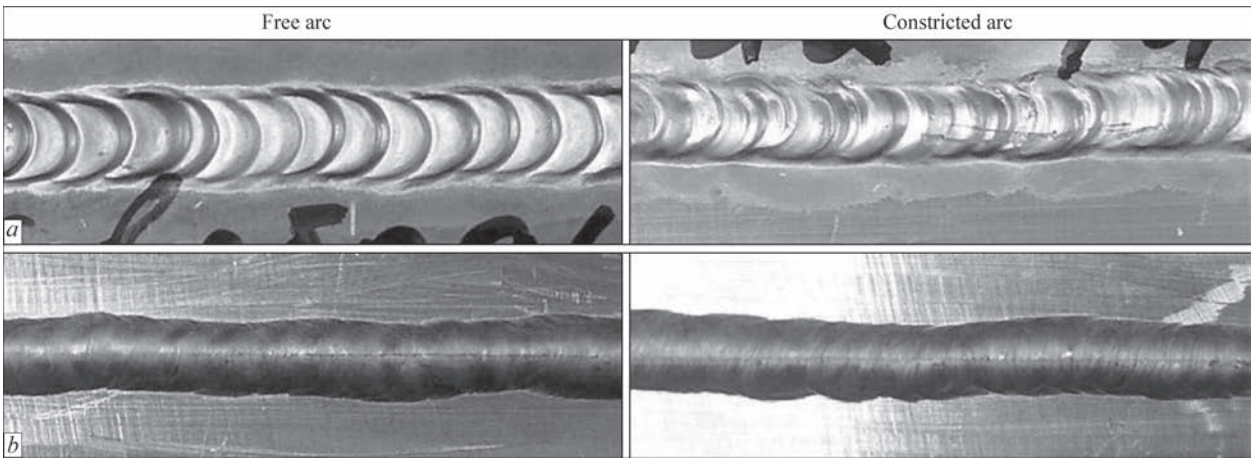

Figure 2. Appearance of as-welded joints: *a* — facial weld surface; *b* — weld root

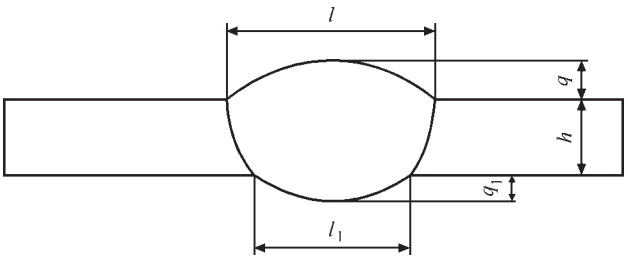

Figure 3. Scheme of measuring geometric dimensions of welds to calculate its form factor

according to the procedure developed at the PWI. To analyze the polarization curves, a clamping electrochemical cell was used. The working electrode was different zones of the welded joint, the reference electrode was a saturated silver chloride electrode EVL-1M1 and the auxiliary electrode was platinum. Polarization curves were recorded in a potentiodynamic mode at a potential scanning rate of 0.5 mV/s in the solution of 3 % NaCl. Before measurements, the surface of specimens was treated with a sandpaper and degreased with ethyl alcohol.

The resistance to intercrystalline (ICC) and exfoliating corrosion was evaluated according by the standard procedures in accordance with GOST 9.021 [13] and GOST 9.904 [14].

The corrosion cracking resistance was investigated in accordance with GOST 9.019 [15]. The tests were performed under the presence of a constant axial tensile stress at the level of 160 MPA at a complete immersion of the specimens of welded joints in the solution of 3 % NaCl in the installation Signal. The test specimens were perpendicularly arranged relatively to the direction of the loading vector action. The duration of the tests was at least 45 days.

Results and their discussion. *Geometric parameters of welds and form factor.* After producing dissimilar joints with the use of different technological methods of manual welding with free and constricted arc, the geometric dimensions of the welds were determined. The explanation of their determination is

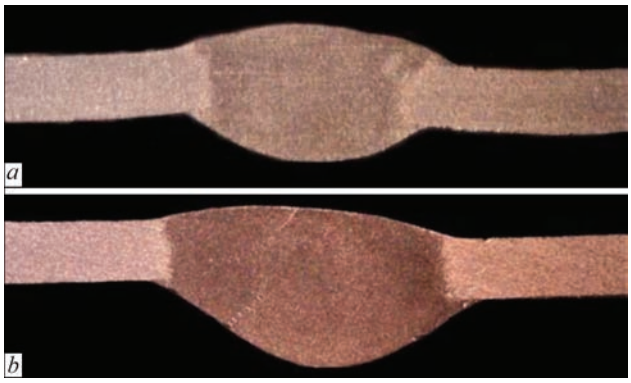

Figure 4. Macrosections of welded joints of B1341 alloy produced by manual argon arc welding at different technological methods of welding using nonconsumable electrode: *a* — free arc; *b* — constricted arc

given in Figure 3, and the obtained results are shown in Table 2. The form factor of the weld was calculated by the formula: $K = l/t$, where $t = h + q$, t is the thickness of the weld; l is the width of the weld; q is the height of reinforcement; h is the greatest depth of the molten base metal.

Analysis of the calculation results showed that weld form factor of the welded joint produced by a constricted arc is approximately 4 % higher as compared to the welded joint produced by a free arc, i.e. it has a little effect on the plane of welds intersection.

Macro- and microstructure of welded joints. Below the results of the study of the macro- and microstructure of the base metal and welded joints of B1341T alloy, produced by free and constricted arc are presented (Figures 4 and 5).

Metallographic examinations established that the microstructure of the base metal of B1341T alloy consists of a saturated solid solution, precipitations of the Mg_2Si phase and coarse inclusions of insoluble intermetallics, which enter the metal at the metallurgical stage of semi-finished product manufacturing (Figure 5, *a*). During arc welding of B1341T alloy, structural transformations take place in the metal, as a result of which three structural zones are formed: weld (Figure 5, *a*),

Table 2. Geometric parameters and form factor of welds produced by free and constricted arc during manual welding of B1341 alloy with a thickness of 1.2 mm

Welding method	Designation of parameters	Geometrical parameters of welds, mm				Weld form factor
		Minimum	Average	Maximum	Average	
Manual welding using free arc	l	3.53–4.86	4.68	4.92–5.60	5.2	2.43
	l_1	3.15–4.15	3.84	4.2–5.1	4.55	
	q	0.23–0.70	0.47	0.8–1.3	0.94	
	q_1	0.17–0.68	0.5	0.85–1.15	0.91	
Manual welding using constricted arc	l	3.99–4.80	4.42	4.9–5.5	5.17	2.52
	l_1	3.52–4.50	4.04	4.65–5.35	4.89	
	q	0.15–0.56	0.38	0.6–1.3	0.85	
	q_1	0.35–0.58	0.48	0.75–15	0.97	

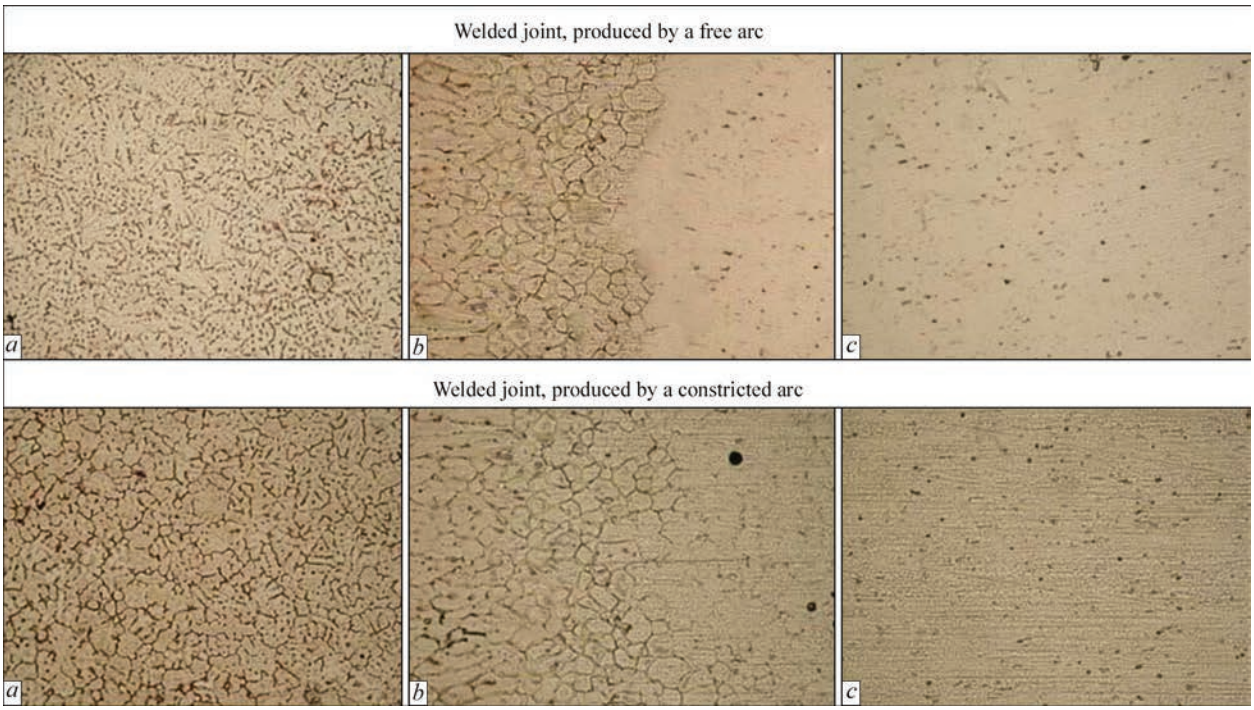

Figure 5. Microstructure (×320) of different zones of welded joints of B1341T alloy, produced by constricted and free arc: *a* — weld; *b* — fusion zone; *c* — base metal

fusion zone and heat-affected-zone (HAZ) (Figure 5, *b*). The structure of the welds of the specimens after welding is homogeneous with the characteristic arrangement of phases and consists of small dendrites (Figure 5, *a*). In the volume of the welds, coarse defects and discontinuities are not observed.

Metallographic analysis of the macrostructure of B1341T alloy joints showed that its welds are characterized by a sufficiently high quality, as there are no coarse defects. In contrast to the base metal (Figure 5), in the welded joint three characteristic parts of the structure are observed, which reflects the degree of influence of the thermal welding cycle on the metal.

The welds have a homogeneous fine-dendritic structure regardless of the arc shape. The size of the dendrites varies in the range of 0.25–0.38 μm. In the process of solidification, the presence of a significant amount of alloying elements and impurities in the composition of the base material and filler wire causes the formation of a significant amount of phases that are uniformly arranged across the joints, but differ in size and shape. According to the state diagram of the system Al–Mg–Si–CuFe in an equilibrium with a solid solution (matrix), such metastable phases can be located as Mg_2Si, $SiCuAl_2$, $FeAl_3$, Mg_5Al_8, and: $CuFeA1_5$, $CuMgAl_2$, $FeSiAl_5$, $FeMg_3Si_6$. The intercrystalline layers are mostly dense and have more distinct contours.

The microstructure of the fusion zone of the weld with the base metal is characterized by the presence of the flashed grain boundaries formed under the conditions of welding heating. This is accompanied by thickening of the boundaries as a result of contact melting of grains with each other and under the conditions of a high-temperature welding heating the formation of the eutectic Mg_2Si phase, located along the grain boundaries (Figures 4, 5). Dissolution of some strengthening phases is also noted. In the structure of HAZ under the action of the thermal cycle of welding, separate fragments of grain boundary flashing and a partial precipitation of secondary phases and eutectics are observed. In addition, coarsening (coagulation) of inclusions of insoluble harmful phases takes place, which reduces the strength of the metal in HAZ.

It should be noted that during welding by a free arc, the width of the HAZ decreases. It can be assumed that such a joint will have a higher corrosion resistance under operating conditions due to a lower heterogeneity of the product.

Mechanical investigations. The mechanical properties of the specimens produced using different technological methods are presented in Figure 6. The analysis of the obtained results shows that the specimens of the base metal are fractured in the working area, and the fracture of specimens of both types of welded joints occurs in the HAZ at a distance of 3–5 mm from the fusion boundary. As compared to the strength of the base metal, the level of these characteristics for welded joints is lower by 22 and 20 %, the yield strength is by 30 and 23 %. The coefficient of strength of welded joints is 0.79 and 0.8. The difference in the shape of the arc has a stronger effect on the characteristics of ductility. Thus, the bending

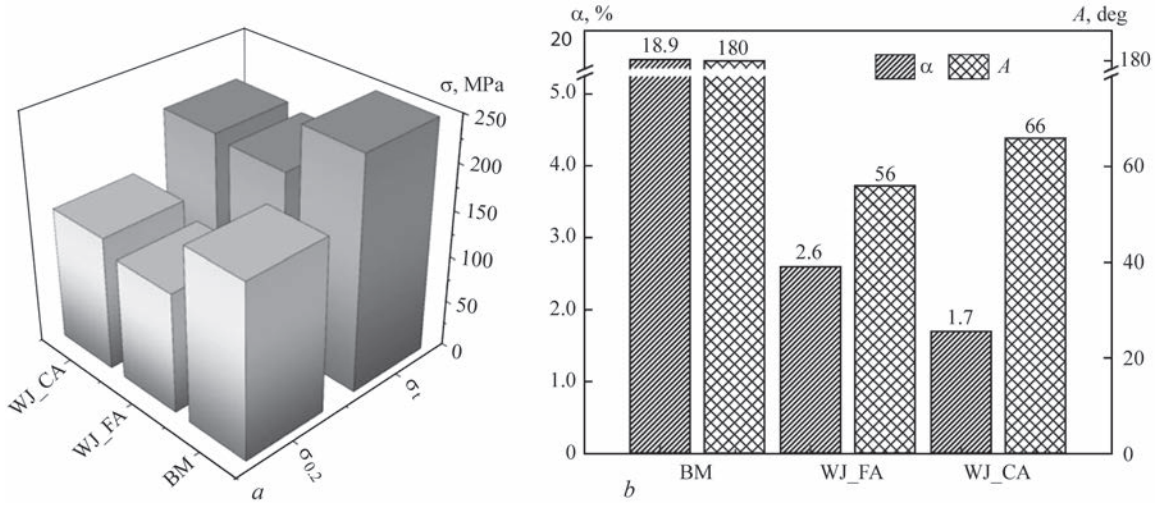

Figure 6. Mechanical properties of welded joints and base metal: *a* — tensile and yield strength; *b* — elongation and bending angle (WJ_CA — welded joint produced by a constricted arc; WJ_FA — welded joint produced by a free arc; BM — base metal)

angle is reduced by 70 and 63 %, and the elongation is by 86 and 91 %. Thus, the joint produced by a constricted arc has a higher tensile strength, ductility and bending angle as compared to the joint produced by a free arc, but the value of the elongation is less than in Figure 6. Probably, this is connected with coarsening (coagulation) of inclusions of insoluble harmful phases as a result of the action of the thermal cycle of a constricted arc welding. Thus, a constricted arc welding contributes to some extent to the strength of welded joints, but at the same time a decrease in the level of ductility is noted.

Electrochemical investigations. The corrosion potential of the base metal is almost –0.729 V. The potential difference between the base metal and the weld is 0.100 V and 0.08 V for the joints produced by free and constricted arc, respectively (Figure 7). Therefore, the potential difference is quite high, but a corrosion potential of the weld is more positive than that of the base metal. The potential difference between the base metal and HAZ is within the values of 0.100 V for the joint produced by a free arc and 0.086 V for that produced by a constricted one, which are admissible by GOST 9.005 (Figure 7, curves *1* and *2*).

From the analysis of experimental results it follows that both types of welded joints have an electrochemical heterogeneity. However, the more positive potential is inherent to the zone with a smaller area and does not represent a danger during operation. Electrochemical heterogeneity between the base metal and the HAZ occurs also in the joints produced by both technologies, which should be taken into account during operation of a welded structure.

Polarization curves measured on the base metal and the weld are presented in Figure 8. It is seen from Figure that the anode and cathode curves, obtained on the welds of both joints, coincide, which is quite natural. The current of anode dissolution on the weld of the specimens of both welded joints (Figure 8, curves *2*, *3*) is much higher than that on the base metal. The cathode curves of the welds are shifted to a region of lower currents as compared to the base metal. In

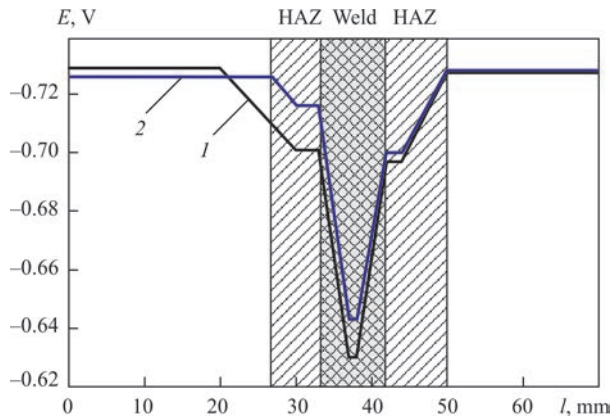

Figure 7. Nature of distribution of potentials under the drop at different zones of welded joint of B1341T alloy, produced by different technological methods: *1* — free arc; *2* — constricted arc

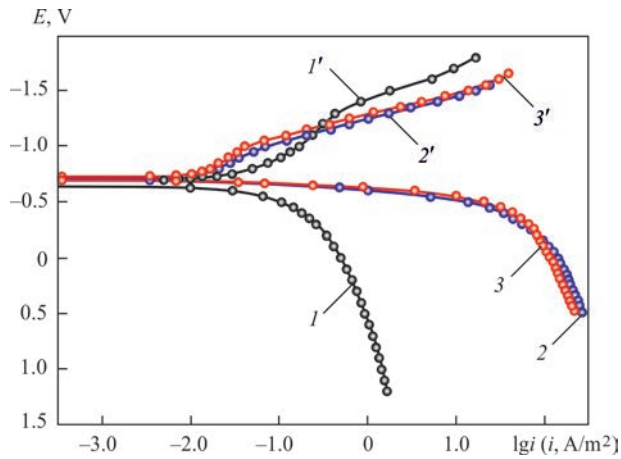

Figure 8. Anode (*1*, *2*, *3*) and cathode (*1′*, *2′*, *3′*) polarisation curves of base metal and weld on welded joint of B1341T alloy: *1* — base metal; *2* — weld of the joint produced by a free arc; *3* — weld of the joint produced by a constricted arc

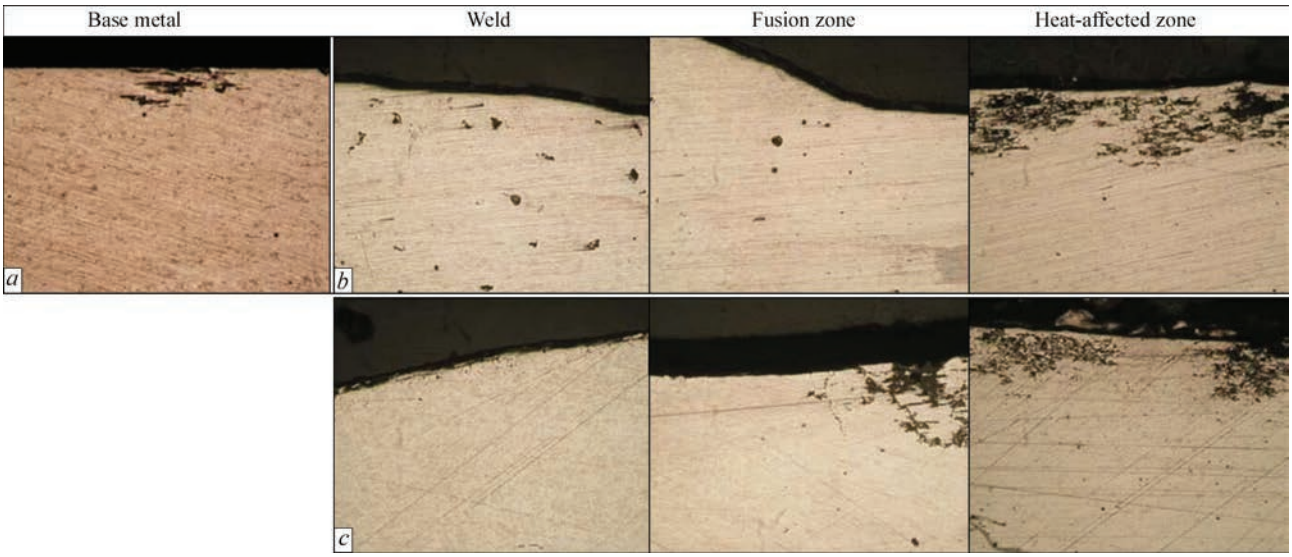

Figure 9. Microstructure (×320) of zones of welded joints of B1341 alloy after the tests on resistance to intercrystalline corrosion: *a* — base metal; *b* — welded joint produced by a free arc: *c* — welded joint produced by a constricted arc

aqueous media at a free access of oxygen, the corrosion process occurs with an oxygen depolarization (Figure 8, curves *1′–3′*). The decrease in the values of the limiting diffusion current on the welds as compared to the base metal indicates a local inhibition of the corrosion process in this area of the welded joint.

Thus, it was revealed that the influence of the applied technological methods of welding almost does not affect electrochemical characteristics of the welded joint.

Resistance to intercrystalline corrosion. The study of resistance to intercrystalline corrosion (ICC) of the base metal showed that the depth of damage to the grain boundaries varies from 0.082 to 0.086 mm. Intercrystalline fracture of the welded joint produced by a free arc was not observed in the area of the weld and the fusion zone (Figure 9, *b*, *c*), but was recorded in the HAZ.

The depth of the damage of the grain boundaries varies from 0.245 to 0.350 mm (Table 3).

On the welded joint produced by a constricted arc, intercrystalline corrosion of the weld was not detected (Figure 9, *b*, *c*). The areas of intergranular fracture are observed in the fusion zone and were propagated to a depth of 0.222 to 0.506 mm and in the HAZ to a depth of 0.222–0.416 mm. Thus, structural transformations and coagulation of insoluble inclusions of harmful phases not only cause a decrease in the strength of the HAZ metal, but also lead to an increase in the local stress at the grain boundaries and, as a consequence, the appearance of a center of intergranular fracture. Thus, the use of welding of thin-sheet metal of B1341T alloy by a constricted arc can reduce the resistance of the welded joint metal to intercrystalline corrosion.

Resistance to exfoliating corrosion. The results of the study of exfoliating corrosion resistance (Figure 10) showed that on the surface of the base metal a change in surface color and delamination with a diameter of not more than 1 mm was revealed. Their total area does not exceed 1.5 % (Figure 10). Delamination at the ends was not detected. According to GOST 9.904, resistance of the base metal of B1341T alloy

Table 3. Mechanical, corrosion and corrosion-mechanical properties of base metal and welded joints of B1341T alloy, produced by free and constricted arc

Condition	Properties of base metal and welded joints							
	Mechanical					Corrosion		Corrosion-mechanical
	σ_t, MPa	$\sigma_{0.2}$, MPa	δ, %	α, deg	Coefficient of WJ strength	Depth of intercrystalline corrosion, mm	Resistance to exfoliating corrosion, point	Time of fracture, days
Base metal	250.5	187.6	18.9	180	–	from 0.082 to 0.086	2–3	from 67 to 88
WJ produced by a free arc	195.0	130.1	2.6	56	0.79	from 0.245 to 0.350	2–3	from 10 to more than 45
WJ produced by a constricted arc	200.3	144.3	1.7	66	0.80	from 0.289 to 0.467	2–3	from 9 to more than 45

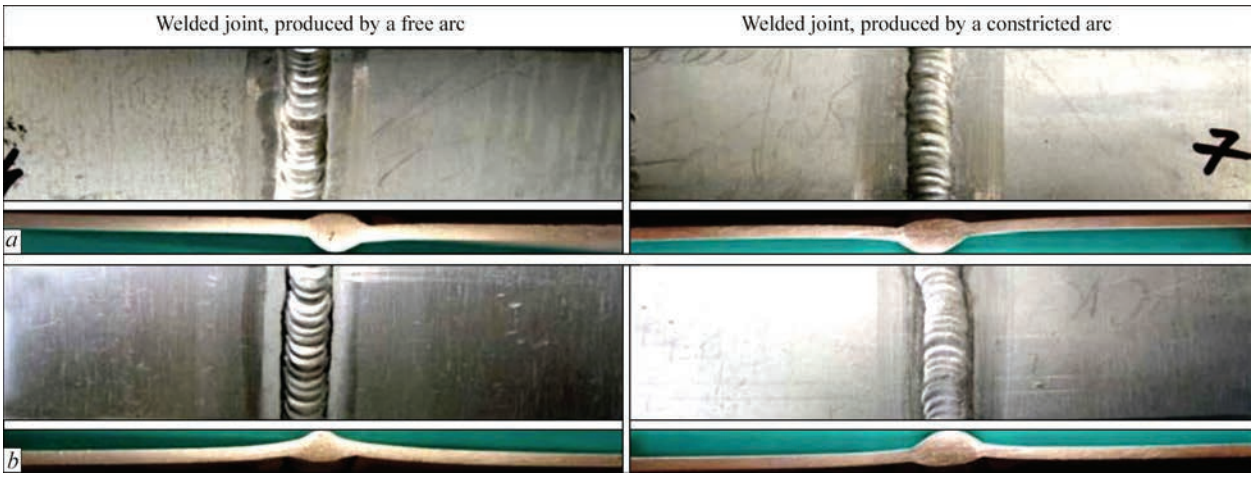

Figure 10. Appearance of working surfaces of specimens of welded joints of B1341T alloy in the state after welding before (*a*) and after (*b*) studies of resistance to exfoliating corrosion (×5)

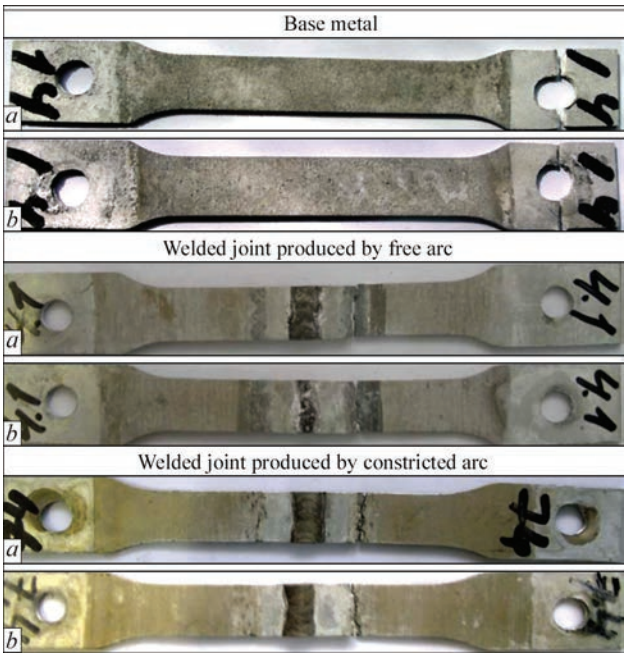

Figure 11. Appearance of specimens of base metal and welded joints of B1341T alloy, produced by free and constricted arc after tests on resistance to corrosion cracking: *a* — facial surface; *b* — back surface

to exfoliating corrosion was evaluated by 2–3 points according to a ten-point scale (Table 3). For welded joints, the condition of the HAZ and weld zone was evaluated. On the surface of the welded joints of both types, delamination in the HAZ and on the weld are also absent. In accordance with the recommendations of GOST 9.904, their resistance to exfoliating corrosion was evaluated by the point I. As far as the resistance of the base metal is slightly lower than that of the area of the weld and HAZ, the resistance of the weld to exfoliating corrosion is generally evaluated by a point 2–3. It was revealed that the peculiarities of the technology of manual argon arc welding using free or constricted arc do not affect the resistance of welded joints to exfoliating corrosion.

Resistance to corrosion cracking. The appearance of the testing specimens after corrosion tests is presented in Figure 11, *a*, *b*. As is seen, on the entire surface of the specimens pittings were formed. In the area of the welded joint, pittings are concentrated mainly in the area of the HAZ, which may indicate the localization of corrosion namely in this part of the welded joints of B1341T alloy. The corrosion-mechanical resistance of the base metal and welded joints in the conditions of joint impact of a constant load at a full immersion in a corrosive environment differs quite significantly (Table 3). A significant scattering of experimental data for both base metal as well as for welded joints is observed. The time before fracture of the base metal specimens ranged from 67 to 88 days (almost 73 days) and for the welded joints produced by a free arc, a decrease in the fracture time to 10–45 days (in average 20 days) was observed. The similar results were obtained for the welded joints produced by a constricted arc. In both cases, the fracture time of the joints made by different welding technologies is almost three times lower than of the base metal. Therefore, the change in technological methods for welding the alloy will not significantly affect the value of a corrosion and mechanical resistance of specimens of welded joints.

Conclusions

According to the results of complex studies of mechanical and corrosion-mechanical properties of welded joints of B1341T alloy with a thickness of 1.2 mm, produced by argon arc welding using free and constricted arc, it was revealed that:

- the strength coefficient of the welded joints produced by free and constricted arc is 0.79 and 0.8, respectively. Thus, the joint produced by a constricted arc has a higher tensile strength and ductility (bending angle) as compared to the joint produced by a free arc, but the values of elongation decrease;
- based on the results of electrochemical investigations, it was determined that after applying both types

of technology, the specimens of welded joints have an electrochemical heterogeneity. At the same time, more positive potential is inherent to the zone of a weld, which has a smaller area, which does not represent a danger during operation;

• it was revealed that the peculiarities of the technology of manual argon arc welding do not affect the resistance of welded joints of B1341T alloy to exfoliating corrosion and corrosion-mechanical strength under the constant deformation. At the same time, the use of a constricted arc welding causes a decrease in the resistance of welded joints to intercrystalline corrosion;

• it was experimentally proved that the corrosion resistance of the welded joint produced by a constricted arc is slightly lower than in the specimens produced by a free arc, but it can be assumed that a well chosen heat treatment of such joints can improve its resistance.

The work was carried out with the support of the National Academy of Sciences of Ukraine within the framework of the program of departmental order of the E.O. Paton Electric Welding Institute in 2017–2021 (state registration number 0117U001188).

1. Feigenbaum, Yu.M., Dubinsky, S.V.(2013) Influence of accidental operational damage on strength and residual life of aircraft structures. *Nauchny Vestnik MGTU GA*, 187, 83–91 [in Russian].
2. Krivov, G.A., Ryabov, V.R., Ishchenko, A.Ya. et al. (1998) *Welding in aircraft construction*. Moscow, MIIVTs [in Russian].
3. Ishchenko, A.Ya., Labur, T.M. (2013) *Welding of modern structures from aluminium alloys*. Kyiv, Naukova Dumka [in Russian].
4. Ovchinnikov, V.V., Grushko, O.E. (2005) High tech welded aluminium alloy V1341 of Al–Mg–Si system. *Mashinostroenie i Inzhenernoe Obrazovanie*, **3**, 2–11 [in Russian].
5. J. Zheng, B., Wang, Q. (1993) lv he jin deng li zi hu li han chuan kong rong chi wen ding jian li tiao jian. *Transact. of the China Welding Inst.*, **3**, 164–171.
6. Martinez, L.F., Marques, R.E, Mcclure, J.C., Nunes, A.C. (1992) Front side keyhole detection in aluminium alloys. *Welding J.*, 71(**5**), 49–52.
7. Norlin, A. (2000) A century of aluminium — a product of the future. *Svetsaren*, 2(**2**), 31–33.
8. Albert, D. (1993) Aluminium alloys in arc welded constructions. *Welding World Magazine*, 32(**3**), 97–114.
9. *GOST 10157–79: Gaseous and liquid argon. Specifications*. Moscow, Izd-vo Standartov [in Russian].
10. Koval, V.A., Labur, T.M., Yavorska, T.R. (2020) Properties of joints of V1341T grade alloy under conditions of TIG welding. *The Paton Welding J.*, **2**, 35–40.
11. *GOST 1497–84: Metals. Test methods on tension.* Moscow, Izd-vo Standartov [in Russian].
12. *GOST 6996–66: Welded joints. Methods of mechanical properties determination*. Ibid. [in Russian].
13. *GOST 9.021–74: Unified system of corrosion and ageing protection. Aluminium and aluminium alloys. Methods of accelerated tests for interctystalline corrosion*. Ibid. [in Russian].
14. *GOST 9.904–83: Unified system of corrosion and ageing protection. Aluminium alloys. Methods of accelerated tests for exfoliating corrosion.* Ibid. [in Russian].
15. *GOST 9.019–74: Unified system of corrosion and ageing protection. Aluminium and magnesium alloys. Methods of accelerated tests for corrosion cracking*. Ibid. [in Russian].

Received 12.11.2020

https://doi.org/10.37434/tpwj2020.12.07

MODERNIZATION OF OPTICAL MICROSCOPE AND ITS USE TO OBTAIN DIGITAL IMAGES OF MICROSTRUCTURE OF DEPOSITED METAL

A.A. Babinets, I.O. Riabtsev and **I.P. Lentyugov**
E.O. Paton Electric Welding Institute of the NAS of Ukraine
11 Kazymyr Malevych Str., 03150, Kyiv, Ukraine. E-mail: office@paton.kiev.ua

The article analyzes the methods of modernization of optical microscopes to obtain digital images and simplification of their subsequent analysis during basic metallographic examinations of deposited metal specimens. Two main methods of modernization were considered: with the help of a camera, equipped with special adapters, which is attached to the tube of the microscope eyepiece and with the help of a video eyepiece, which is mounted instead of a standard microscope eyepiece. The main advantages and disadvantages of each method were noted. With the help of the metallographic microscope MIM-7, camera Canon 650D, video eyepiece SIGETA MCMOS 3100, as well as specimens of microsections with a deposited layer of semi-heat-resistant steel of C–Cr–Mo–W–V alloying system, comparative metallographic examinations were performed. It is shown that the use of the special video eyepiece SIGETA MCMOS 3100 allows obtaining digital images of metal microstructures with a higher quality. As an illustration of the main advantages of the work, provided by the use of the equipment modernized in such a way, the results of metallographic examination of the metal, deposited by electric arc method using flux-cored wire PP-Np-120V3KhMF, were provided. It was experimentally established that the software Toupview, supplied with the eyepiece SIGETA MCMOS 3100, used during these examinations, allows easy processing of the obtained digital images, which greatly expands the capabilities of basic metallographic analysis. 10 Ref., 7 Figures.

Keywords: metallography, optical microscope, video eyepiece, arc surfacing, flux-cored wire, deposited metal, semi-heat-resistant steel

For today, in many modern metallographic research laboratories special digital microscopes are used, where the image, obtained from the optical system of the device, is transmitted directly to a high-definition light sensor, which allows carrying out its further computer processing easily [1]. Most often, the observations of a studied object is carried out either through the built-in LCD screen, or through the screen of laptop or personal computer, to which the microscope is connected. This significantly simplifies a preliminary search and examination unlike when it is necessary to look all the time into the microscope eyepiece.

In addition, having a digital image of the studied objects, using the appropriate software (further SW), it is possible to apply special filters, highlight the required areas, «glue» several images into one, carry out different measurements, etc., which greatly expands the capabilities of the basic metallographic analysis, reduces the time and complexity of its implementation [2]. Taking into account the fact, that during the development of new materials or surfacing technologies it becomes necessary to perform a large amount of preliminary experiments on the manufacture and study of macro- and micro-sections of the deposited metal, the task of simplifying the basic metallographic analysis is quite relevant.

However, at present some of the research laboratories are still equipped with the optical microscopes MIM, METAM, MMU and other models, where the optical system allows obtaining a sharp image with a magnification of up to 1000 times, but they have no possibility to obtain digital images of the studied objects.

The aim of the work is analyzing and choosing the ways to modernize optical microscopes to obtain digital images and to simplify their subsequent analysis during basic metallographic examinations, as well as to illustrate the capabilities of the modernized metallographic equipment on the example of studying the structure of semi-heat-resistant deposited metal of the alloying system C–Cr–Mo–W–V.

Analysis of ways of modernizing optical microscopes. Taking into account the high cost of both modern digital microscopes, as well as comprehensive professional modernization of existing optical microscopes, many researchers are trying to carry out modernization «on their own». For this purpose, either different digital cameras or special video eyepieces are often used.

A.A. Babinets — https://orcid.org/0000-0003-4432-8879, I.O. Riabtsev — https://orcid.org/0000-0001-7180-7782,
I.P. Lentyugov — https://orcid.org/0000-0001-8474-6819

In the first case, the problem is solved in several ways. Thus, photographing can be performed directly through the eyepiece of the microscope, but this method has significant disadvantages [3, 4]:

- need to provide a rigid attachment of the eyepiece to the camera and alignment of their optical systems;
- need to provide protection against side light-striking;
- additional optics (camera lens) often deteriorates the image quality, reducing its sharpness and brightness.

To eliminate these drawbacks, photographing through the microscope eyepiece can be performed by the camera without its lens, instead of which the optics of the microscope is directly used [3, 4]. In this case, two schemes of work are possible: photographing through the lens and eyepiece of the microscope or only through the lens of the microscope (Figure 1). In both cases, the image is focused only by the microscrew of the microscope by the image on the camera screen.

However, as the experience of using the above-described schemes shows, images with the highest quality can be obtained at low magnifications (not more than ×100), or with the use of additional special expensive optics. For example, in [5] the operability of a similar modified model of the microscope Lomo Metam R-1 by replacing the eyepiece with a digital SLR camera Canon 650D. Therefore, the image was projected to the matrix without the use of the eyepiece of the microscope and the lens of the camera, as is shown in the scheme in Figure 1, *b*.

Using a modified microscope, the authors of [5] obtained digital images at magnifications ×10–×40 (Figure 2). The Figure shows that at a magnification of ×40, the image quality becomes worse — the standard illumination is clearly insufficient to obtain a quality image. Thus, the use of the scheme shown in Figure 1, *b* significantly limits the capabilities of the researcher because of the fact that a total magnification of the microscope in this case will be provided only by its own magnification of the used microscope

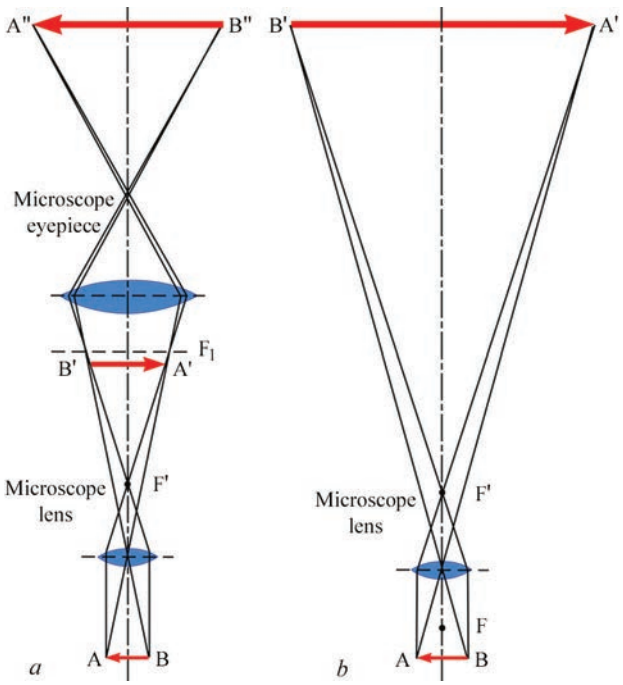

Figure 1. Movement of rays during photographing with the microscope lens and eyepiece (*a*) and with the microscope lens only (*b*) [4]

lenses (usually within ×4–×90) and the abilities of a digitally camera scaling. In addition, the image itself at all magnifications is «clogged» with black edging of the microscope tube.

As is seen, obtaining digital images from the optical microscope using conventional digital cameras is associated with certain difficulties in providing a good quality of images and the need to purchase a camera with the ability of replacing the lens, special adapters for a particular brand of camera and microscope and also such additional equipment, as external illuminators, etc.

The abovementioned disadvantages include the need of making special adapters for mounting the camera on the microscope and the lack of native SW for processing the obtained digital images. Such SW allows performing calibration of the system necessary for carrying out geometrical measurements and the

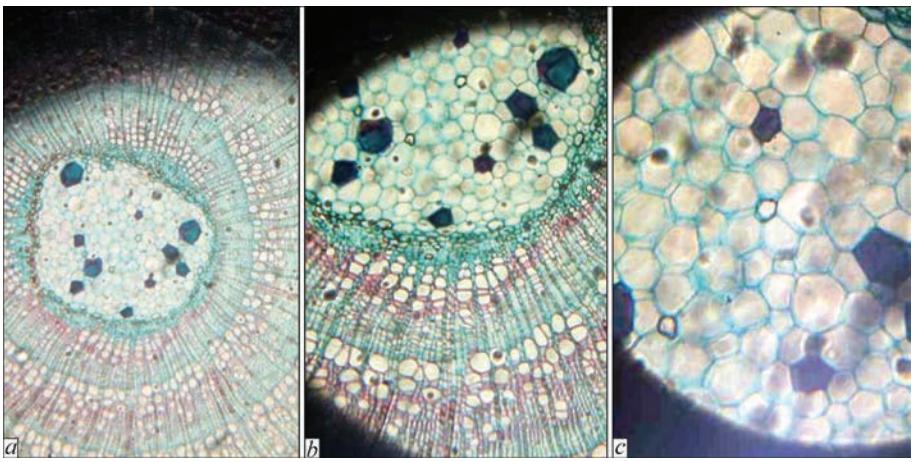

Figure 2. Digital image of the object obtained by the authors of [15] when using lenses with magnification of (*a* — ×10); (*b* — ×20) and (*c* — ×40)

subsequent quantitative analysis and in case of acquisition of special video eyepieces, it is delivered, as a rule, in a set with them.

Therefore, there can be only three advantages of using digital camera together with the optical microscope, they include a high light sensitivity, high separating capability of images and ability of long-term exposures. However, these advantages also depend on the cost of the used equipment as far as manual adjustments of these parameters are possible in the professional cameras.

Based on the abovementioned, it looks more attractive to use special video eyepieces, which allow working with the image in real time directly on the computer monitor. The advantage of such equipment is the simplicity of its installation instead of the native eyepiece, as well as the compliance of the separating capacity of the digital eyepiece to the used magnification, which allows obtaining images with a maximum detailing without extraneous «noises», which significantly increases the accuracy and reproducibility of measurement results [6, 7].

Thus, in [6] the investigations were performed in the microscope MIM-8, instead of whose eyepiece, a digital camera Scope Tek DEM35 was installed, which allowed obtaining high-quality images of microsections of cast irons of grades SCh15 and VCh400-12 and carry out the further analysis of these images. In [7] to study the microstructure, the metallographic microscope Metam LV-42 at a magnification of ×50×1000 together with a digital eyepiece CAM V200 was used.

The cost of digital video eyepieces is determined first of all by the separating capacity of the resulting image, as well as the presence of a special optical unit (homal) at a certain magnification (most often ×10). The presence of the homal is necessary not only to obtain images at a higher magnification, but also to improve the quality of the image itself, as far as the homal serves as a compensation eyepiece to correct image defects due to a chromatic aberration and especially to rectify the curvature of the image plane. The cost of such video eyepieces is also affected by the convenience, efficiency and a number of measuring tools in the SW that is supplied with the eyepiece [2].

Figure 3. Photography equipment used for modernization of the microscope MIM-7: camera Canon 650D with adapters made for it (*a*); video eyepiece SIGETA MCMOS 3100 with set adapters and SW Topview (*b*)

The use of such SW during the subsequent processing and analysis of digital images allows providing a partial automation of this process, significantly reducing the time and labor intensity, in particular, while conducting metallographic analysis, as well as increasing in the accuracy of the results [2]. The examples of such SW paid Thixomet and ZEISS Axiovision, as well as free, such as imagej, Jmicrovision and other may be [6–9].

Comparative analysis of two methods of microscope modernization. Based on the abovementioned, in order to determine the best way to modernize the optical microscope, it was decided to conduct comparative studies of the quality of the obtained digital images using the following equipment: optical metallographic microscope MIM-7, digital camera Canon 650D and video eyepiece SIGETA MCMOS 3100. Due to the fact that the video eyepiece SIGETA is supplied with the homal at the own magnification of ×10, to provide the same conditions, photographing with the camera was performed without its lens with a standard eyepiece, mounted in the microscope tube at the same magnification of ×10 (i.e. according to the scheme, shown in Figure 1, *a*). The lens of the microscope in both cases was the same — achromatic epic lens LOOMP F-6.2; A-0.65, at the own magnification of ×32.

As far as the microscope MIM-7 is not equipped with a standard system for connecting camera to it, special adapters were made, which were put on the tube of the microscope eyepiece and allowed attaching camera to it (Figure 3, *a*). At the same time, mounting of the video eyepiece SIGETA (Figure 3, *b*) on the microscope was much simpler, because it already includes several adapters for the most common diameters of the microscope eyepiece tube. The appearance of the microscope MIM-7, additionally equipped with a camera and video eyepieces, is shown in Figure 4.

To provide an example, a comparison of the quality of digital images obtained from the digital camera Canon 650D and the video eyepiece SIGETA MCMOS 3100 was performed applying microsections of the metal deposited using the flux-cored wire of the alloying system C–Cr–Mo–W–V (PP-Np-120V3KhMF) [10].

The specimens for microstructure examinations were cut out from St3 steel billets deposited in four layers using this wire. The structure of the deposited and base metal was detected by chemical etching in a 4 % alcoholic solution of the nitric acid HNO_3. Before the measurements, the microscope and SW were calibrated using a micrometer object.

Results of comparative analysis of two methods of microscope modernization. Significant differences

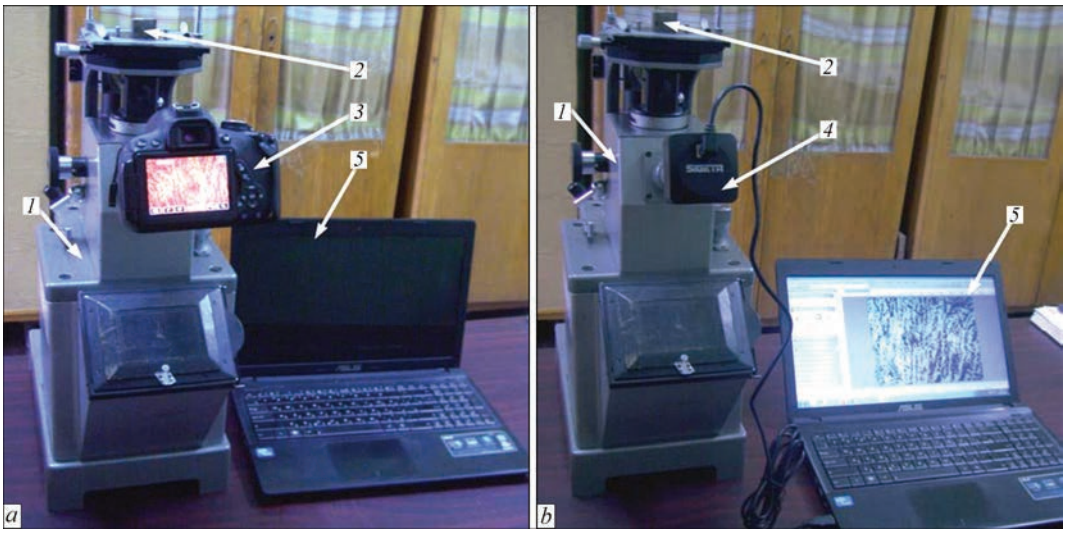

Figure 4. Modernized microscope MIM-7 when using camera (*a*) or video eyepiece (*b*): *1* — microscope MIM-7; *2* — test specimen; *3* — camera Canon 650D; *4* — eyepiece SIGETA; *5* — laptop with a special SW

in the use of the camera and video eyepieces to obtain digital images in the optical microscope are observed at the early stages of work during setting up the equipment. In case of using camera, it is necessary to correctly adjust the exposure value, aperture, light sensitivity, white balance, etc., because automatic adjustments often do not allow obtaining an acceptable image quality. It is rather problematic to do this operation at a high level, looking at a small screen of the camera (Figure 4, *a*). In addition, using the camera settings it was still failed to remove the yellowness of the image provided by the incandescent lamp used in the microscope MIM-7.

After mounting the video eyepiece SIGETA in the microscope tube, it is connected to the computer using USB cable and with the help of the SW supplied in the set with the video eyepiece, it displays the resulting image on the screen (Figures 4, *b*). It is much easier to sharpen and search for the desired area of the microsection on the big screen, and due to the wide capabilities of SW Toupview, manual adjustment (if automatic settings do not suit the user) of the image quality obtained from the microscope takes no more than a few minutes. With the help of «sliders», the user can change such parameters as exposure, white balance, color tone, saturation, brightness, contrast, sharpness, etc. in real time, reaching the maximum quality of the resulting image. Also, using the built-in capabilities of SW, it is possible to reduce the «noise» of the image, highlight objects of the same color, «stitch» several images into one, etc.

For comparison, the images of the same areas of the specimen obtained using the digital camera Canon 650D and the video eyepiece SIGETA at the same magnification (×320) are shown in Figure 5. As is seen, the use of the video eyepiece SIGETA allows obtaining a higher quality and detailing of the image as compared to using digital camera. In addition, the sharpness of the images obtained with the help of the camera is not the same over the entire area of the image — the area of sharpness in the central part of the

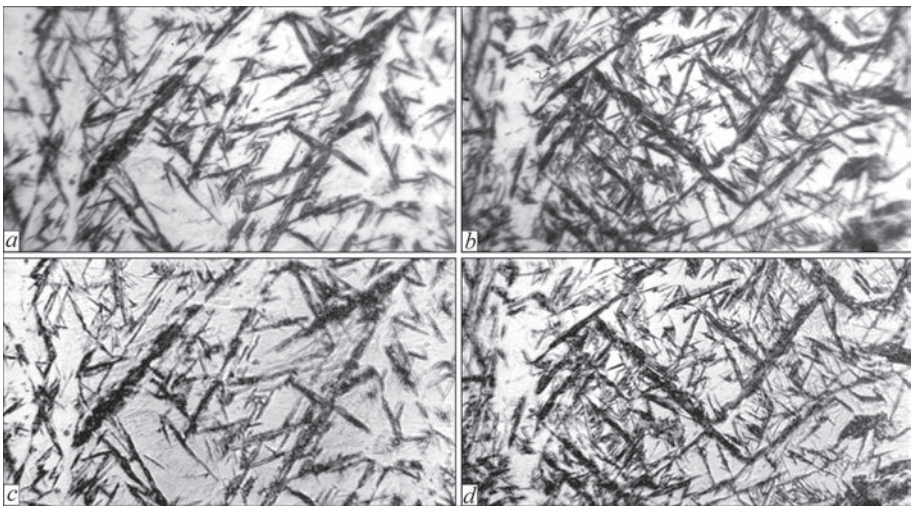

Figure 5. Microstructure (×320) of the specimen deposited using the wire PP-Np-120V3KhMF. Photo taken with the camera Canon 650D (*a*, *b*) and video eyepiece SIGETA MCMOS 3100 (*c*, *d*)

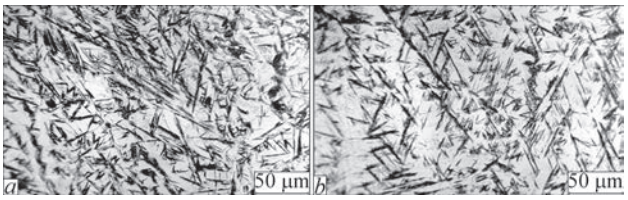

Figure 6. Microstructure (×320) of metal in the center (*a*) and at the upper edge (*b*) of the layer deposited using the flux-cored wire PP-NP-120V3KhMF

image occupies about 45 % of its total area (Figure 5, *a*, *c*). The image obtained with the help of the video eyepiece SIGETA has a more uniform sharpness over almost the entire area of the image (Figure 5, *b*, *d*). In this case, the area with a good sharpness amounts to more than 85 % of the image area.

Taking into account the advantages of using the video eyepiece SIGETA described above, as an illustration, the abilities of operation with this equipment and SW Toupview during metallographic analysis are given more fully below.

The structure of the metal, deposited using the flux-cored wire PP-Np-120V3KhMF consists of martensite with large and small needles of different etching and a small amount of residual austenite (Figure 6, *a*). At the upper edge of the deposited metal, the amount of residual austenite increases slightly, and the size of martensite needles, on the contrary, decreases (Figure 6, *b*). In this case, the typical structure of the cast metal is preserved along the entire height of the deposited layer. Analysis of the structure of the metal in the heat-affected-zone (HAZ) showed (Figure 7, *a*), that it consists of a ferrite-pearlite mixture, here the amount of ferrite predominates.

It should be noted that in the deposited specimens, individual pores were revealed in the lower layer of the deposited metal, near the fusion line (Figure 7, *b*). The average pore size is 76 μm. Also, on the polished non-etched specimens, the sizes, amount and number size of nonmetallic inclusions were determined. In the studied specimens oxides, sulfides and oxisulfides were revealed. The amount of inclusions is small, they are located rather uniformly and have a predominantly round shape. The volume fraction of inclusions in the metal deposited by the test flux-cored wire PP-Np-120V3KhMF was 0.18 %.

Conclusions

1. There are several different methods for modernization of optical microscopes with the purpose of obtaining digital images, the most appropriate of which is the use of digital video eyepieces, which are mounted directly into the microscope tube without any additional manipulations. It is possible to significantly accelerate and simplify measurements when performing basic metallographic analysis using a specialized SW for digital image processing.

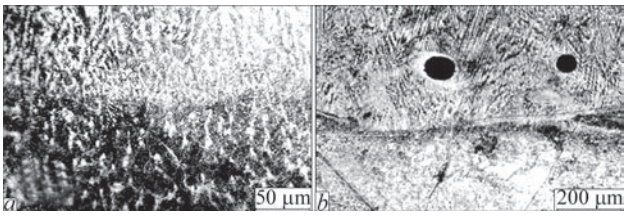

Figure 7. Microstructure of metal near the fusion line in the specimen deposited using the wire PP-Np-120V3KhMF: *a* — ×320; *b* — ×90

2. With the help of microsections of the metal deposited using the flux-cored wire of the alloying system C–Cr–Mo–W–V (PP-Np-120V3KhMF), the main advantages and capabilities of the metallographic analysis, carried out by means of the microscope MIM-7, modernized by mounting the video eyepiece SIGETA MC-MOS 3100 and using SW Toupview 3.7 are shown.

1. Litovchenko, S.V., Malykhina, T.V., Shpagina, L.O. (2011) Automation of analysis of metallographic structures. *Visnyk KhNU*, **960**, 215–223 [in Russian].
2. Panteleev, V.G., Egorova, O.V., Klykova, E.I. (2005) *Computer microscopy*. Moscow, Tekhnosfera [in Russian].
3. Trankovsky, S.D. (2014) How the microscope operates. *Nauka i Zhizn*, **2**, 101–104 [in Russian].
4. Hawkins, A., Avon, D. (1980) *Photography: The guide to technique*. London, Book Club Associates.
5. Guzhov, V.I., Iltimirov, D.V., Khaidukov, D.S. et al. (2016) Modification of optical microscope. *Avtomatika i Programmnaya Inzheneriya*, **2**, 71–76 [in Russian].
6. Lutai, A.M., Klimchuk, O.S., Klyufinskyi, V.B. (2016) Automation of analysis of metallographic microstructures. In: *Proc. of 3rd Int. Sci.-Pract. Conf. on Automation and Computer-Integrated Technologies*. Kyiv, NTUU KPI, 121–123.
7. Glukhova, K.L., Dolgodvorov, A.V. (2014) Examination of microstructure of composite structural material at the stage of carbon-filled plastic producing. Vestnik PNIPU. *Aerokosmicheskaya Tekhnika*, **2**, 222–235 [in Russian].
8. Ternovykh, A.M., Tronza, E.I., Yudin, G.A., Dalskaya, G.Yu. (2013) ELEMENTIZER – program module of microstructural analysis. Vestnik MPGUPiI. *Priborostroenie i Informatsionnye Tekhnologii*, **44**, 106–114 [in Russian].
9. Zubko, Yu.Yu., Frolov, Ya.V., Bobukh, A.S. (2017) Influence of MECAP on microstructure of AD0. *Obrabotka Materialov Davleniem*, **2**, 93–100 [in Russian].
10. Lentyugov, I.P., Ryabtsev, I.A. (2015) Structure and properties of metal deposited by flux-cored wire with charge of used metal-abrasive wastes. *The Paton Welding J.*, **5–6**, 87–89. DOI: https://doi.org/10.15407/tpwj2015.06.19

Received 17.11.2020